2017

Wind Turbine Wake Interactions - Characterization of Unsteady Blade Forces and the Role of Wake Interactions in Power Variability Control

Daniel Curtis Saunders
University of Vermont

WIND TURBINE WAKE INTERACTIONS – CHARACTERIZATION OF UNSTEADY BLADE FORCES AND THE ROLE OF WAKE INTERACTIONS IN POWER VARIABILITY CONTROL

A Dissertation Presented

by

Daniel Curtis Saunders

to

The Faculty of the Graduate College

of

The University of Vermont

In Partial Fulfillment of the Requirements
for the Degree of Doctor of Philosophy
Specializing in Mechanical Engineering

May, 2017

Defense Date: March 10, 2017
Dissertation Examination Committee:

Jeffrey S. Marshall, Ph.D., Advisor
Paul D. H. Hines, Ph.D., Chairperson
Yves Dubief, Ph.D.
Darren L. Hitt, Ph. D.
Cynthia J. Forehand, Ph.D., Dean of the Graduate College

ABSTRACT

Growing concerns about the environmental impact of fossil fuel energy and improvements in both the cost and performance of wind turbine technologies has spurred a sharp expansion in wind energy generation. However, both the increasing size of wind farms and the increased contribution of wind energy to the overall electricity generation market has created new challenges. As wind farms grow in size and power density, the aerodynamic wake interactions that occur between neighboring turbines become increasingly important in characterizing the unsteady turbine loads and power output of the farm. Turbine wake interactions also impact variability of farm power generation, acting either to increase variability or decrease variability depending on the wind farm control algorithm. In this dissertation, both the unsteady vortex wake loading and the effect of wake interaction on farm power variability are investigated in order to better understand the fundamental physics that govern these processes and to better control wind farm operations to mitigate negative effects of wake interaction.

The first part of the dissertation examines the effect of wake interactions between neighboring turbines on the variability in power output of a wind farm, demonstrating that turbine wake interactions can have a *beneficial* effect on reducing wind farm variability if the farm is properly controlled. In order to balance multiple objectives, such as maximizing farm power generation while reducing power variability, a model predictive control (MPC) technique with a novel farm power variability minimization objective function is utilized. The controller operation is influenced by a number of different time scales, including the MPC time horizon, the delay time between turbines, and the fluctuation time scales inherent in the incident wind. In the current research, a non-linear MPC technique is developed and used to investigate the effect of three time scales on wind farm operation and on variability in farm power output. The goal of the proposed controller is to explore the behavior of an 'ideal' farm-level MPC controller with different wind, delay and horizon time scales and to examine the reduction of system power variability that is possible in such a controller by effective use of wake interactions.

The second part of the dissertation addresses the unsteady vortex loading on a downstream turbine caused by the interaction of the turbine blades with coherent vortex structures found within the upstream turbine wake. Periodic, stochastic, and transient loads all have an impact on the lifetime of the wind turbine blades and drivetrain. Vortex cutting (or vortex chopping) is a type of stochastic load that is commonly observed when a propeller or blade passes through a vortex structure and the blade width is of the same order of magnitude as the vortex core diameter. A series of Navier-Stokes simulations of vortex cutting with and without axial flow are presented. The goal of this research is to better understand the challenging physics of vortex cutting by the blade rotor, as well as to develop a simple, physics-based, validated expression to characterize the unsteady force induced by vortex cutting, such as might be used in a control algorithm or material fatigue analysis.

CITATIONS

Material from this dissertation has been published in the following form:

Saunders, D.C., Marshall, J.S.. (2015). Vorticity reconnection during vortex cutting by a blade. *Journal of Fluid Mechanics*, **782**, 37-62.

Material from this dissertation has been accepted for publication to the Journal of Fluid Mechanics on March 20, 2017 in the following form:

Saunders, D.C., Marshall, J.S.. Transient lift force on a blade during cutting of a vortex with non-zero axial flow. *Journal of Fluid Mechanics*.

Material from this dissertation has been submitted for publication to Wind Energy on January 25, 2017 in the following form:

Saunders, D.C., Marshall, J.S., Hines, P.D.. The importance of timescales in a nonlinear model predictive controller for dynamic wind farm performance. *Wind Energy*.

ACKNOWLEDGEMENTS

First and foremost, I would like to thank my Ph.D. adviser, Dr. Jeff Marshall. Jeff's mentorship and guidance with this project has been instrumental in its success. Furthermore, his vast knowledge of fluid mechanics and his dedication to helping his students succeed is remarkable. I would also like to thank my other committee members, Dr. Darren Hitt, Dr. Yves Dubief, and Dr. Paul Hines for their help and guidance. I have enjoyed working with each of them whether it be through class instruction, dissertation guidance, or research collaboration.

I would also like to thank my friends and officemates who have significantly enriched these past few years. Thank you to Emily for making sure that group lunch occurred every day, and that my weekend social schedule was never empty. Thank you to Tom for being a sounding board for research ideas, and for assisting me with many woodshop projects. Thank you to Mark for talking through many potential research collaborations, patiently answering any programming questions that I had, and for making sure I always had my afternoon cup of coffee. In addition, I would like to thank Banjo, the IGERT dog, for providing me with hugs, kisses, and lots of fresh air as we went on our walks around the UVM campus.

Finally, I would like to thank my family. Thanks to my parents, Dan and Liz, sister, Janet, and nieces, Emma and Natalie. Their love and support are invaluable and I will always be grateful.

TABLE OF CONTENTS

Page

LIST OF TABLES

LIST OF FIGURES

CHAPTER 1: MOTIVATION AND OBJECTIVES

1.1. Motivation

Growing concerns about the environmental impact of fossil fuel energy and continued improvements in both the cost and performance of wind turbine technologies has enabled wind power to become an increasingly popular option for electricity generation (US DOE, 2015). As a result of technological advances the average nameplate capacity of new wind turbines installed in the US in 2014 has increased by 172%, the average hub height has increased by 48%, and the average rotor diameter has increased by 108%, all since 1998-1999 (US DOE, 2015). Larger rotor diameters allow wind turbines to reach stronger winds that are found higher in the atmosphere and to achieve greater swept areas; both of which contribute to increased electricity production. In addition, wind farms are also growing in size as larger farms allow for greater economic efficiencies (Wu et al., 2011). All of this has contributed to wind energy representing 24% of the electric-generating capacity added to the US in 2014 (US DOE, 2015). To maximize land use within a wind plant, wind turbines are often placed close together, whether in an array or along a ridgeline. The close proximity of the wind turbines within modern wind farms allows them to interact aerodynamically with their neighbors (via their wakes) to a much greater extent than in the past. These wake interactions have a significant impact on the overall wind farm power output, on the variability in wind farm power output, and on the enhanced fatigue damage to the wind turbines and their various components (e.g., the gearbox and high speed shafts) that occurs due to turbine operation in the turbulent wake of upstream turbines. Turbine wake interactions also have an

impact on the control of wind farms (Gonzallez-Longatt et al., 2012), and their effects may be either detrimental or beneficial to wind farm operation depending on the wind farm control strategy and objective. In this dissertation, aspects of wind farm wake interactions which contribute to these effects will be examined in detail.

The first aspect of wind turbine wake interactions to be examined is the effect of wakes on the variability in wind farm power output, as regulated by the wind farm control scheme. The wind resource varies over timescales of seconds to days at a given location, and the power output of wind farms varies accordingly (Burton et al., 2008). While the electric grid can handle small amounts of variation in power generation with use of limited storage or dispatchable power sources, large amounts of variability can cause serious issues with grid stability. Furthermore, as wind farms grow in size and capacity, operators will be increasingly called upon to track power set points rather than supplying the maximum amount of power possible (Knudsen et al., 2015). These issues increase the need for wind farm controllers and engineering turbine wake models that more accurately capture the time-varying dynamics of wind farms resulting from unsteady wind velocity and turbine wake interaction, rather than just steady-state behavior, and that specifically account for the costs of power variability in the controller design.

The second aspect of wake interactions to be examined is the interaction of turbine blades with vortex structures contained within the wakes of upstream turbines. As previously stated, wake interactions are a source of fatigue loading on wind turbines. Fatigue loadings can be categorized as either steady, cyclic, transient, stochastic, or resonance-induced (Manwell et al., 2009). Both the magnitude and timescale of the force

contribute to the fatigue load; a force with a small magnitude but a fast timescale can be a significant source of fatigue damage to certain turbine components, such as the gearbox. The interaction of turbine blades with vortex structures contained within the wakes of upstream turbines is an important type of stochastic load. The wind turbines ingest and chop vortices of the incident atmospheric flow (Churchfield et al., 2012; Shafii et al., 2013), particularly in rough topological conditions or when situated in a wind farm and subjected to the wake of upstream turbines. In the canonical vortex cutting problem, the ambient vortex axis is orthogonal to the symmetry plane of the blade and the relative translation velocity of the blade and the vortex is in the direction of the blade chord (Coton et al., 2004). In cases where the vortex possesses a non-zero axial flow, vortex cutting events can lead to exertion of a sudden force on the blade, which can cause performance degradation, material fatigue or pitting (particularly in the presence of local cavitation), and noise and vibration generation (Ahmadi, 1986; Cary, 1987; Paterson and Amiet, 1979). These unsteady forces on blades, airfoils, and impellers due to chopping of vortex structures in the incident flow are not unique to wind turbines and play an important role in many different applications. In helicopters that are either hovering or moving forward slowly, vortices shed from the main rotor are swept backward and impinge on the vehicle tail or are entrained into the tail rotor (Leverton et al., 1977; Cary, 1987; Sheridan and Smith, 1980). For fixed-wing aircraft, the effects of 'wake turbulence' due to interaction of an airplane with the wake vortices of a preceding airplane continues to be a leading cause of accidents, particularly among smaller aircraft. In many pumps, such as axial flow pumps, intake vortices and turbulent flow vortices in the intake flow are chopped by the pump impeller (Nagahara et al., 2001). The

streamwise hull vortices on torpedoes and submersibles, as well as vortices shed from upstream control surfaces, can be ingested into a propeller intake and chopped by the propeller blades (Felli et al., 2009, 2011). A similar phenomenon occurs in turbomachinary flows, where vortices shed from the upstream stator blades are carried downstream and chopped by the rotor blades (Binder, 1985), leading to turbulence generation.

1.2. Objective and Scope

The objective of this dissertation is to investigate both the unsteady vortex wake loading and the effect of wake interactions on farm power variability in order to better control wind farm operations and mitigate the negative effects of wake interactions. This objective is pursued by a series of three studies on different aspects of wind farm operation, each having to do with turbine interaction with upstream turbine wakes. The first study examines the importance of wake interaction on the control of a wind farm for both power maximization and variability minimization. In particular, the study examines the relative importance of three time scales − the time delay between turbines, the timescale of incident wind fluctuations, and the model predictive control (MPC) time horizon − in designing a dynamic wind farm controller. The controller is used to evaluate the performance subjected to a wind signal with a single, dominant period and to an experimentally-obtained wind data signal with a full spectrum of oscillations. Variability can be described by both the speed and magnitude of wind fluctuations. Two novel objective functions are proposed which allow for the controller to simultaneously maximize farm electric energy output while minimizing the farm power variability. Their

performance is assessed and the effect of the relative weighting between power maximization and variability minimization on the solution is explored.

The second study examines the basic phenomenon of vortex cutting by a blade. The study particularly examines the relationship between the dimensionless parameters and time scales governing the breaking and rejoining of vortex lines in both the vortex cutting problem and the classical vortex tube reconnection problem, and whether the different phases of the vortex reconnection problem (see, e.g., Kida and Takaoka, 1994, or Shelley et al., 1993) have analogues in the vortex cutting problem. A series of Navier-Stokes simulations of vortex cutting with different values of the vortex strength are described, and the different phases in the vortex cutting process are compared to those of the more traditional vortex tube reconnection process. In addition, a highly simplified model is presented that examines the vorticity diffusive cancellation process between an incident vortex (a stretched vortex sheet) and vorticity generated from a no-slip surface.

The third study extends the vortex cutting study to examine orthogonal cutting of vortices with non-zero ambient axial velocity by a blade. The study, in particular, seeks to explain the underlying physics of the transient vortex cutting force through a combination of scaling analysis, heuristic modeling, and full viscous flow simulations. Issues of particular interest include how the transient vortex cutting force depends on the various dimensionless parameters that govern the flow field, and how the transient force compares to the steady-state vortex cutting force. This third study results in a simple expression for the unsteady loading on a wind turbine resulting from chopping of an ingested vortex structure, which is explained by theory and validated by full Navier-Stokes simulations.

CHAPTER 2: LITERATURE REVIEW

A significant body of existing literature on wind turbine wake interactions focuses on topics such as wind turbine placement, turbine power maximization, turbine power variability, wake steering, and wake interaction damage. This chapter examines two specific topics relevant to the dissertation objective – wind farm control and vortex-blade interaction (with specific focus on vortex cutting). In-between these two reviews is a short discussion of the phenomenon of vortex reconnection, which is important for understanding vortex cutting by a turbine blade.

2.1. Wind Farm Control

Previous work on wind farm control includes both individual turbine and farm level control. Traditionally, individual turbine controllers deal with events on the order of tenths of a second to seconds. Proportional-integral-derivative (PID) controllers have been widely used in wind turbines and an overview of them can be found in many wind energy textbooks (e.g. Burton et al., 2008). These controllers have the ability to regulate the electrical torque on the generator, the collective pitch angle of the turbine blades, and the yaw angle of the turbine. Together with the wind speed, these variables determine the rotational rate of the wind turbine and consequently the electrical power output of the turbine. PID controllers are designed to maximize the power of individual turbines and the controller actions are determined based on the wind speed reaching the turbine (Figure 2.1). Above the cut-in speed of the turbine, the controller works to maximize the power extracted from the wind by increasing the electrical torque of the generator, while

holding the blade pitch angle constant. This control regime is referred to as *Region 2 control*. As the wind speed continues to increase and the turbine rotor reaches its rated speed, the controller operates in *Region 3 control*. In this region, the electrical torque is held constant while the controller adjusts the blade pitch angles so as to maintain the rated power output of the wind turbine.

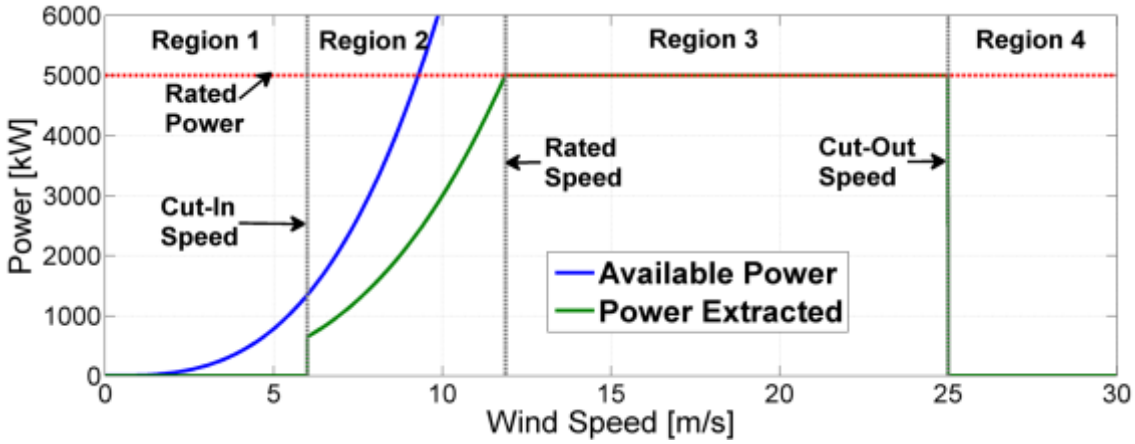

Figure 2.1: Power output of a wind turbine as a function of wind speed. The wind turbine controller operates in different regions depending on the wind speed. Adapted from Aho et al. (2012).

More recent research has concentrated on other forms of control, including Gain Scheduled Linear Quadratic Regulator (LQR) (Bossanyi, 2003; Boukhezzar et al., 2007), Feedback Linearization (Burkart et al., 2011; Kumar et al., 2010), H_2 and H_∞ Control (Rocha et al., 2005; Kristalny et al., 2013; Ozdemir et al., 2013), and Model Predictive Control (MPC) (Sorensen et al., 2002; Kumar et al., 2009; Koerber & King, 2011; Laks et al., 2011; Soltani et al., 2011; Koerber & King, 2013; Schlif et al., 2013; Spencer et al., 2013). These control systems are explicitly formulated according to a set of objectives, which often extend beyond the typical goals of maximizing power output or tracking a

power signal, to additional objectives such as limiting tower loads, blade loads, shaft twist, power outputs, and power fluctuations. Since these approaches explicitly or implicitly use optimization methods, these different objectives can be given different weights, allowing one to make tradeoffs that align with the goals for a particular location.

MPC techniques have been gaining in popularity due to their ability to handle multiple objectives and to explicitly incorporate constraints within the controller. Another advantage is their ability to incorporate predictions of future wind speeds and to model how the plant will respond to disturbances in the wind (Spencer et al., 2013).

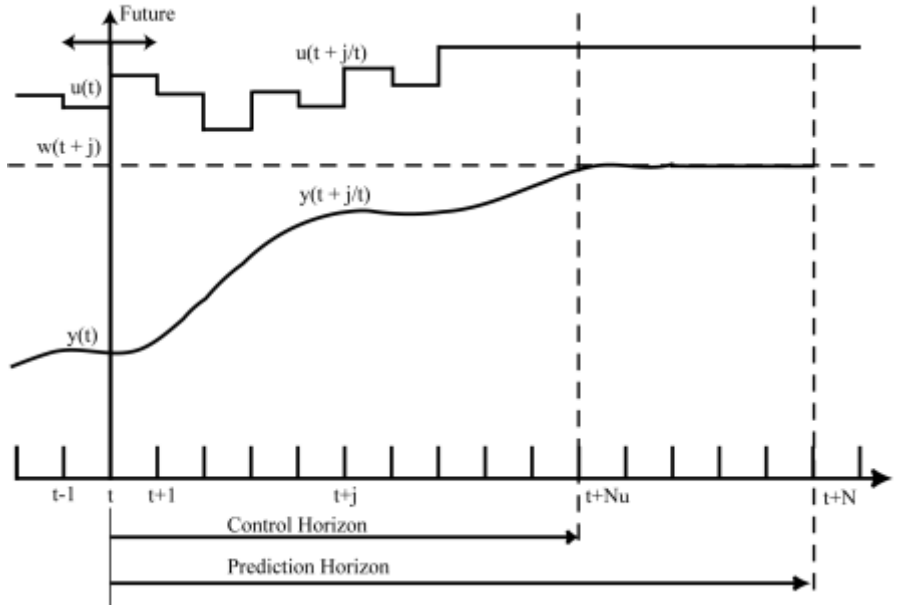

Figure 2.2: Operation of a Model Predictive Controller. Given a model of the system and a prediction for how the inputs will change with time, the controller calculates the output of the system over the prediction horizon ($y(t + j/t)$) and implements the solution ($u(t + j/t)$) over the control horizon before again recalculating an optimal solution over the next prediction horizon. Adapted from Holkar et al. (2010).

Formulations have been developed based on linearized MPC (Korber and King, 2009; Spencer et al., 2013; Kumar et al., 2009; Lindeberg, 2009), continuously linearized MPC, and nonlinear MPC techniques (Botasso et al, 2007; Korber and King, 2011;

Schlipf et al., 2013). Schlipf et al. (2013) found that by combining a nonlinear MPC model with LIDAR predictions, they could achieve a 50% reduction in loads from extreme gusts and a 30% reduction in lifetime fatigue loads without a negative impact on overall energy production. Botasso et al. (2007) found that their nonlinear MPC scheme achieved significant improvements in the control of the turbine over conventional PID controllers even without wind field predictions in the presence of wind gusts or large variations in wind speed.

With greater amounts of electricity being produced from wind farms, farm level controllers have become increasingly important. Farm level controllers are generally supervisory controllers that either directly actuate individual wind turbines or send power reference signals to turbines (Knudsen et al., 2015).

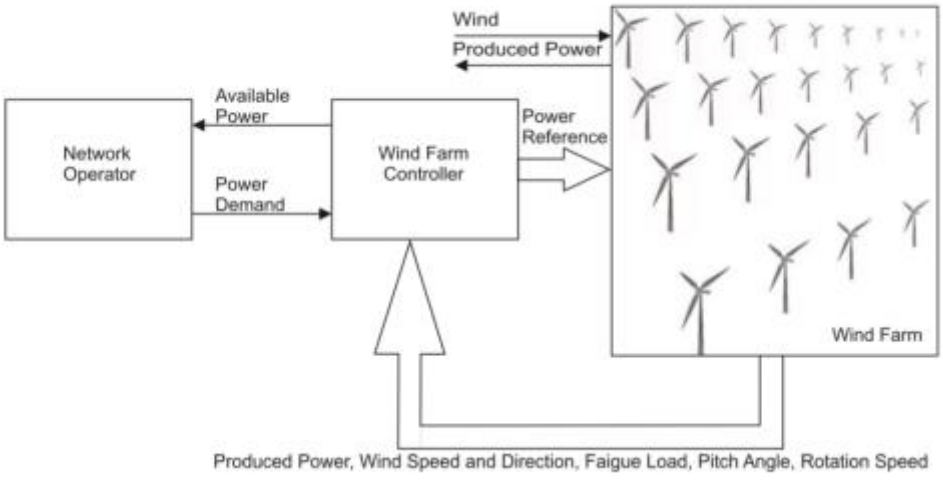

Figure 2.3: Centralized wind farm controller with inputs and outputs. Adapted from Knudsen et al. (2015).

These controllers are called on to either maximize the total wind farm electrical power or to follow a reference for wind farm power, while in some cases simultaneously

minimizing the fatigue loadings of the individual turbines within the wind farm (Knudsen et al., 2015). Steinbuch et al. (1988) proposed a centralized farm-level controller to maximize the power production of wind farms. They showed that a single farm level controller could produce more power from a wind farm than individual turbine controllers given the same wind velocities by utilizing a method of control referred to as axial-induction-based control. In this method, the power production of upstream turbines is decreased to increase the wind velocity in the wakes of the upstream turbines. Consequently, this increased wake velocity increases the power produced by the downstream turbines which results in a net increase in power produced from the wind farm. This occurrence is due to the fact that when the turbines are operating in below-rated wind velocities, the power maximization operating point of the turbine is not very sensitive to the turbines' pitch and electrical torque settings while the thrust is very sensitive to these settings at the operating point (Figure 2.4). Since the thrust of the upstream turbine determines the velocity within the wake, by deviating slightly from the maximum operating point and accepting a slight decrease in power from the upstream turbines, the velocity in the wake will increase significantly and allow a greater increase in power production from downstream turbines (Figure 2.5). Since this study, various other centralized control systems have been proposed (Johnson et al., 2012; Spruce, 1993; Bjerge et al., 2007; Spudic et al., 2011).

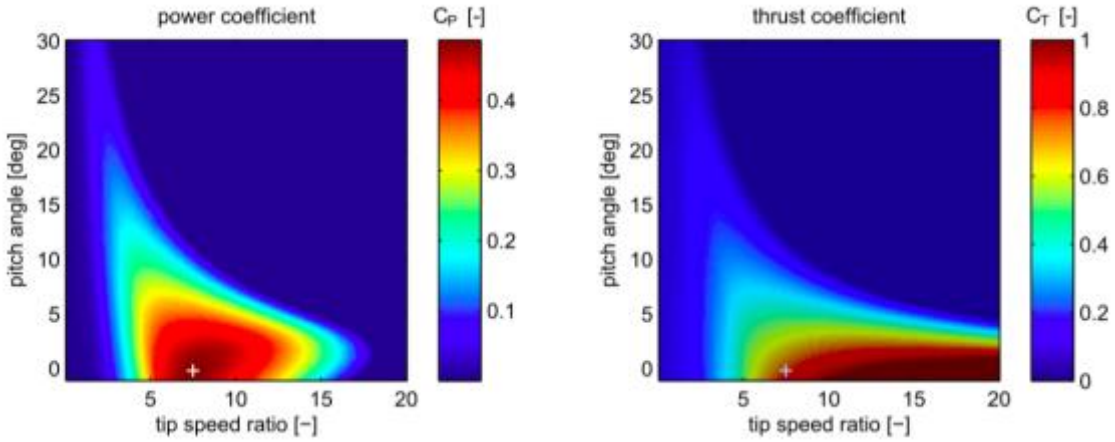

Figure 2.4: Power and thrust coefficients for the NREL 5 MW reference turbine as a function of blade pitch angle and tip-speed ratios. The cross (+) indicates the power-maximizing operating point Adapted from Annoni et al. (2016).

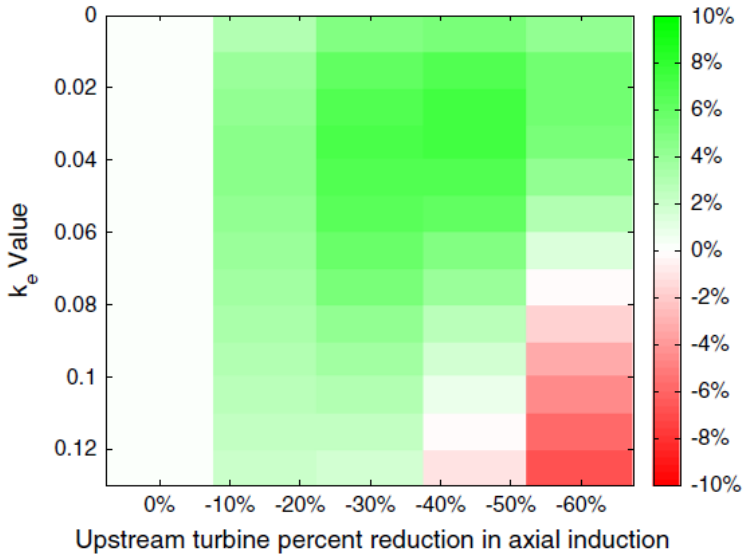

Figure 2.5: Increase (green) or decrease (red) in farm power with respect to the individual turbine control case. Adapted from Annoni et al. (2015).

A downside to centralized controllers is the large amount of rapid communication necessary between the controller and individual wind turbines. To address this problem,

several schemes with a combination of centralized and individual control have been proposed. These controllers all operate on similar principles of calculating an optimal solution and then distributing the power reference signals to individual wind turbines (Hansen et al., 2006; Rodriguez-Amendo et al., 2008; Spudic et al., 2010; Guo et al., 2013; Ebrahimiet al., 2016). As an alternative to centralized control, several distributed control schemes have also been proposed. Soleimanzadeh et al. (2013) proposed an H_2 controller design to provide a pre-determined amount of farm power while minimizing the structural loads to wind turbines. Spudic et al. (2015) proposed a cooperative distributed MPC approach which incorporated a wind forecast to reduce turbine fatigue while tracking the power set point determined for the wind farm. Other distributed controllers have been proposed by Mauledoux and Shkodyrev (2009), Madjidian et al. (2011), Marden et al. (2013) and Gebraad et al. (2015), all with similar goals of maximizing or tracking a power set point, while in some cases also minimizing fatigue loadings on individual wind turbines.

While some previous studies have allowed for time delay between the turbines, the relative importance of the different timescales in this problem has not been fully addressed. For instance, Gonzalez-Longatt et al. (2012) implemented a time delay in their wake models to investigate the impacts of turbine wakes with both steady and varying winds. They assumed a constant acceleration of the air between the turbines and calculated the time delay using an average of the wind speeds at the two turbines.

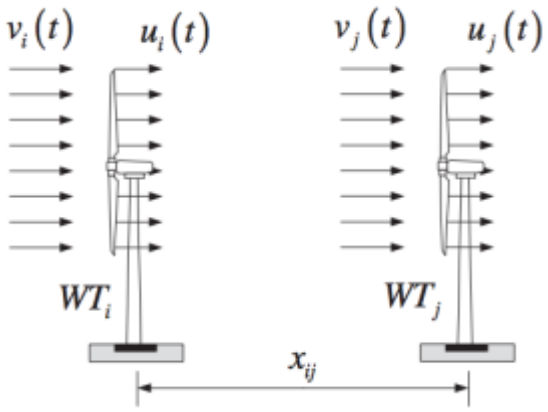

Figure 2.6: Two-turbine case used for calculation of time delay. Adapted from Gonzalez-Longatt et al. (2012).

However, this scheme was not implemented into a wind farm controller. Johnson et al. (2012) incorporated a time delay into their centralized control system for the purpose of maximizing the power production from a wind farm but did not attempt to control for turbine fatigue damage or power fluctuations. Their time delay was calculated using Simulink's variable time delay blocks in which the time delay is calculated from the velocity at the downstream wind turbine. Finally, Gebraad et al. (2015) implemented a time delay model similar to Gonzalez-Longatt et al. (2012) and reported results from a distributed gradient-based control system, but also did not attempt to minimize power fluctuations while tracking a power set point.

2.2. Vortex Reconnection

As previously stated, coherent vortex structures shed off of upstream turbines travel within the turbine wakes and impact downstream turbine blades. In an inviscid fluid, Helmholtz's laws require that vortex lines remain material lines, and consequently

the vortex tube will deform around the blade leading edge, but vortex lines originating within the vortex tube will remain within the tube. In a viscous fluid the Helmholtz restriction no longer applies, and vortex lines originating within the tube are observed to break and reconnect to vortex lines originating within the blade boundary layer (Liu and Marshall, 2004). The term *vorticity reconnection* (or simply *vortex reconnection*) refers to the topological change associated with vortex lines originating within the vortex tube breaking and reconnecting to vortex lines originating within a different vorticity region (Kida and Takaoka, 1994).

While the ultimate interest in the current dissertation is on the impulsive force on turbine blades from vortex cutting, it is necessary to understand aspects of more basic vortex reconnection processes in order to appreciate the specific type of vortex reconnection involved in the vortex cutting process. Some of the basic vortex reconnection that have been examined by previous researchers include interaction of two vortex tubes (Melander and Hussain, 1988; Melander, 1988), colliding vortex rings (Kida et al, 1991), and tubes of unequal strength (Marshall et al., 2001; Zabusky and Melander, 1989).

As described by Melander and Hussain (1989), vortex reconnection processes can be characterized by a series of three phases: 1) *inviscid induction*, which leads to alignment of the vortex cores into an anti-parallel formation (in which vortex axes are parallel with opposite axial vorticity sign) followed by core flattening and stretching, 2) *bridging* of the vortex cores, which occurs via cross-diffusion and cancelation of opposite-sign vorticity between the cores and subsequent linking of vortex lines, and 3) *threading*, or formation of fine threads from remnants of vorticity that have not yet

completed reconnection before the cores are advected away from each other as a result of the high curvature of the reconnected vorticity sections. These three stages of the vortex reconnection process are given in Figure 2.7.

Figure 2.7: Three stages of vortex reconnection (a) induction, (b) bridging, (c) threading. Adapted from Marshall (2001).

In the first phase of reconnection, two vortices driven towards each other will deform to adopt an anti-parallel configuration in the region near the reconnection position (Siggia, 1985). In many reconnection problems, the vortices are initially placed so that they will interact in this anti-parallel orientation, but in some cases, such as the problems of orthogonally offset vortices examined by Boratav et al. (1992) and Zabusky and Melander (1989), significant distortion of the vortices is required to attain the anti-parallel configuration. Once in this anti-parallel configuration, each vortex will induce a two-dimensional straining flow on the opposing vortex, and as a consequence the core of each vortex will become deformed and elongated. The curvature of the three-dimensional vortices along their axes both serves to drive the vortex cores into each other and to induce an additional background straining flow on the vortex pair which causes each deformed core to develop a *head-tail structure* (Kida et al., 1991). As shown in Figure 2.8, the "head" is a region of increased thickness along the outside of the curved vortex core and the inner part of the core stretches out to become the "tail".

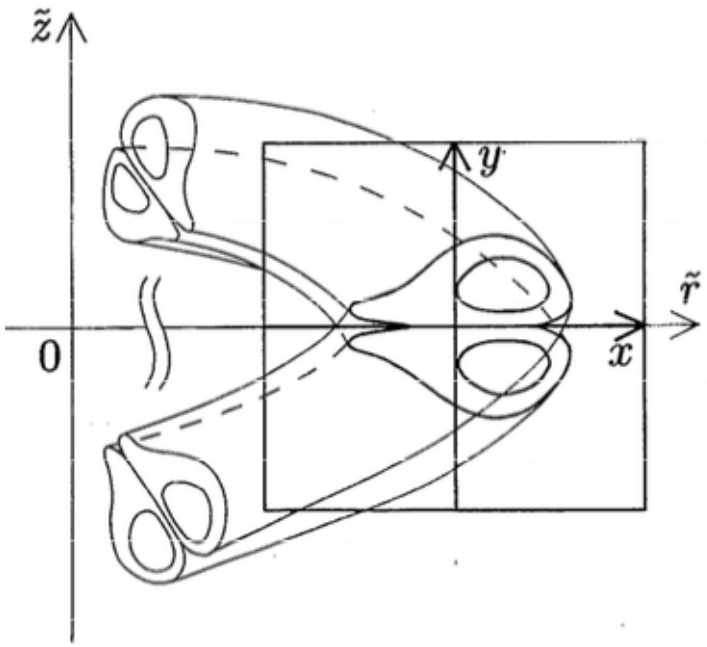

Figure 2.8: Deformation of vortex cores into a head-tail configuration. Adapted from Kida et al. (1991).

The second "bridging" phase of vortex reconnection is dominated by the diffusive cross-cancellation of vorticity between the two anti-parallel vortex cores. As the opposite-sign vorticity cancels out due to diffusion between the two touching vortex cores, the vortex lines passing through the annihilated vorticity reconnect to those from the opposing vortex as a consequence of the requirement that the strength of a vortex tube remains uniform along the tube. These resulting bridges between the two vortex structures continue to grow stronger as more vorticity is diffusively annihilated within the vortex cores (Figure 2.9).

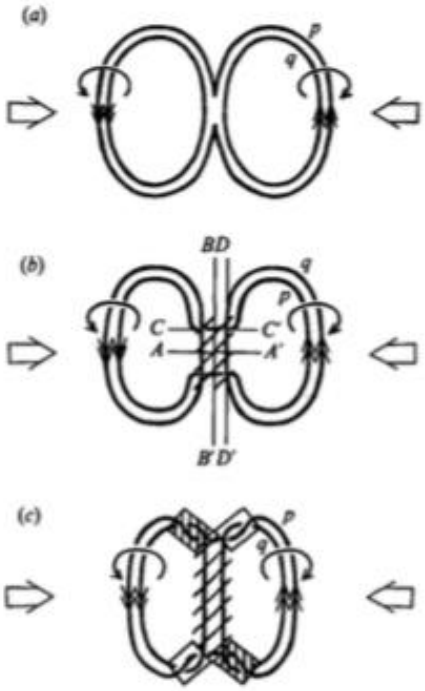

Figure 2.9: Bridging and subsequent reconnection of two vortex rings. Adapted from Kida et al. (1991).

However, since the vortex lines within these bridges are highly curved, their self-induced velocity increases as the bridges grow stronger, eventually causing them to propagate away from each other and discontinuing the vortex reconnection process before all vorticity within each vortex core has had a chance to diffusively interact with that in the opposing core.

A simple model for this cross-cancellation process was proposed by Saffman (1990), the predictions of which were compared to results of numerical simulations by Shelley et al. (1993). The governing principles of this model were that as the vortex cores traveled close together and deformed, viscous diffusion lead to vorticity cancellation. This cross-cancellation process then decreased the rotational and centrifugal forces inside the core, causing a localized increase in pressure which produced a positive strain that

acted to pull the cores further together and accelerate this process of vorticity diffusion and cancellation. A second model for this process was proposed by Kimura & Moffatt (2014). Their model consists of two linearized Burgers-type vortices driven together by an irrotational strain field. In this work, the researchers assumed the vortex-vortex interaction was negligible compared to the uniform strain field and obtained an exponential decay in vorticity with time scale on the order of the strain time scale. Additionally, this time scale was independent of the kinematic viscosity.

The third phase of vortex reconnection deals with the remnants of vorticity, called threads, which are left behind as the bridges pull away from each other. As shown in Figure 2.10, the threads have the form of a curved vortex pair, with a strength much less than that of the original vortex pair.

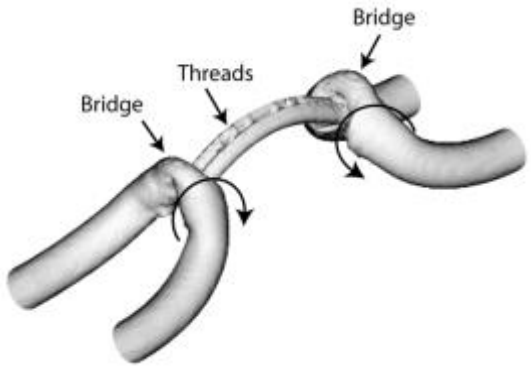

Figure 2.10: Simulation of the reconnection of a vortex pair performed using a triply-periodic spectral method, showing the direction of the induced velocity from cross-linked regions of the vortex cores and the vorticity threads left over from remnants of the core as the reconnected vortices move apart. Adapted from Marshall (2001).

The thread curvature is a result of both the self-induced velocity of the threads on each other and of the velocity induced by the bridges. The thread curvature leads to a weak self-induced velocity that drives the threads towards each other, but this motion is also

influenced by the straining flow induced by the bridges. The velocity induced by the bridges also causes strong stretching of the threads, which intensifies the vorticity within the thread cores. As a consequence of these various effects, the threads appear to remain in contact over a long time but the cross-diffusion between them is slow.

2.3. Vortex Cutting

The term *vortex cutting* refers to a specific type of vorticity reconnection process in which a solid object (such as a turbine blade) passes through the vortex core, forcing vortex lines originating within the vortex to break and reconnect to those within the boundary layer of the solid object. Vortex cutting differs from traditional vortex reconnection problems by the fact that a vorticity generation surface (the surface of the solid body) lies within the reconnection region.

2.3.1 Vortex Cutting: No Axial Flow

The problem of symmetric vortex cutting, with no ambient vortex axial flow, was examined experimentally by Weigand (1993) for the problem of cutting of a vortex ring by a thin plate. Detailed simulation of penetration of a NACA0012 blade into a vortex core was reported by Marshall and Grant (1996) for inviscid flow and by Liu and Marshall (2004) for viscous flow. In these papers, the blade symmetry plane is oriented orthogonal to the vortex core at the point of impact. Cases with varying blade angle of attack were examined in viscous flow simulations by Filippone and Afgan (2008). This previous experimental and computational research exhibits a series of stages of the vortex cutting process. In the early stages of vortex cutting, as the blade leading edge is just

starting to penetrate into the vortex core, the vortex responds in an almost inviscid fashion by reorienting the vortex lines originating within the vortex core to wrap around the blade leading edge. In the inviscid problem, the vortex lines within the vortex cannot be cut in accord with the second Helmholtz vortex law (Marshall, 2001), and they consequently bend around the blade leading edge and stretch, creating a strong vortex sheet, as seen in Figure 2.11 (Marshall and Grant, 1996).

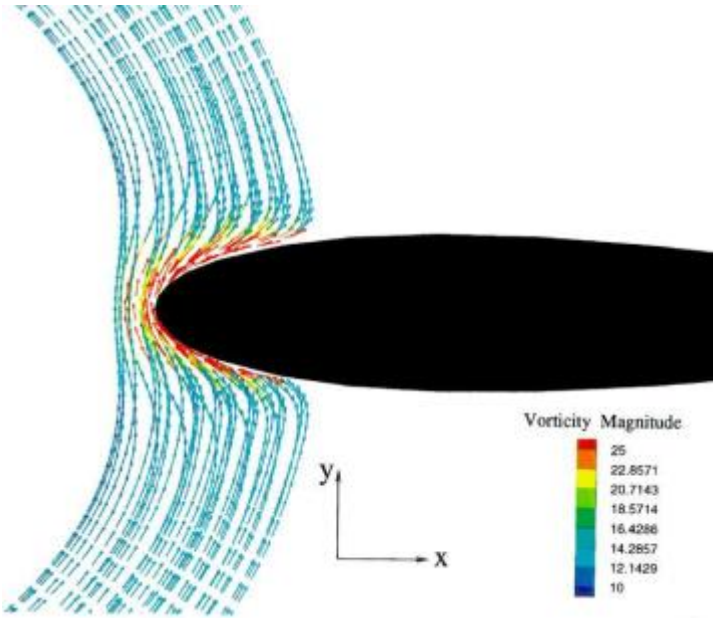

Figure 2.11: Side view of vorticity field showing vortex lines from a vortex ring remaining uncut and wrapping around front of a penetrating blade. Adapted from Marshall & Grant (1996).

In a viscous flow, the vorticity within the vortex near the leading edge diffusively interacts with vorticity of the opposite sign from the blade boundary layer, where the latter is generated by the induced velocity along the blade span generated by the approaching vortex (Figure 2.12). The middle stage of vortex cutting is dominated by this

diffusive cancellation of vorticity of opposite sign between the vortex core and the blade boundary layer, which is what allows vortex lines in the vortex to be cut and to reconnect with vortex lines in the blade boundary layer, in a manner analogous to classic vortex reconnection problems (Kida and Takaoka, 1994; Saffman, 1990).

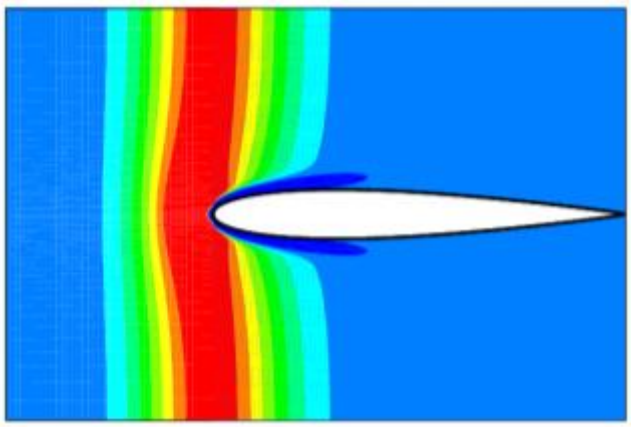

Figure 2.12: Close-up view of blade tip region. Positive vorticity within the vortex core is shown in black and negative vorticity on blade leading edge in grey. Adapted from Liu and Marshall (2004).

When the blade penetrates a sufficient distance into the vortex core, the spanwise velocity induced by the columnar vortex changes direction (Liu and Marshall, 2004). This change in spanwise velocity direction leads to a change in sign of the vorticity orthogonal to the blade plane at the blade leading edge, so that after this point the blade vorticity in this orthogonal direction is of the same sign as that within the vortex core and diffusive cancellation can no longer occur. As a result, the reconnection process between the vortex lines originating within the vortex core and those originating within the blade boundary layer is delayed, and the remaining parts of the vortex wrap around the blade leading edge in the form of a thin sheet, similar to what is observed in the inviscid problem (Figure 2.13). This situation constitutes the late stage of vortex cutting.

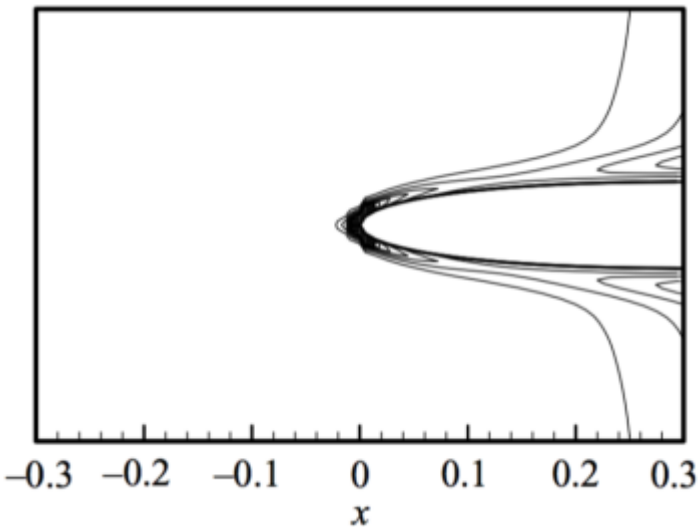

Figure 2.13: Close-up region of blade front. Uncut portion of vortex core is stretched over the blade leading edge. Adapted from Liu and Marshall (2004).

2.3.2 Vortex Cutting: Axial Flow

Cutting (or chopping) of a vortex with non-zero axial flow produces an impulsive lift force on the blade. Vortex cutting is part of the more general process of orthogonal vortex-blade interaction, a review of which is given by Coton et al. (2004). A series of detailed experimental studies of orthogonal vortex-blade interaction and vortex cutting at high Reynolds number have been performed in the wind tunnel at Glasgow University using blade pressure measurements, flow visualization, and particle-image velocimetry (Doolan et al., 1999, 2001; Early et al., 2002; Green et al., 2000; Green et al., 2006; Wang et al., 2002)(Figure 2.14).

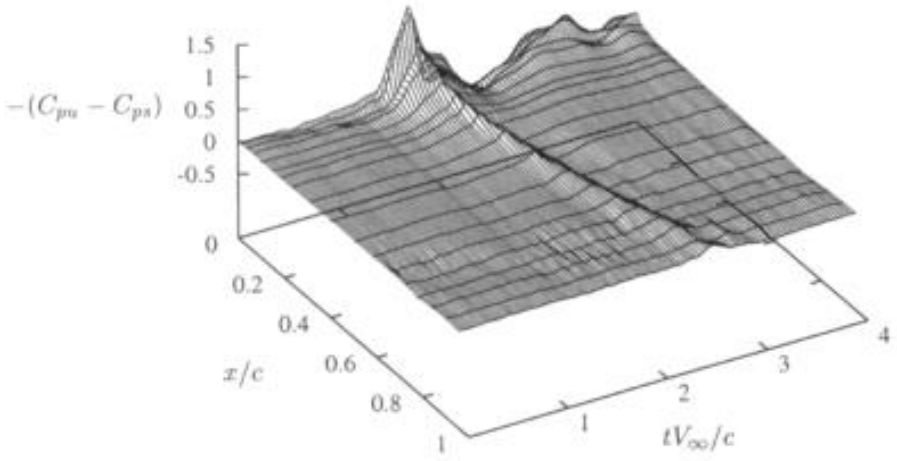

(a)

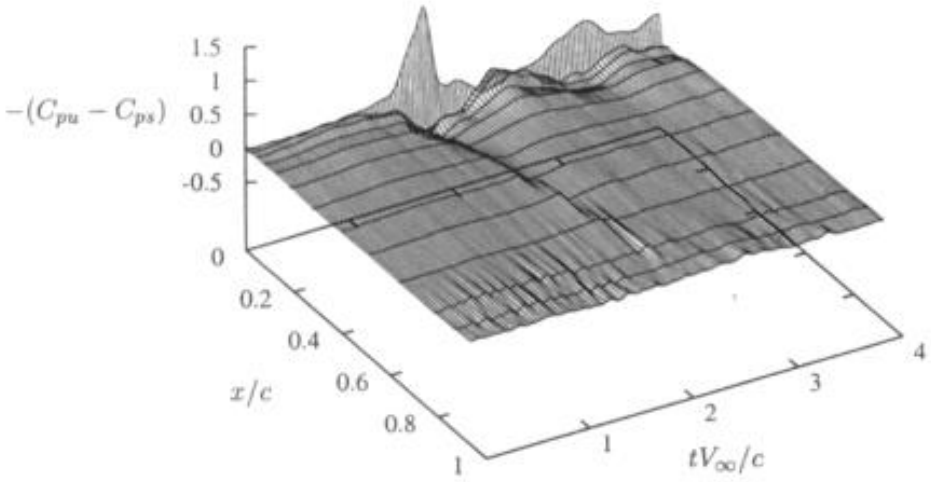

(b)

Figure 2.14: Unsteady pressure measurements on the (a) upper and (b) lower surfaces of a blade during the vortex cutting process. Adapted from Doolan et al. (1999).

Experiments of vortex cutting in water at low Reynolds numbers have also been conducted, which allow for improved visualization using techniques such as laser-induced fluorescence, as reported by Johnson and Sullivan (1992), Krishnamoorthy and Marshall (1998), and Marshall and Krishnamoorthy (1997) (Figure 2.15, Figure 2.16).

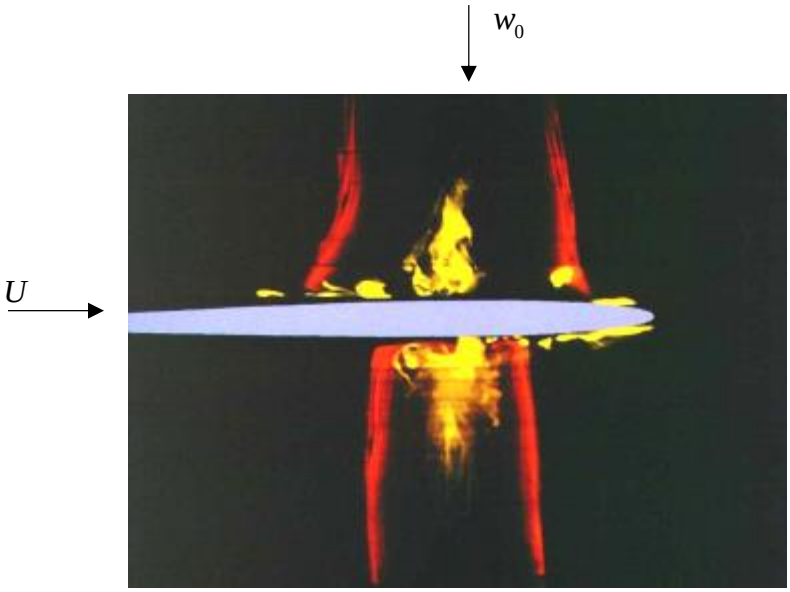

Figure 2.15: LIF image of a blade cutting a columnar vortex in the weak-vortex regime. The blade has velocity *U* and the vortex core velocity is given as w_0. The blade has cut through the vortex core and there is an increase in the vortex core radius on the compression side (blade top) and a decrease in core radius on the expansion side (blade bottom). The yellow fluid, ejected from the boundary layer at the blade leading edge, is entrained into the vortex core. Adapted from Marshall and Krishnamoorthy (1997).

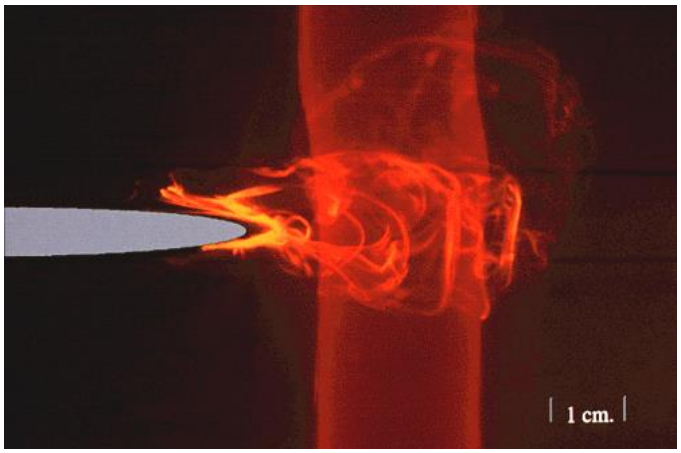

Figure 2.16: LIF (laser-induced fluorescence) image showing a blade approaching a columnar vortex in the strong-vortex regime. A series of secondary hairpin vortices have been ejected from the blade boundary layer and are wrapping around the primary vortex. Adapted from Marshall and Krishnamoorthy (1997)

The effect of vortex cutting on the ambient axial flow within the vortex core was examined using simplified numerical and analytic models by Marshall (1994), Marshall and Yalamanchili (1994), Marshall and Krishnamoorthy (1997), and Lee et al. (1998) and experimentally by Krishnamoorthy and Marshall (1994) and Marshall and Krishnamoorthy (1997). A key feature in many of these papers concerns wave motion induced on the vortex core by the sudden blocking of axial motion within the core during the vortex cutting process. In addition, the presence of instabilities for certain ratios of the swirl to axial velocity within the vortex core has been investigated. Lessen et al. (1974) investigated the inviscid instability of a vortex with axial flow and created a simple theoretical model of the process. Further work on the instability of a vortex with axial flow has been reported by Liebovich and Stewartson (1983) and Mayer and Powell (1992).

Using the plug-flow models for vortex axial flow developed by Lundren and Ashurst (1989) and Marshall (1991), the response of the vortex core to instantaneous cutting by a thin blade was shown to respond in a manner analogous to the classic problem of a suddenly closed gate in a one-dimensional gas flow (Marshall, 1994; Marshall and Yalamanchili, 1994). It is noted that the plug-flow model for axial motion on a vortex core results in a hyperbolic set of equations for vortex core radius and axial velocity that can be mapped into the one-dimensional gas flow equations, and consequently yield solutions analogous to the expansion fans and shock waves of compressible gas flow. Specifically, a ‘vortex expansion fan’ is observed to propagate away from the blade on the downstream side of the vortex (relative to the vortex axial flow), over which the vortex core radius gradually increases from a reduced value near

the blade surface to its ambient value far away from the blade. A compression wave that forms into a 'vortex shock' propagates away from the blade on the upstream side of the vortex, and the vortex core radius close to the blade surface on the upstream side increases relative to the ambient value (Figure 2.17).

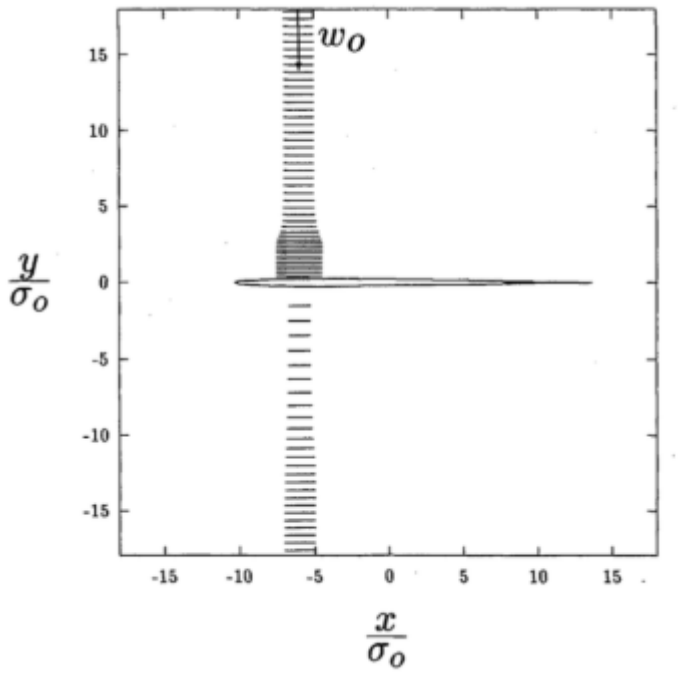

Figure 2.17: Side view of a vortex with axial flow rate after cutting by a blade. A shock forms on the vortex above the blade and an expansion wave forms on the vortex below the blade. Adapted from Marshall and Yalamanchili (1994).

Experimentally, the vortex shock was observed to have the form of a traveling vortex breakdown which translates at the theoretically predicted vortex shock propagation speed (Krishnamoorthy and Marshall, 1994). The difference in vortex core radius on the upstream and downstream sides of the blade leads to a net pressure force in the direction of the ambient vortex axial flow. This *steady-state vortex cutting force* is imposed on the vortex as the vortex is cut and persists throughout the time period following vortex

cutting (Marshall, 1994). Full Euler equation simulations of the inviscid response of a vortex core with axial flow following instantaneous cutting were examined by Marshall and Krishnamoorthy (1997) and Lee et al. (1998) for incompressible flow and by Yildirim & Hillier (2013) for compressible flow, which show good agreement with the plug-flow model predictions for change in core radius and vortex wave speed.

Full viscous simulations of vortex cutting by a blade with non-zero vortex axial flow were reported by Liu and Marshall (2004). The simulations demonstrated that a strong *transient vortex cutting force* is imposed on the blade during the time period in which the vortex is being cut by the blade leading edge, the magnitude of which decreases after the vortex is cut. The magnitude of this transient vortex cutting force was shown by Liu and Marshall to compare well to the experimentally observed lift force on the blade (Wang et al., 2002), even though the Reynolds number between simulation and experiment differed by three orders of magnitude (Figure 2.18).

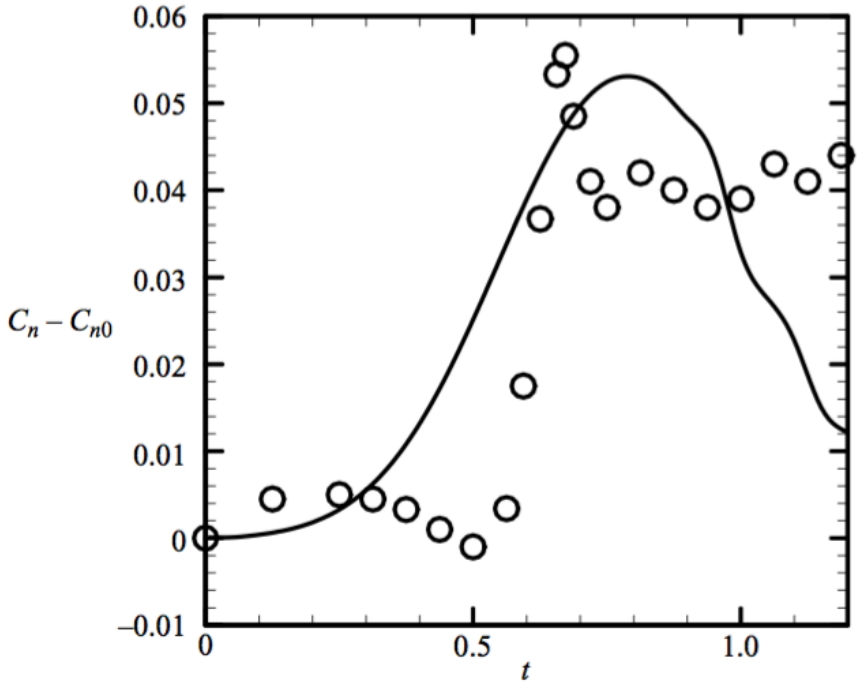

Figure 2.18: Comparison of the computed normal force coefficient (line) with the experimental data of Wang et al. (2002) (symbols). Adapted from Liu and Marshall (2004).

While vortex cutting requires the presence of finite fluid viscosity in order to occur, the observation that computational predictions and experimental measurements of the transient vortex cutting force agree well even when the Reynolds number is vastly different indicates that the transient vortex cutting force is of inviscid origin. In some cases examined, the magnitude of the transient vortex cutting force was found to be much larger than that of the steady-state vortex cutting force derived from the instantaneous plug-flow vortex models. For such cases, the net lift on the blade might be observed to increase to a maximum value equal to the transient vortex cutting force as the leading edge of the blade penetrates into the vortex core, and then to decrease to the steady-state vortex cutting force value after the leading edge of the blade has fully penetrated through

the vortex. On the other hand, if the transient vortex cutting force is smaller than the steady-state force, then the lift on the blade would increase monotonically throughout the vortex cutting process and eventually asymptote to the steady-state force value.

CHAPTER 3: WAKE INTERACTIONS AND FARM LEVEL CONTROL

The first of three studies reported in this dissertation seeks to employ a farm-level control method to investigate the importance of wind turbine wake interactions on the controller for both electric energy maximization and power variability minimization.

3.1 Control Method

The model predictive controller used in this study predicts the behavior of the wind turbines based on a model of the system and a prediction of future wind speeds over a specified time horizon. The aerodynamic thrust and torque on the wind turbine rotor are highly non-linear and cannot be sufficiently approximated by linear models when considering large wind fluctuations over long time horizons. Therefore, a nonlinear model was chosen so that a single plant model and objective function could be used over the entire range of possible wind speed inputs to the farm without loss of accuracy.

3.1.1 Overview of Controller

The controller was implemented using the AMPL (AMPL Optimization Inc) algebraic modeling system and the problem was solved with IPOPT (COIN-OR), a nonlinear program solver. The controller begins by feeding a set of initial conditions, along with a time-series of wind speeds for the upstream turbine, into the controller. The controller then calculates the optimal generator torque and blade pitch angle for all turbines in the wind farm over the length of the time horizon, and the measured wind speeds at the 2nd and 3rd turbines are calculated via an engineering wake model included

within the controller. Once the optimal solution is calculated, the first time step of the solution is implemented as the initial conditions for the next time step. This process was repeated for the duration of the run and is illustrated in Figure 3.1. The nonlinear MPC scheme was not only used to calculate the optimal power solution for the wind farm but was also used to implement the control to the individual turbines, instead of augmenting a standard feedback controller.

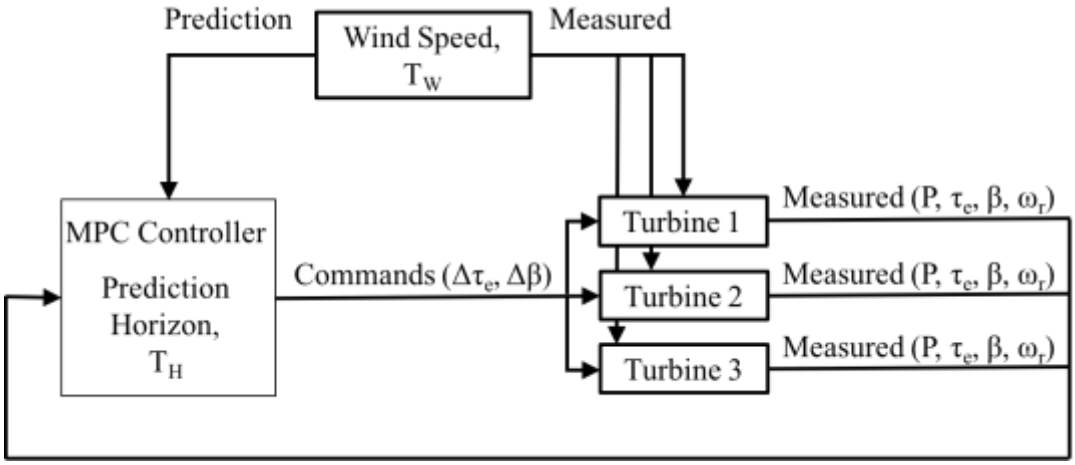

Figure 3.1: Flow diagram for the MPC controller.

In this problem, we assumed collective blade pitch control and perfect wind predictions. A uniform velocity was assumed to be incident to each turbine, which was set equal to the mean velocity over the rotor plane. The state variables for each turbine were the rotational velocity ω_r, the electrical torque τ_e, the wind speed U, the blade pitch angle β, the turbine tip-speed ratio λ, the turbine power coefficient C_p, and the thrust coefficient C_t. The decision variables were the change in electrical torque $\Delta\tau_e$ and the change in pitch angle $\Delta\beta$. The change in predicted wind speed ΔU was modeled as a disturbance. The measured output of the system was the turbine power P. We assumed

that the electrical torque was fully controllable, as would be the case with a type 4 wind turbine which makes use of a full-scale back-to-back frequency converter. Constraints were placed on the different variables to keep the optimizer within a feasible solution space. The constraints were chosen as

$$0 \le \omega_r(t) \le \omega_{r,\max}, \qquad \beta_{\min} \le \beta(t) \le \beta_{\max}, \qquad \left|\dot{\beta}(t)\right| \le \dot{\beta}_{\max}, \qquad 0 \le \tau_e(t) \le \tau_{e,\max},$$

$$\left|\dot{\tau}_e(t)\right| \le \dot{\tau}_{e,\max}. \tag{3.1}$$

The rotation speed was constrained to be less than the rated speed of the wind turbine, $\omega_{r,\max}$. The pitch angle, electrical torque, and their ramp rates were constrained within the rated values for the turbine.

3.1.2 Objective Function

The basic objective function used in the control study included two terms, although alternative formations with a third term to minimize power variability are examined in Section 3.4. The first term of the objective function maximized the electric energy produced by the wind farm; however, this could be easily converted from an energy maximization objective to one that minimizes the deviation from a power set point provided to the wind farm by a Balancing Authority (BA). A problem that can occur with MPC-based wind turbine controllers is that the controller will build up inertia over time and then use this inertia to produce electric energy, thus slowing the turbine near the end of the time horizon. This problem occurs because of the finite length of the time horizon used in the controller. A simple remedy is to add a term in the objective

function that minimizes speed deviations from a fixed value at the end of the time horizon, which acts as a soft constraint on the turbine speed. The objective function was formulated in continuous form as

$$J_1 = -\frac{1}{T_H \omega_{r,\max} \tau_{e,\max}} \int_t^{t+T_H} P dt + \frac{w_1}{\omega_{r,\max}^2} [\omega_r(T_H) - \omega_{r,\max}]^2, \quad (3.2)$$

where w_1 is a prescribed weighting constant and T_H is the time horizon of the controller. The speed deviation in the second term of the objective function was minimized with respect to the maximum rotational speed of the turbine. Additional runs conducted minimizing the speed deviation with respect to the rotational speed at the beginning of the optimization had no measurable difference.

3.1.3 Turbine Model and Simulation Setup

The current study was conducted for a highly simplified farm model that consisted of a set of three, three-bladed horizontal axis, variable-speed wind turbines placed in a line along the prevailing wind direction (Figure 3.2). The turbines were spaced six rotor diameters apart and the wind direction was assumed to remain constant along the line of turbines for the duration of the run. In addition, the downstream turbines were assumed to be fully within the wakes of their immediate upstream neighbor. This model was selected to be representative of how wind turbines in a farm interact with their nearest neighbor turbines. The parameters of the wind turbines were chosen from the 5MW NREL reference wind turbine (Jonkman et al., 2009) and are given in

Table 3.1. This turbine is representative of commercially available turbines and has been extensively used for wind turbine controls research.

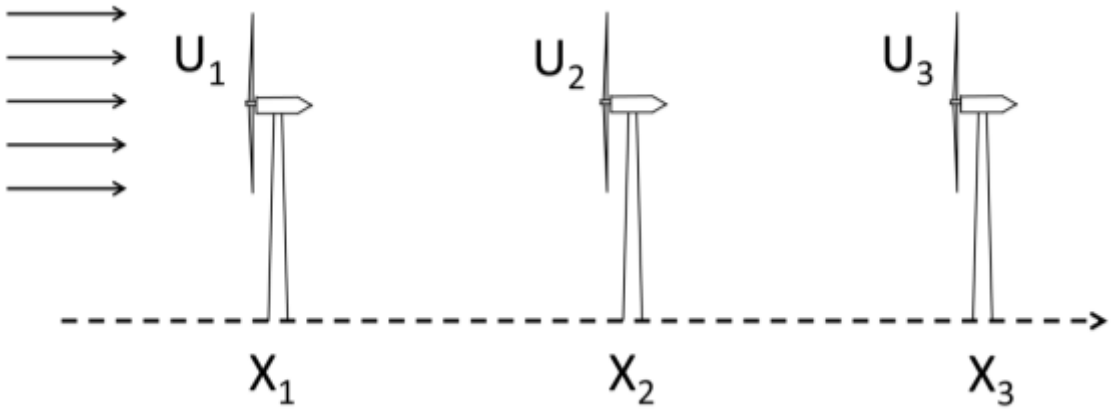

Figure 3.2: Sketch of the three-turbine wind farm considered in this study. Here, x_1, x_2, and x_3 represent the positions of the turbines, and U_1, U_2, U_3 represent the upstream wind velocities at each turbine.

Table 3.1: Parameters used to characterize the wind turbine used in the control study.

Parameter	Variable	Value	Units
Rated Electrical Power	$P_{\max}$	5.3	MW
Minimum Pitch Angle	$\beta_{\min}$	0	deg
Maximum Pitch Angle	$\beta_{\max}$	90	deg
Maximum change in pitch angle	$\left\|\dot{\beta}_{\max}\right\|$	8	deg/s
Rated Electrical Torque	$\tau_{e,\max}$	47,400	N m
Maximum change in electrical torque	$\left\|\dot{\tau}_{e,\max}\right\|$	15,000	N m/s
Rated Rotation Speed	$\omega_{r,\max}$	1.3	rad/s
Gearbox Ratio	N_g	97:1	-
Electrical Efficiency	η_e	0.94	-
Cut-out wind speed	U_{cutout}	25	m/s
Inertia constant of rotor	M_r	35,400,000	kg rad/(m^2 s)
Inertia constant of generator	M_g	530	kg rad/(m^2 s)
Turbine Radius	R	63	m

The power coefficient C_p of the turbine represents the dimensionless power output of the turbine and is defined as (Burton et al., 2008)

$$C_p = \frac{2P_a}{\rho\pi R^2 U^3}, \tag{3.3}$$

where P_a is the aerodynamic power extracted by the wind turbine, ρ is the air density, R is the turbine radius, and U is the upstream velocity of the first wind turbine. The thrust coefficient of the turbine represents the dimensionless thrust force and is defined as

$$C_t = \frac{2F_t}{\rho\pi R^2 U^2}, \tag{3.4}$$

where F_t is the thrust force acting on the turbine. The thrust coefficient C_t and power coefficient C_p are specific to each model of turbine as they depend on the aerodynamic properties of the blades. For the NREL 5MW reference turbine considered in this study, these data were generated from steady-state solutions of the thrust force and aerodynamic power as functions of the pitch angles β and tip-speed-ratios λ using the NREL software FAST. The tip-speed-ratio represents the ratio of the maximum velocity at the blade tip to the inlet velocity and is defined as

$$\lambda = \frac{\omega_r R}{U}. \tag{3.5}$$

The MATLAB curve-fitting toolbox was used to create 3rd order polynomial fits of the thrust and power coefficients as functions of β and λ, which yielded R^2 values of 0.9958 and 0.9984, respectively.

The mechanical and electrical power of the wind turbine are related through the swing equation, which is a form of the rotational inertia equation commonly used to relate the electromagnetic and mechanical torque of a machine. We assumed that the drivetrain was frictionless and neglected the shaft deflections and other dynamics between the slow-speed and high-speed shafts within the gearbox. With these assumptions, the swing equation for the rotor dynamics reduces to

$$(N_g M_g + M_r)\dot{\omega}_r = \tau_a \omega_r - N_g \tau_e \omega_r. \tag{3.6}$$

where M_g and M_r are the generator and rotor inertia constants, N_g is the gearbox ratio of the turbine, and τ_a is the aerodynamic torque on the wind turbine. The values used for

these parameters can be found in Table 3.1. Substituting $P_a = \omega_r \tau_a$ and rearranging (3.3), the aerodynamic torque τ_a can be calculated as

$$\tau_a = \frac{\rho \pi R^2 U^3 C_p(\lambda, \beta)}{2\omega_r}. \tag{3.7}$$

The generator power is given by

$$P = \eta_e \tau_e N_g \omega_r, \tag{3.8}$$

where η_e is the electrical efficiency of the generator.

3.1.4 Engineering Wake Model

The Jensen wake model (Jensen, 1983) was used to represent the effect of the turbine wake on downstream turbines. This model assumes a top-hat shape for the velocity deficit in the wake, where the velocity difference between an upstream and downstream turbine is given by

$$\frac{U_i - U_{i+1}}{U_i} = \left(1 - \sqrt{1 - C_t}\right) \Big/ \left(1 + \frac{\gamma d}{R}\right)^2, \tag{3.9}$$

Here, γ is the wake decay coefficient (given by $\gamma = 0.075$ for on-shore wind farms [40]), d is the spacing between the turbines, and U_{i+1} is the incident wind velocity at turbine

i+1, located downstream of turbine i. Since the system model was chosen to represent how turbines interact with their nearest neighbors, no partial wake overlap or combination of multiple wake models were used. A time delay τ_{td} was employed so that a finite time is required for perturbations introduced at an upstream turbine to propagate to a downstream turbine. The time delay was calculated for each downstream turbine by

$$\tau_{td,i} = \frac{2d}{U_i\left(1-\sqrt{1-C_{t,i}}\right)+U_{i+1}}, \tag{3.10}$$

where $U_i\left(1-\sqrt{1-C_{t,i}}\right)$ represents the velocity directly downstream of turbine i. This model is similar to that proposed by Gonzalez-Longatt et al. (2012) and used by Gebraad et al. (2015).

In order to improve the convergence of the controller and to make the results applicable to different wind turbines, the variables in the problem were non-dimensionalized. The rotational velocity, electrical torque, and blade pitch angle were normalized relative to the maximum rated values for the wind turbine, denoted by $\omega_{r,max}$, $\tau_{e,max}$, and β_{max}, respectively, and the wind speed was normalized relative to the turbine cut-out wind speed U_{cut}. Finally, time was non-dimensionalized using the maximum rated rotation rate $\omega_{r,max}$ of the wind turbine.

3.1.5 Integral Parameters to Assess Performance of Controller

We defined several dimensionless parameters to assess the response of the wind farm power output both to changes in the velocity input and to controller timescales. One

parameter, denoted by Φ, measures the average farm power output, and two other parameters, denoted by Γ and Δ, measure the variability of the farm power output. The parameters are defined mathematically as

$$\Phi = \frac{1}{\omega_{r,\max}\tau_{e,\max}} \frac{1}{T_K} \int_0^{T_K} \left(\sum_{i=1}^{N_t} P_i \right) dt, \tag{3.11}$$

$$\Gamma = \frac{1}{\omega_{r,\max}\tau_{e,\max}} \int_0^{T_K} \left| \sum_{i=1}^{N_t} \frac{dP_i}{dt} \right| dt, \tag{3.12}$$

$$\Delta = \frac{1}{\omega_{r,\max}\tau_{e,\max}} \sqrt{\frac{1}{T_K} \int_0^{T_K} \left(\left(\sum_{i=1}^{N} P_i \right) - \overline{P}_{farm} \right)^2 dt}, \tag{3.13}$$

where T_K is the total run time and $\overline{P}_{farm} = \omega_{r,\max}\tau_{e,\max}\Phi$ is the average farm power output over the time interval from 0 to T_K. The absolute value of farm power fluctuations was used for calculating Γ, so that increases and decreases in power output would both be measured rather than cancelling over the integral. The parameter Δ calculates the root-mean-square (RMS) deviation in power output over the interval from 0 to T_K, and so measures the deviation of power variation but is independent of oscillation frequency.

As previously stated, in this study a single MPC scheme operated both to optimize the power output of a wind farm and to control the torque and blade pitch commands of individual turbines. The time step of the controller and the turbine actuators were assumed to be the same. Independence of the controller predictions to the choice of time step was examined for a case with a sinusoidal wind velocity with a period of 20 seconds, oscillation amplitude of 1 m/s, and mean wind speed of 9 m/s. These parameters

were selected to be typical of conditions examined in the study and to ensure that the wind turbines operated below rated power conditions. The integral parameters listed in (3.11) - (3.13) were calculated for 5 full oscillation periods after the initial start-up time, defined as the time required for the initial velocity signal from the first turbine to propagate to the third turbine. The time steps examined varied from $\omega_{r,\max}\Delta t = 0.04$ to 1.4 with a fixed time horizon of 150. Time step independence was demonstrated by assessing how the measure Γ changed for different time steps. Between $\omega_{r,\max}\Delta t = 0.16$ and $\omega_{r,\max}\Delta t = 0.08$, this measure changed by less than 0.5% and so a time step of $\omega_{r,\max}\Delta t =$ 0.16 was selected. The other integral measures were less sensitive to changes in time step and achieved convergence at larger time steps.

3.2 Wind Farm Performance with Power Maximization Objective Function

Although considerations such as power output variability and turbine damage are important in wind farm operation, control algorithms based on simple electrical energy maximization schemes are often still employed by wind farm operators (Johnson et al., 2009). The first series of tests were performed to examine the case of periodic incident wind, with oscillation period T_W. A series of runs were conducted with different values of the ratio of the MPC time horizon to the incident wind period, T_H / T_W, and the ratio of the time horizon to the time delay, T_H / T_D, where T_D is the time delay between the first and second wind turbine, $\tau_{td,1}$. After accounting for the startup time of the system, the integral measures were calculated for five full periods of the incident wind. A representative case of the three-turbine system with input velocity U, control variables τ_e

and β, and state variables ω_r, λ, and P, are shown in Figure 3.3 for two full periods, with values shown for each individual turbine and the power also shown for the farm as a whole.

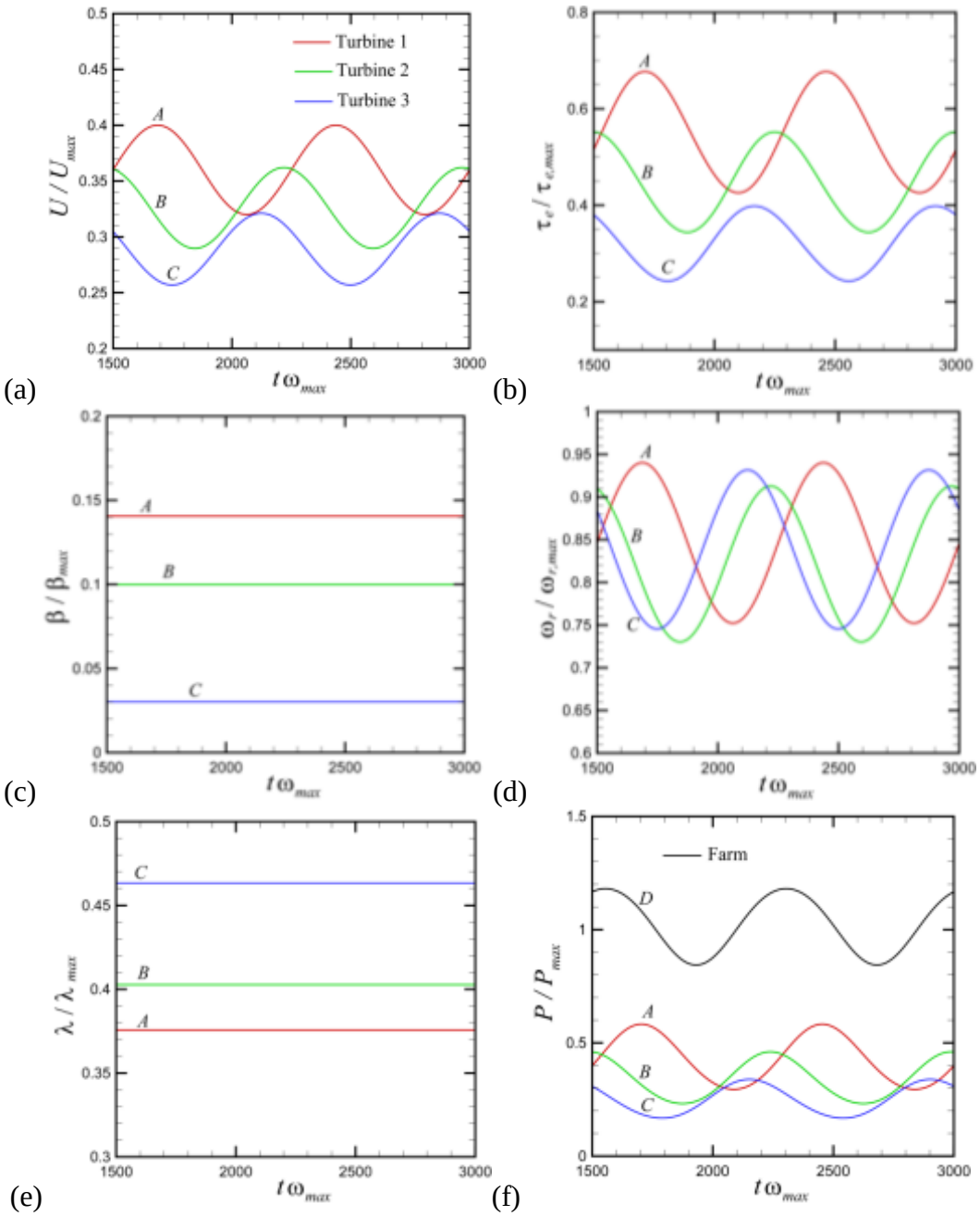

Figure 3.3: A representative case of the three-turbine system, with a) input wind velocity *U*, b) torque *τ*, c) pitch *β*, d) rotation rate *ω*, e) tip-speed-ratio *λ*, and f) power *P* for turbines 1 (A, red line), 2 (B, green line), and 3 (C, blue line). The total farm power is also shown in (f) as line D (black line). Each variable is non-dimensionalized on the *y*-axis and plotted against dimensionless time.

The sinusoidal wind speed input results in nearly sinusoidal outputs for the various control and state variables. The finite delay time introduces a phase difference in the

response curves of the different turbines. It is observed that the blade pitch is nearly constant for each turbine, with the control primarily occurring in the torque variation. This is a result of the turbine being in Region 2 operation; the turbine has not yet reached the rated torque and rotation speed so the turbine works to maximize electric energy production through varying these parameters while the blade pitch is held constant. The variation in collective pitch angles between the three turbines in Figure 3.3 is due to the fact that unlike a standard feedback controller that uses different control laws for different wind speed ranges, the MPC scheme used in this paper uses the same control law over all wind speeds: so the controller was free to decide the optimal pitch angle without any additional constraints.

Results are shown in Figure 3.4a for how the average farm power measure Φ varies with the ratio T_H / T_W for different values of T_H / T_D. The average farm power appears to be independent of the ratio of the time horizon to the period of the input wind signal, which indicates that the time horizon was sufficient for the controller to find the optimal solution. The average farm power exhibited an interesting jump-type of behavior with variation of the ratio of the time horizon to the time delay (Figure 3.4b).

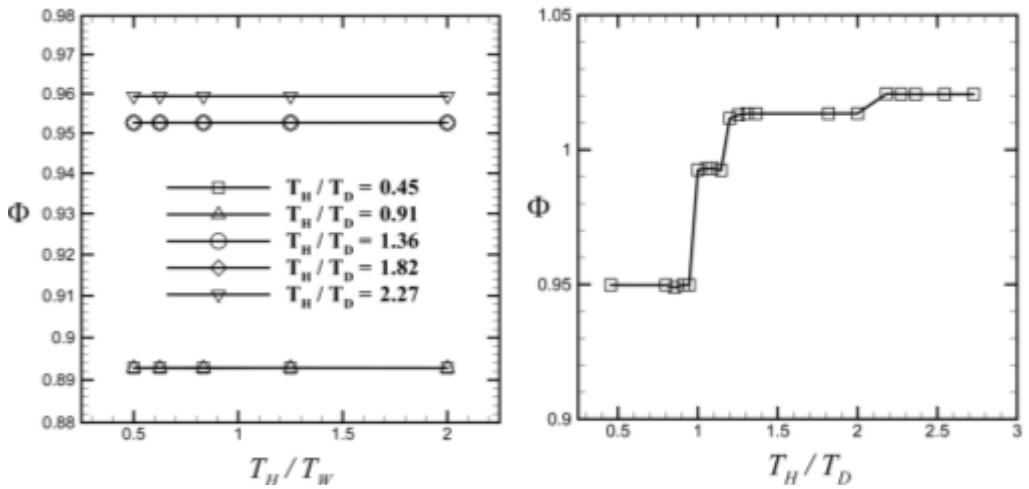

(a) (b)

Figure 3.4: Plots showing average farm power measure Φ as a function of time scale ratios: (a) versus T_H / T_W for different T_H / T_D values and (b) versus T_H / T_D (with T_W = 123 s).

When the time horizon of the controller is less than the delay time between the wind turbines ($T_H / T_D < 1$), the controller operates in greedy mode, where each turbine acts to maximize its own individual power output. As this ratio increases above unity, the average farm power increases in a series of discrete transitions, corresponding to the time at which the first turbine 'sees' the second turbine ($T_H / T_D = 1$), the time at which the second turbine 'sees' the third turbine ($T_H / T_D = 1.2$), and the time at which the first turbine 'sees' the third turbine ($T_H / T_D = 2.2$). In-between each of these transitions, the average farm power is nearly constant with variation in T_H / T_D. This figure clearly shows that the electrical energy generation increases under the MPC algorithm when the time horizon is sufficiently large to include information from multiple turbines, but at the same time the amount of the energy improvement decreases as the distance between turbines increases. The idea that electrical energy output can be increased under certain conditions by upstream turbines shedding power was first proposed by Steinbuch et al. (1988) and

Figure 3.4b illustrates that the majority of energy increases from this approach can come from a decentralized, nearest neighbor approach to turbine control ($1.2 < T_H / T_D < 2$) rather than a centralized, farm level approach ($T_H / T_D > 2$).

The variability of the farm power output was examined by calculating the measures Γ and Δ for the different cases considered. It was found that the fluctuations in farm power output depend mainly on the ratio of the incident wind period to the time delay (T_W / T_D), and exhibited little dependence on the time horizon T_H. Plots of Γ and Δ as functions of T_W / T_D are given in Figure 3.5a and Figure 3.5b, and the two curves are found to have very similar shapes.

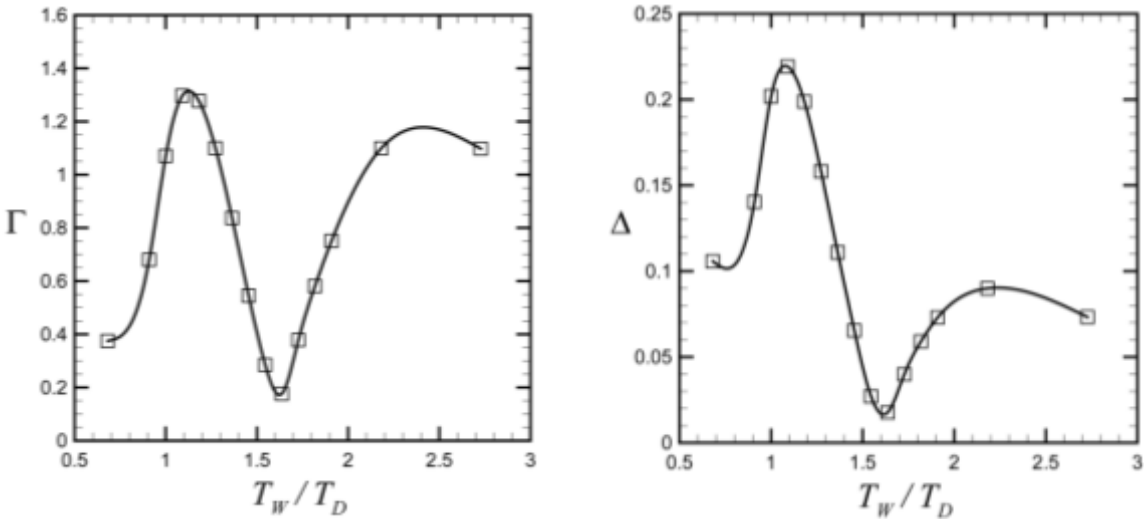

Figure 3.5: Plots showing power variability measures (a) *Γ* and (b) *Δ* as functions of the time scale ratio T_W / T_D.

By varying the ratio of the incident wind period to the time delay, the relative phase of the input velocities to the three turbines was shifted. This phase shift in velocities causes a phase shift in the power output signals, leading to both constructive ($T_W / T_D = 1.1$) and destructive ($T_W / T_D = 1.6$) interference, without including any control for power

variability within the objective function of the controller. Time series illustrating the power variation for the individual turbines and for the farm as a whole in cases with both constructive and destructive interference are shown in Figure 3.6. The small kink at the top of turbine A's power curve is due to the controller switching between varying the electric torque of the turbine and varying the pitch angle of the turbine blades. This transition in control regimes occurs since it is more efficient for the controller to vary the electrical torque at low power output and to switch to varying the blade pitch angles at higher power output.

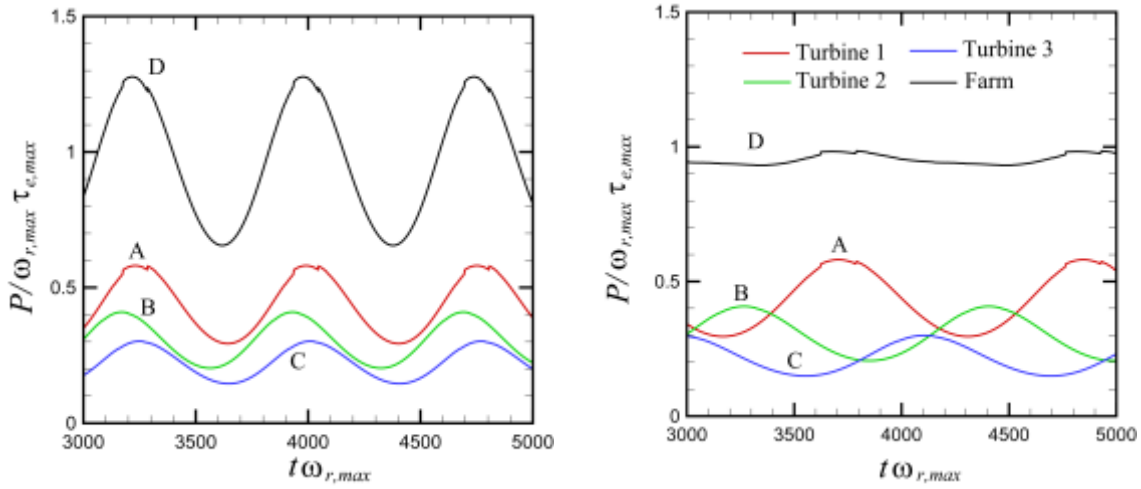

Figure 3.6: Plots showing the interference in dimensionless power output between the three wind turbines (labeled A-C) resulting in (a) constructive (T_W / T_D = 1.1) and (b) destructive (T_W / T_D = 1.6) interference. Curve colors and letters are the same as in Figure 3.3. The total farm power output is plotted as curve D (black).

3.3 Wind Farm Performance with Realistic Wind Data

We next investigated if the trends observed in our controller with the sinusoidal wind velocity were still present in cases with a more complex wind velocity input. Wind data with a resolution of one second was obtained from a wind farm operator, and a 22-

minute subset of this data was used as the inlet velocity for the first (most upstream) wind turbine, while the inlet velocities for the second and third wind turbines are predicted using the Jensen wake model. In practice, the combination of a large swept rotor area and large moment of inertia for an actual wind turbine attenuates many of the high-frequency fluctuations in wind speed (Nakamura et al., 1995). While the rotor inertia is included within the modeled turbine dynamics in (3.6), a low-pass filter was introduced to address the spatial filtering of the large swept rotor area of actual turbines. The upper cutoff frequency was calculated as

$$f_{cutoff} = \frac{U_{mean}}{D_o}, \tag{3.14}$$

such that U_{mean} is the average velocity of the signal and D_o is the diameter of the wind turbine. The filtered velocity is shown as a function of time in Figure 3.7a, and a power spectrum of the filtered data is plotted in Figure 3.7b (on a log-log plot). A line was fit to the power spectrum, which was found to have a slope of -1.8. The theoretical value of the slope of the power spectrum is obtained using the Kolmogorov scaling as -5/3 = -1.66$\overline{6}$; however, typical experimental values obtained for the power spectrum slope for ground-level wind in an atmospheric boundary layer range between -5/3 to -2 (Malik et al., 1996). The observed slope of -1.8 from our data was therefore within the expected region for atmospheric turbulence.

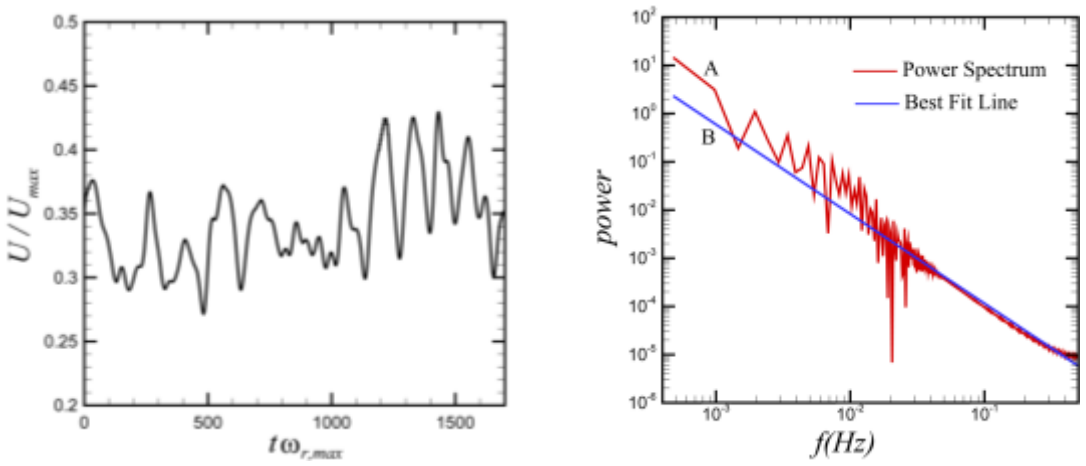

(a) (b)

Figure 3.7: Plots showing (a) input wind velocity and (b) power spectrum of velocity data (A, red line). A best-fit line with slope -1.8 (B, blue line) is also shown.

Unlike the sinusoidal velocity signal used in Section 3.2, the velocity input used in this section had no single dominating period. A typical time scale T_W of the incident wind can be estimated using the approximation,

$$T_W = \sqrt{\frac{m_0}{m_2}} \tag{3.15}$$

where m_0 and m_2 are the zeroth and second spectral moments, respectively. These spectral moments are given by

$$m_i = \sum_{n=1}^{n_b} f_n^i S(f_n) df_n \ , \tag{3.16}$$

where n_b is the number of discrete frequency bins, f_n is a given frequency, $S(f_n)$ is the spectral density at a given frequency, and $d(f_n)$ is the bandwidth of each frequency band. The time scale estimation method is similar to that used for wave buoys, as noted by

Earle (1996). For the wind velocity data shown in Figure 3.7, this method yields T_W = 123 s.

A series of tests were performed to examine the case of realistic incident wind with an electrical energy maximization objective function. Similar to the sinusoidal incident wind case, a series of runs were conducted with different values of the ratio of the MPC time horizon to the incident wind period, T_H / T_W, and the ratio of the time horizon to the time delay, T_H / T_D. After accounting for the startup time of the system, the integral measures in (3.11) - (3.13) were calculated for the full duration of the signal, which in this case is approximately equal to $11T_W$. A representative case showing input velocities, control variables, and state variables are shown in Figure 3.8, with values shown for each individual turbine and the power also shown for the farm as a whole. The incident wind period was varied by interpolating the original wind signal onto a stretched time vector, and then passing this new velocity signal through a low-pass filter. The slope of the power spectrum for these altered wind data signals was then calculated. For all cases considered the slope was found to be within 0.7% of the slope for the original wind data signal. Since the power spectrum slope of these signals all fell within the expected range for atmospheric boundary layer turbulence, the stretched wind signals can be taken to still be representative of realistic wind velocity inputs.

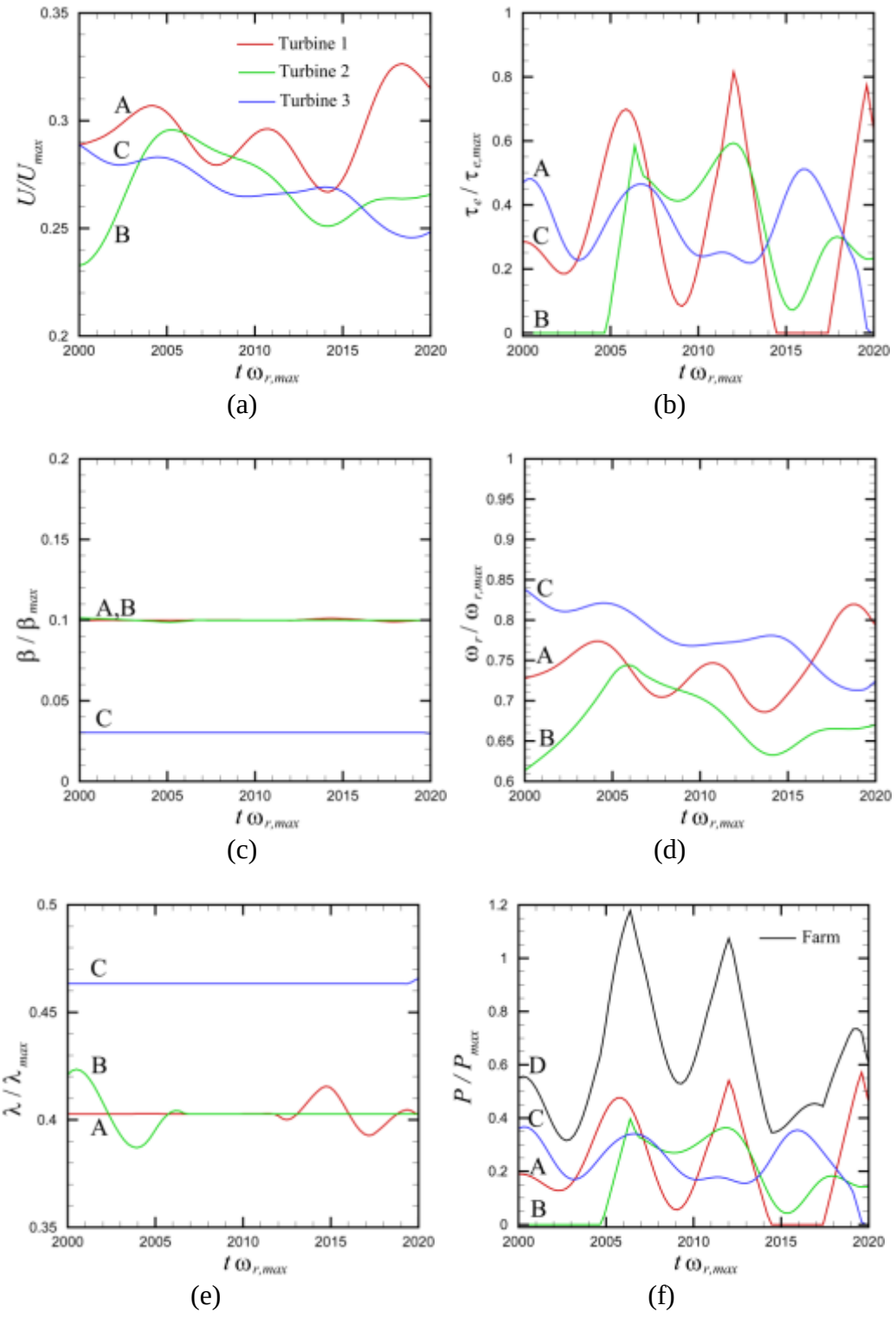

Figure 3.8: A representative case of the three-turbine system, with a) realistic wind velocity *U*, b) torque *τ*, c) pitch *β*, d) rotation rate *ω*, e) tip-speed-ratio *λ*, and f) power *P* for turbines 1 (A, red line), 2 (B, green line), and 3 (C, blue line). The total farm power is also shown in (e) as line D (black line). Each variable is non-dimensionalized on the *y*-axis and plotted against dimensionless time.

The farm power output was found to be relatively independent of the ratio T_H/T_W, varying by a maximum of 0.17% between cases. The system did exhibit interesting behavior in the average farm power Φ as the ratio T_H / T_D varied (Figure 3.9). A series of discrete transitions occurred, similar to those for the sinusoidal incident wind, and these three transitions corresponded to an increase in power generation of 5%, 2% and 0.5%, respectively. This indicates that for realistic incident wind, the farm power generation from an MPC approach will increase when the time horizon is long enough to incorporate the dynamics between turbines, but with diminishing returns for subsequent turbines after the nearest neighbors.

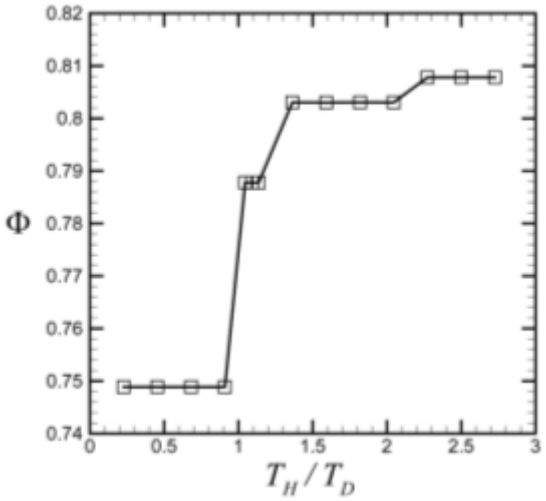

Figure 3.9: Plot showing average farm power measure Φ as a function of T_H / T_D (with T_W = 123 s).

The average farm power for the longest time horizon from these tests was Φ=0.81 which is slightly lower than the average farm power for the same time horizon with the sinusoidal wind input in Figure 3.4a, Φ=1.02. This decrease in average farm power is likely due to the decrease in average wind velocity of the realistic wind input signal (U_{avg} / U_{max} = 0.34) compared to the sinusoidal wind input signal (U_{avg} / U_{max} = 0.35). A time

series of the upstream velocities at the three turbines is given in Figure 3.10. The average farm power increase is due to the first turbine shedding power, leading to an increase in wind velocities at the 2nd and 3rd turbines. The computation time of the optimizer was found to be most dependent on the time horizon employed. The computation time for each second of data simulated ranged from 6 s for the smallest time horizon of T_H = 25 to 86 s for the largest time horizon of T_H = 300. For the standard horizon of T_H = 150 employed later in the study, the optimizer required 26 s of computation time per second of simulated data.

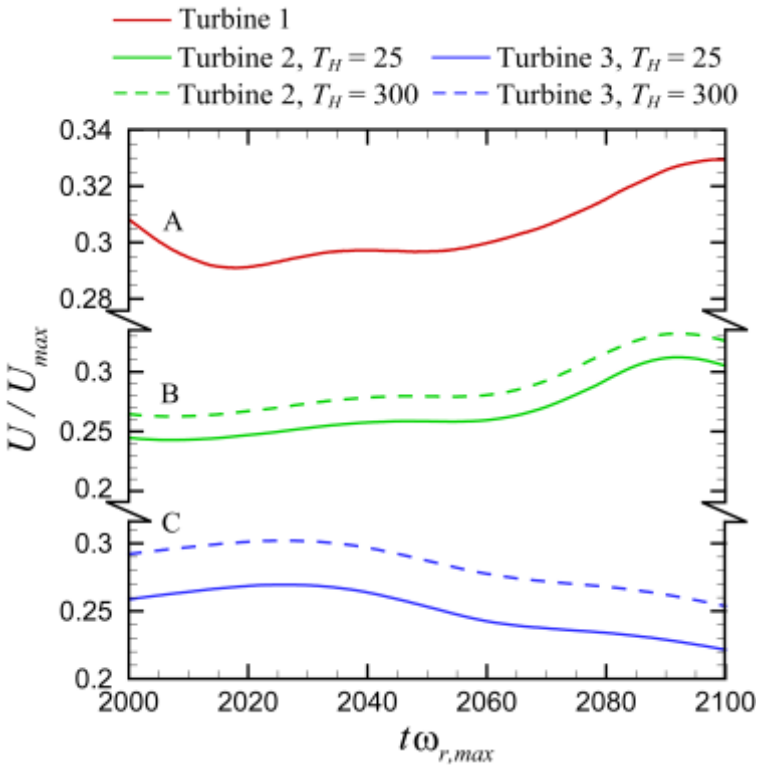

Figure 3.10: Plot illustrating the effect of the controller time horizon on the upstream velocities of turbine 2 (blue) and turbine 3 (green) for greedy control (T_H = 25, solid line) and cooperative control (T_H = 300, dashed line). The cooperative control case resulted in an 8% increase in average farm power over the greedy control for the same input velocity at turbine 1 (red).

In addition to the farm power output, the variability in power output was assessed by calculating the integral measures Γ and Δ. It was again found that the fluctuations in farm power output mainly depend on the ratio of the incident wind period to the time delay (T_W / T_D), with values that are relatively independent of the time horizon T_H. Both measures indicate that as the ratio T_W / T_D is varied, the farm power output experiences both constructive and destructive interference relative to the original signal (T_W / T_D = 1.12). Unlike the sinusoidal case, the realistic wind velocity contained fluctuations over multiple periods. Therefore, the effects from constructive and destructive interference for different values of the ratio T_W / T_D were significantly less, with the integral measure Γ varying from 11.1 to 13 and Δ varying from 0.324 to 0.339.

3.4 Effect of Power Variability Minimization in the Objective Function

While simple power maximization objective functions are still often used by wind farm operators, multi-objective controllers are now being explored. These controllers allow for additional objectives such as minimizing power output variability or turbine fatigue damage. A systematic study was conducted to characterize the response of the controller with an additional power variability minimization term added to the objective function. The variability term is added to the electrical energy maximization term as an additional objective with a tunable weighting parameter. Two different formulations for the variability term were introduced and the performance of each separate objective formulation was evaluated across the time scale ratios previously introduced in Section

3.3. The first formulation controlled for minimizing the square of farm power fluctuations, so the additional term added to the objective J_1 in (3.2) is given by

$$J_2 = \frac{w_2}{T_h}\int_t^{t+T_h}\left(\sum_{i=1}^{N_t}\frac{dP_i}{dt}\right)^2 dt, \tag{3.17}$$

where w_2 is the weighting parameter. This objective is similar to that employed by DeRijcke et al. (2015); however, they did not estimate the power derivative using the difference between subsequent time steps but instead use a specified time interval. A similar measure of controlling for power fluctuations between successive time steps was introduced by Clemow et al. (2010), and in their formulation they took the absolute value of the power fluctuations and normalized by the average farm power. The second formulation for minimizing farm power variability was defined as

$$J_3 = \frac{w_2}{T_h}\int_t^{t+T_h}\left(P_{avg} - \sum_{i=1}^{N_T}P_i\right)^2 dt, \tag{3.18}$$

where P_{avg} is calculated from

$$P_{avg} = \frac{1}{T_h}\int_{t-T_h}^{t}\left(\sum_{i=1}^{N_T}P_i\right)dt. \tag{3.19}$$

Unlike the first form, this term did not measure the fluctuations between time steps but instead measured the variance from the farm power averaged over the previous time horizon window, and is similar to the signal tracking objectives that are commonly employed in many control systems.

The first series of tests were conducted to examine how the controller responded to realistic wind data as the relative weighting on the variability term w_2 increased. Runs were conducted with various values of w_2 and the performance assessed by calculating the three integral measures defined in (3.11) - (3.13). As w_2 increased from the initial

value of 0.01, the average farm power output gradually decreased for J_2 (Figure 3.11a). At a value of w_2 = 100, the average farm power decreased by 0.56% for J_2. In contrast, J_3 experienced a sharp decrease in average farm power above w_2 = 0.03 and at w_2 = 0.1, the average farm power decreased by 1.06% (Figure 3.11a).

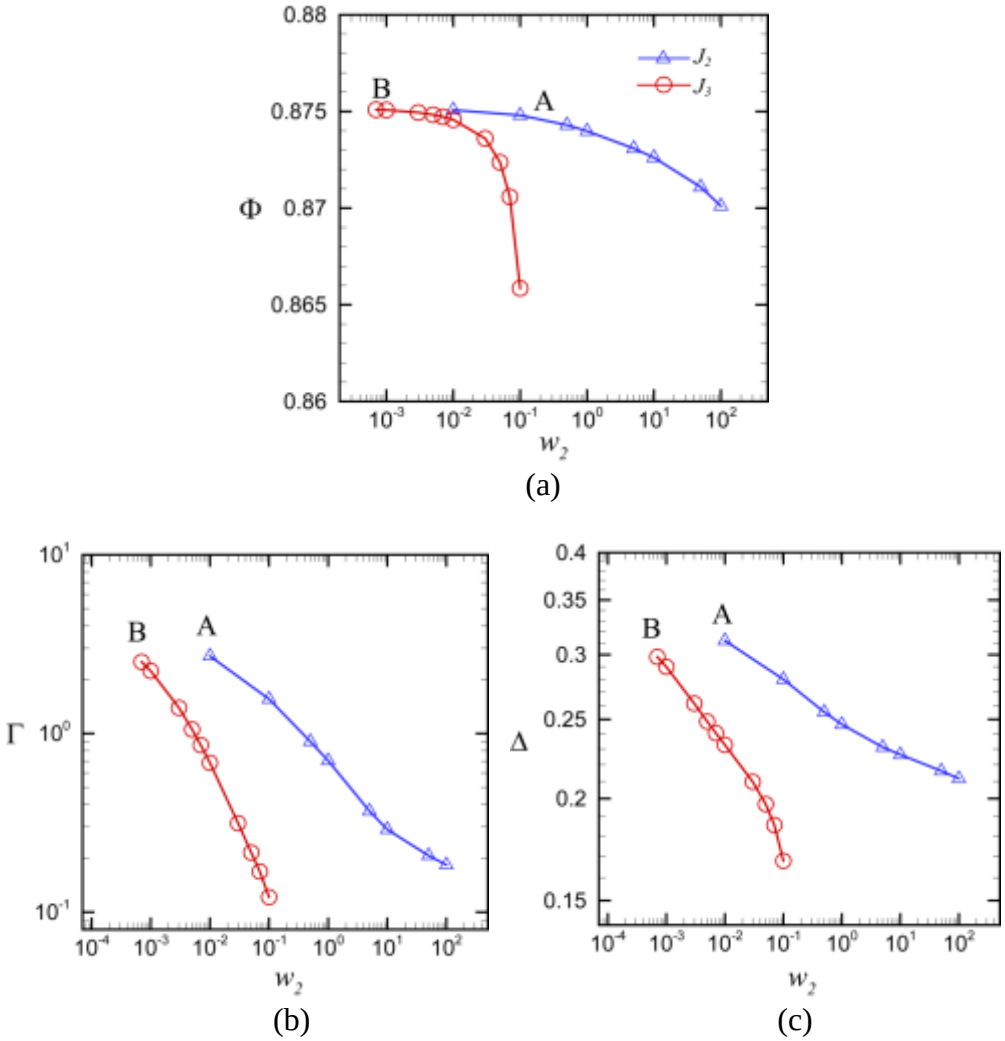

Figure 3.11: Plots showing (a) average farm power measure Φ, (b) power variability measure Γ, and (c) power variability measure Δ as a function of variability weighting parameter w_2 for objective functions J_2 (A, blue squares) and objective function J_3 (B, red circles).

The variability in farm power output was again examined by calculating how Γ and Δ responded as w_2 changed. It was found that for both objective functions Γ decreased by roughly an order of magnitude as w_2 increased from 0.01 to 100 for objective J_2 (Figure 3.11b) and 0.001 to 0.1 for objective J_3 (Figure 3.11b). As shown in Figure 3.11c, Δ decreased by about 30% over the same range of weights for both objectives. The effect of increasing w_2 on the farm power is further illustrated in Figure 3.12a-b for objectives J_2 and J_3.

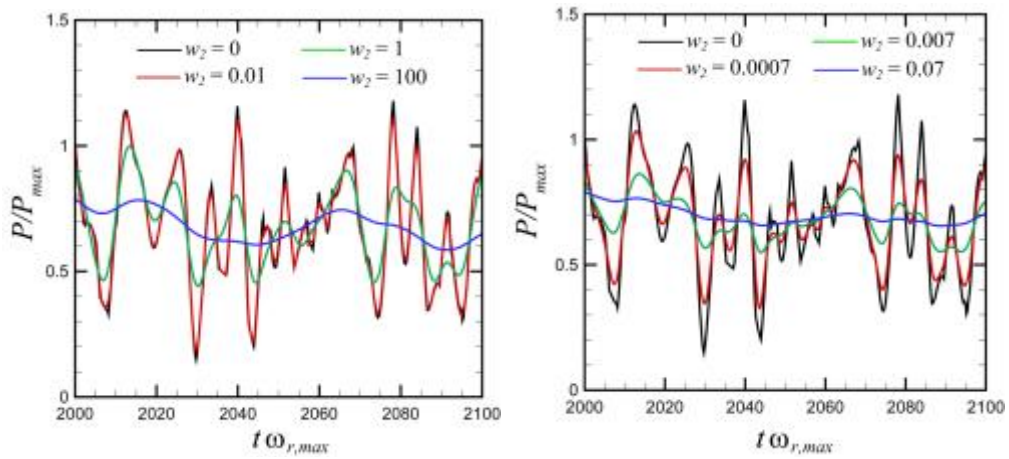

Figure 3.12: Plots showing the effect of the weighting parameter w_2 on the farm power output for (a) objective function J_2 where the colors correspond to $w_2 = 0$ (black), $w_2 = 0.01$ (red), $w_2 = 1$ (green), and $w_2 = 100$ (blue) and for (b) objective function J_3 where the colors correspond to $w_2 = 0$ (black), $w_2 = 0.0007$ (red), $w_2 = 0.007$ (green), and $w_2 = 0.07$ (blue).

While both objectives achieved a significant reduction in farm power intermittency with only a slight reduction in average farm power output, they did not accomplish this in the same way. Objective J_2 reduced the variability of the farm power output by smoothing the power output of individual wind turbines as can be seen in Figure 3.13b. Instead, objective J_3 used constructive and destructive interference between the individual turbines to achieve a reduction in farm power output variability, as shown in Figure

3.13c. For this objective, the power variability from the individual turbines did not change appreciably from the original signal (Figure 3.13a); however, the timing of the increases and decreases of the individual turbine power outputs have been adjusted by the controller to result in a significant reduction in the net farm power variability.

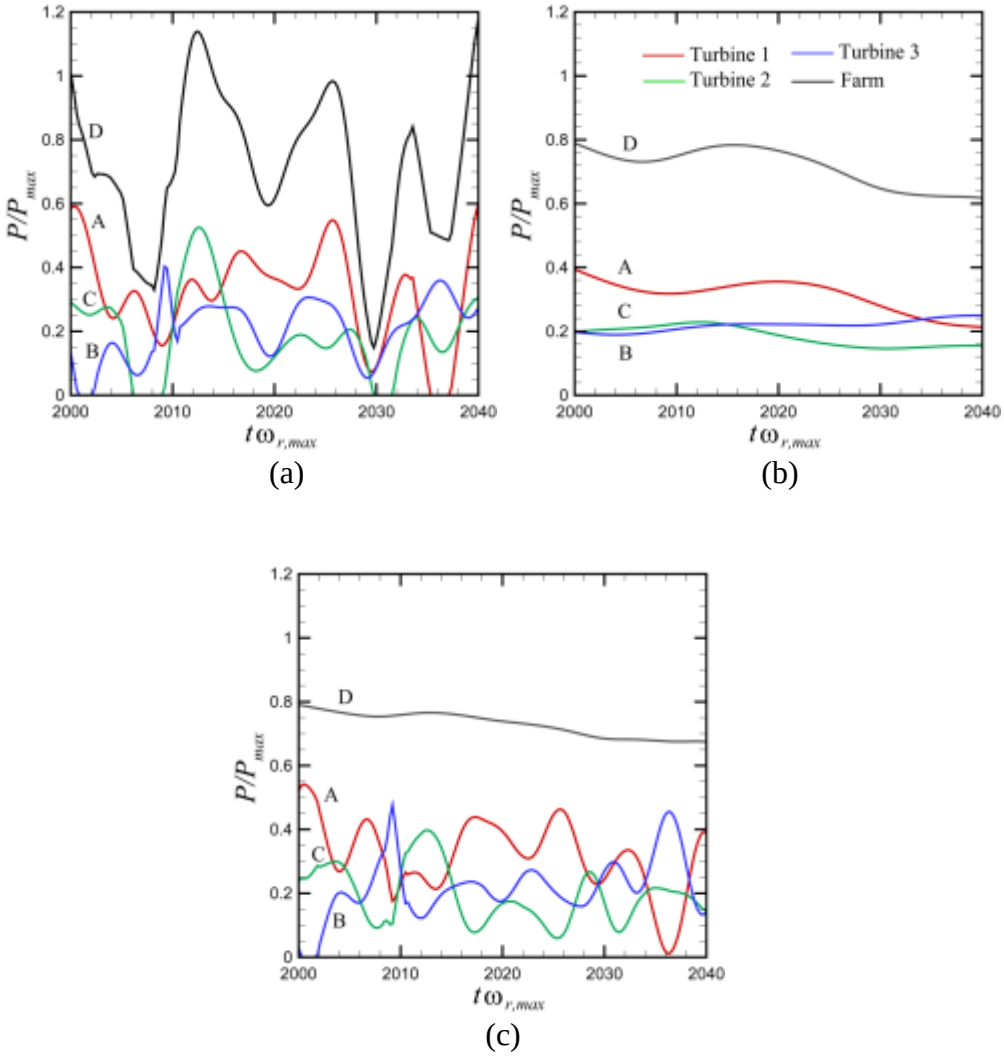

Figure 3.13: Plots illustrating the different methods used by the objective terms to minimize power variability. The farm power output (black line) is plotted in addition to the individual powers from turbine 1 (red line), turbine 2 (blue line) and turbine 3 (green line). The variability in the original signal (a) is reduced by smoothing the fluctuations in individual turbine power outputs for J_2 (b) and by altering the amplitudes of the individual power outputs for J_3 (c).

The final series of tests were conducted to examine how the multi-objective controllers responded to varying the ratio of the MPC time horizon to the incident wind period, T_H / T_W, and the ratio of the time horizon to the time delay, T_H / T_D. Discrete transitions in the average farm power Φ were again observed for both objective J_2 and objective J_3 (Figure 3.14a) as the time horizon T_H increased relative to the time delay between wind turbines T_D. However, unlike for the simple power maximization objectives, in these tests these transitions corresponded to similar decreases in farm power variability measure Γ for both objective J_2 and for objective J_3 (Figure 3.14b). This indicates that when explicitly controlling for variability of farm power within an objective function, it is important for the time horizon of the controller to be long enough to see neighboring turbines.

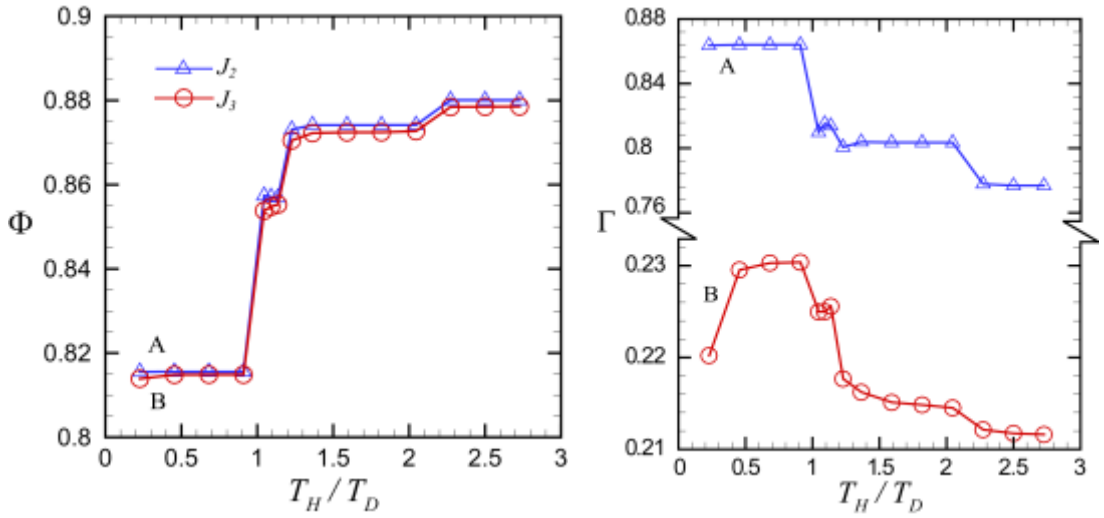

(a) (b)

Figure 3.14: Plots showing (a) average farm power measure Φ and (b) variability measure Γ as a function of T_H / T_D (with T_W = 123 s) for objective J_2 (A, blue squares) and objective J_3 (B, red circles).

One exception to this trend is the first point for objective J_3 in Figure 3.14b. As the ratio T_H / T_D increases from 0.2 to 0.45, the variability measure Γ increases from 0.22 to 0.23,

indicating that the variability in farm power initially increases as the time horizon increases. For this case, the controller finds that an increase in farm power variability will result in a small increase in average farm power (Figure 3.14a). This trade-off depends on the relative weighting between the power maximization and variability minimization objectives and is not observed in any other cases. The variability measure Δ remained relatively constant for objective J_2 as the ratio of T_H / T_D increased, only changing by a maximum of 0.7%, and for objective J_3 it followed a similar trend to the Γ measure. Similar to the previous cases examined, the average farm power Φ was found to be relatively independent of the ratio T_W / T_D, only changing by a maximum of 0.19% for objective J_2 and 0.17% for objective J_3. However, for certain values of this ratio both constructive and destructive interference were again observed for objectives J_2 and J_3. This interference was most prominent in the Γ measure, and has less of an effect on the Δ measure, as can be seen in Figure 3.15a for Γ and Figure 3.15b for Δ. Instead of periods of constructive and destructive interference, the Δ measures gradually increased as the ratio of T_W / T_D increased which is likely due to the larger wind periods having a larger root-mean-square value for a given time step.

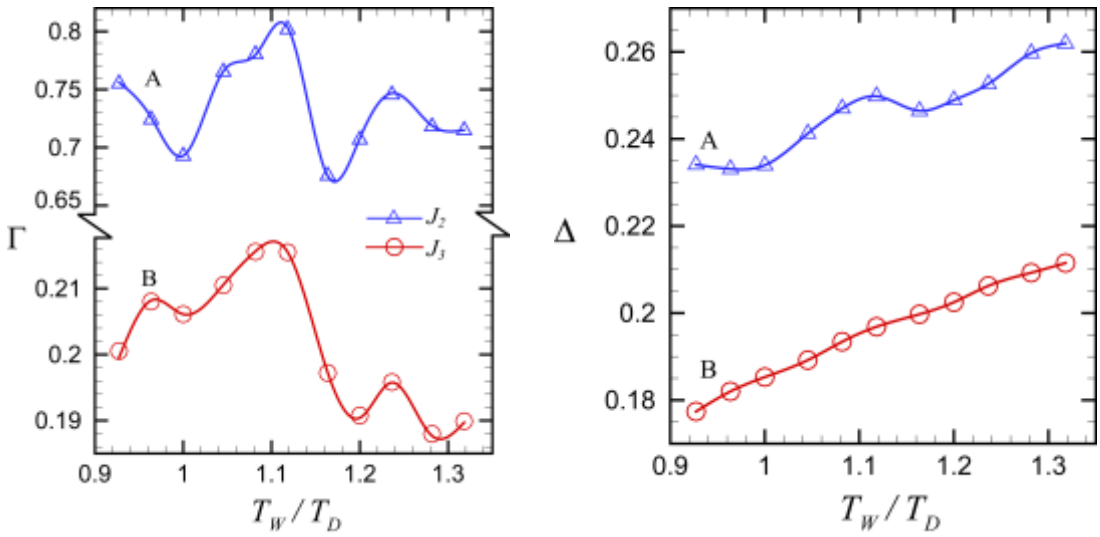

(a) (b)

Figure 3.15: Plots showing (a) variability measure Γ and (b) variability measure Δ as a function of T_W / T_D (with T_H = 150 s) for objective J_2 (A, blue squares) and objective J_3 (B, red circles).

3.5. Conclusions

The nonlinear MPC strategy presented serves as a means to explore both the potential and the limits of farm level controllers as different timescales in the problem are varied. First, a controller with a simple electrical energy maximization scheme was introduced and significant changes in farm power output variability were achieved depending on the ratio of the period of the wind input and the time delay between wind turbines, both for a sinusoidal wind velocity and for a realistic wind velocity. The average farm power output increased as a series of discrete transitions as the time horizon of the controller increased relative to the time delay between turbines. This can be attributed to the increased time horizon allowing for the controller to 'see' neighboring turbines.

Two measures characterizing the farm power variability were introduced and each was incorporated into the objective function of the controller. The effect of the relative

weightings between the electrical energy maximization and variability minimization terms was examined, and it was found that significant reductions in farm power variability could be achieved through coordinating the power fluctuations in the individual turbine power outputs without significant reductions in average farm power output. Furthermore, the controller was found to utilize two different methods to achieve variability reduction depending on the formulation within the objective function. If the objective function was formulated to minimize the time derivative of the power fluctuations, the controller smoothed the power curves of the individual wind turbines. However, if the objective function was formulated to minimize the variance in farm power relative to the past mean power output of the plant, the controller utilized constructive and destructive interference between the individual turbines to smooth the net farm power output. Finally, it was found that both the variability and average power output of a combined electrical energy maximization and variability minimization controller were affected by the ratio of the time horizon to the time delay between wind turbines. As the time horizon increased so that the controller could 'see' neighboring turbines, the average farm power increased and the variability in farm power output decreased.

CHAPTER 4: VORTEX LINE RECONNECTION DURING VORTEX CUTTING

As discussed in Chapter 1, the interaction of turbine blades with vortex structures contained within upstream turbine wakes contribute to the stochastic loadings on wind turbine gearboxes and high-speed shafts. In the next two chapters, aspects of the orthogonal vortex-blade cutting process are examined in order to better understand the fundamental physics of the vortex-cutting process and to aid in the development of simple models to describe and predict the unsteady vortex-wake loading. The relation of the vortex-cutting process to the vortex reconnection process is examined, specifically whether the same parameters and timescales govern both processes. In addition, the transient vortex cutting force is examined through a combination of Navier-Stokes simulations, scaling analysis, and heuristic model in order to understand the relation between the force and the main dimensionless parameters of the flow.

4.1 Introduction

In this chapter, the relationship between dimensionless parameters and timescales which govern the breaking and rejoining of vortex lines in the vortex cutting problem is investigated and these findings are compared to the classical vortex reconnection problem. In particular, this study seeks to determine whether the same parameters and time scales that govern the breaking and rejoining of vortex lines in the classical vortex tube reconnection problem also govern the vortex cutting problem, and whether the different phases of the vortex reconnection problem (see, e.g., Kida and Takaoka, 1994, or Shelley et al., 1993) have analogues in the vortex cutting problem. The

investigation is conducted using two different approaches. The first approach consists of a series of high-resolution simulations of vortex cutting by a blade with no ambient axial flow within the vortex and with different values of the *impact parameter I*, defined in terms of the vortex-blade relative velocity *U*, the vortex core radius σ, and circulation Γ by $I = 2\pi\sigma U/\Gamma$. The temporal and spatial variation of pressure, vorticity, surface vorticity flux, and stretching and reconnection of vortex lines are examined to understand how these measures compare to similar measures in the literature on colliding vortex tubes. In the second approach, a highly simplified model that examines the vorticity diffusive cancellation process between an incident vortex (a stretched vortex sheet) and vorticity generated from a no-slip surface is presented. The model is made analytically tractable by 'unwrapping' the blade surface, so that the vortex-blade interaction very close to the blade leading edge is represented by the problem of a stretched vortex sheet interacting with a flat surface in the presence of a straining flow. While this model is a bit too simplified to provide accurate quantitative comparison with the full Navier-Stokes vortex cutting simulation, as an exact Navier-Stokes solution it is useful for suggesting parameter scalings and for illustrating the physics of the vorticity cross-diffusion process in the presence of a no-slip surface.

4.2 Numerical Method

The Navier-Stokes equations were solved in primitive-variable form using a finite-volume method (Lai, 2000) and a block-structured mesh with hexahedral elements. The domain consisted of four implicitly coupled blocks and was designed to achieve high

spatial resolution along the leading edge of the blade and along the blade boundary layer (Figure 4.1).

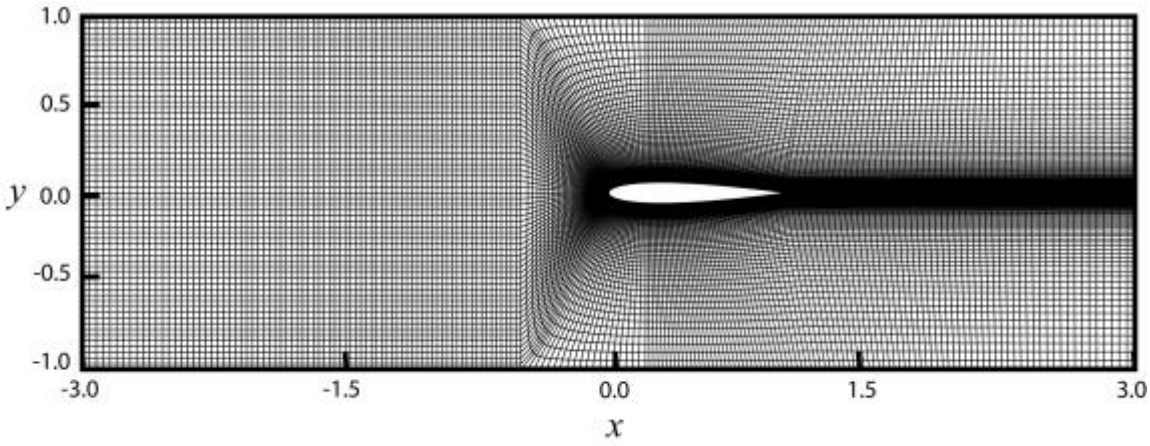

Figure 4.1: Cross-sectional view of the computational grid in the plane $z = 0$. The inlet and outlet planes are at $x = -3$ and $x = 3$, respectively, and the blade span length is equal to unity.

The simulation algorithm stores all dependent variables at the cell centers and calculates second-order accurate approximations of the diffusive and convective fluxes on the cell boundaries. The momentum and continuity equations are coupled together using the PISO algorithm (Issa, 1985). To achieve additional numerical stability, the time derivative is weighted between a second-order derivative approximation and a first-order upwind with a 90-10 ratio.

The computations were performed with a columnar vortex convected toward a fixed blade by a uniform upstream flow *U*. The Cartesian coordinate system used for these simulations was oriented such that the uniform flow was in the *x*-direction, the normal vector of the blade center plane was in the *y*-direction, and the blade span was in the *z*-direction (Figure 4.2).

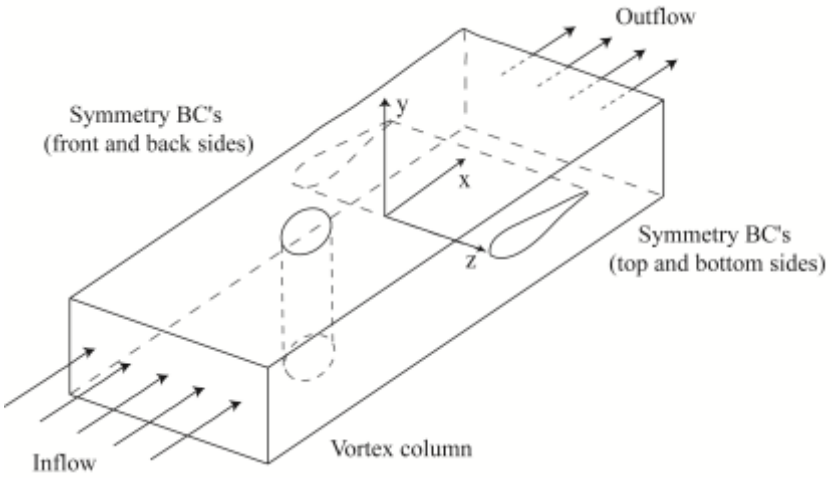

Figure 4.2: Schematic diagram showing coordinate system and boundary conditions used for the numerical computations.

Standard inflow and outflow boundary conditions were used for the boundary planes in the *x*-direction, and symmetry boundary conditions were used in the *y*- and *z*-directions. The blade was a NACA0012 airfoil with chord length *c* and with leading edge lying on the line $x = 0$. The computational domain spanned the region $-3 \le x/c \le 3$, $-1 \le y/c \le 1$, and $-1.25 \le z/c \le 1.25$, where the blade center plane is given by the intersection of the blade with the $y = 0$ plane. The initial velocity field was evaluated using a columnar Rankine vortex with uniform vorticity distribution, strength Γ, and core radius $\sigma_0 / c = 0.25$, along with two similar vortices in neighboring domains in the spanwise direction. The vortex axis was initialized on the central plane ($z_0 = 0$) at a location $x_0 / c = -1.1$ upstream of the blade leading edge, and the inlet plane was located upstream of the blade leading edge at $x_{inlet} / c = -3$.

Several dimensionless parameters can be defined which govern orthogonal vortex-blade interactions. The vortex and blade Reynolds numbers are defined as

$\mathrm{Re}_V \equiv \Gamma/\nu$ and $\mathrm{Re}_B \equiv Uc/\nu$, where ν is the kinematic viscosity. The free-stream velocity U can be used to define the *impact parameter* as $I \equiv 2\pi\sigma_0 U/\Gamma$, which is the ratio of the relative vortex-blade velocity to the maximum swirl velocity within the vortex. The thickness parameter T/σ_0, which is the ratio of the blade thickness T to the vortex core radius σ_o, is important for determining the extent and type of vortex core deformation as the vortex approaches the blade. The ambient vortex axial flow was set to zero for all cases examined in the paper. The computations reported were selected to compare cases in the high impact parameter and low thickness parameter regime. The values of these parameters for the cases considered in the paper are given in Table 4.1. The thickness parameter is fixed at $T/\sigma_0 = 0.8$ and the blade Reynolds number is set at $\mathrm{Re}_B = 1000$ for all cases examined. The impact parameter varies from 0.5 to 20. In all instances, the impact parameter is sufficiently high that no separation of the boundary layer vorticity is observed prior to impact with the vortex. The vortex Reynolds number varies inversely to the impact parameter, ranging from 79 to 3142 for the different cases examined.

Typical values of blade and vortex Reynolds numbers in vortex cutting problems depend upon the application. Taking helicopter flow as an example system, for instance, the typical blade Reynolds number Re_B is estimated by Leishman (2006) as about 5×10^6 for retreating blades and 2×10^7 for advancing blades. The typical vortex strength is estimated by Leishman as being approximately equal to the bound vortex strength on the blade surface, which for typical values of the blade solidity and thrust coefficient gives helicopter vortex Reynolds numbers Re_V of about 20% of the blade Reynolds

number. While these Reynolds number values are much higher than those used in the current computations, it was shown by Liu and Marshall (2004), and is also the case for vortex reconnection problems in general, that the value of the Reynolds number has only a minor influence on the vortex cutting flow results. For instance, Liu and Marshall (2004) obtained computational results for blade lift coefficient during chopping of a vortex with axial flow which agree well with experimental values obtained at a Reynolds number three orders of magnitude higher than the computational value.

All length variables are non-dimensionalized using the blade chord *c*, velocity variables are non-dimensionalized by the free-stream velocity *U*, time is non-dimensionalized by the advective time c/U, and vorticity is non-dimensionalized by the inverse time scale U/c. Pressure and shear stress are non-dimensionalized by ρU^2, where ρ is the fluid density. The blade surface vorticity flux, defined by

$$\mathbf{q} = -\nu \frac{\partial \boldsymbol{\omega}}{\partial n}, \tag{4.1}$$

where **n** is the outward unit normal of the blade surface and ν is the kinematic viscosity, is non-dimensionalized by $\nu U / c^2$.

Grid independence was examined by repeating the calculation in Case 2 for four different meshes, where the total number of grid points varied by a factor of 4.5 between the coarsest and finest meshes. The meshes are labeled as mesh A (865,536 grid points), mesh B (1,900,701 grid points), and mesh C (3,883,238 grid points). All computations in this comparison were performed with the same parameter values and with the same

computational domain size. Grid independence was demonstrated by computing the positive and negative circulation measures, defined by

$$\Gamma^{+} = \int_{L} \omega_y^{+}\, dx, \qquad \Gamma^{-} = \int_{L} \omega_y^{-}\, dx, \tag{4.2}$$

where $\omega_y^{+} = \begin{cases} \omega_y & \text{if } \omega_y > 0 \\ 0 & \text{if } \omega_y \le 0 \end{cases}$ and $\omega_y^{-} = \begin{cases} 0 & \text{if } \omega_y > 0 \\ -\omega_y & \text{if } \omega_y \le 0 \end{cases}$. The line L lies on the blade symmetry plane, extending over the interval $-1.3 \le x \le 0$ upstream of the blade leading edge and passing through the ambient position of the vortex axis. The results are plotted as functions of time for each mesh type in Figure 4.3. The peak negative circulation measure has about 4% difference between meshes A and B, and less than 1% difference between meshes B and C. The peak positive circulation measure has about 10% difference between meshes A and B, and less than 5% difference between meshes B and C. The negative values of ω_y lies within the vortex core and the positive values of ω_y are induced within the thin blade boundary layer at the leading edge in response to the induced velocity by the vortex, which explains why the positive circulation measure is more sensitive to grid resolution than is the negative circulation measure. All subsequent computations in the paper were performed using the grid in mesh C.

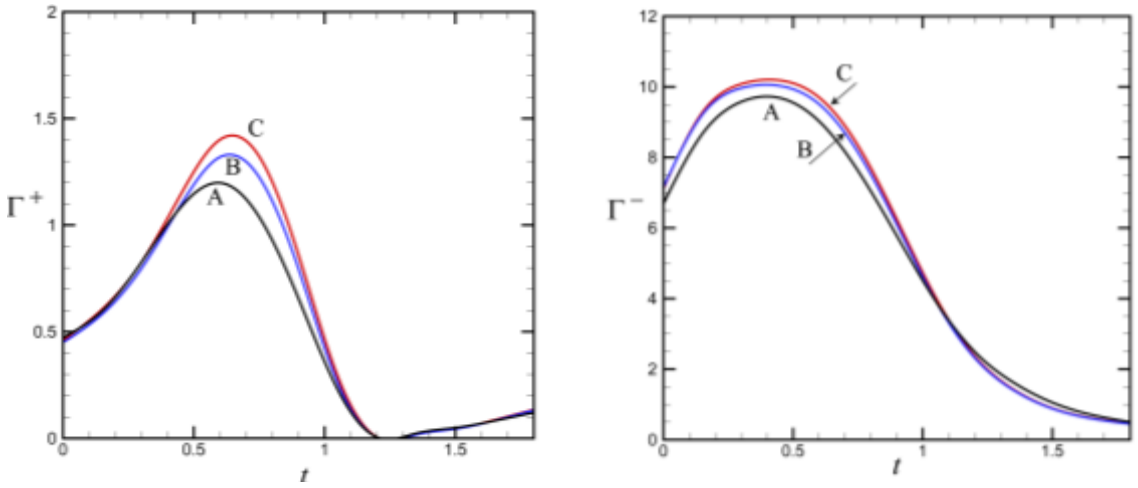

(a) (b)

Figure 4.3: Positive and negative circulation measures, Γ^+ and Γ^-, versus dimensionless time. The circulation was calculated along a line extending out from the blade front in the –*x* direction over the interval $-1.3 \le x \le 0$ for three different meshes: Mesh A – 865,536 grid points (black), Mesh B – 1,900,701 grid points (blue), and Mesh C – 3,883,238 grid points (red).

The effect of domain size was also considered to ensure the accuracy of the numerical simulations. The most important parameter was found to be the distance between the initial position of the vortex core and the inlet plane. If this distance was set too small, the induced velocity from the vortex caused weak positive *y*-vorticity to be generated on the inlet plane, which propagates towards the blade behind the vortex. When this vorticity reaches the blade leading edge it diffusively cancels with the uncut portion of the vortex core that was stretched around the blade leading edge. Several domains were examined, and the mesh in Figure 4.1 was chosen in order to ensure that the strength of this inlet vorticity was small and that it did not reach the blade until very late in the computation. In addition, the effect of time step was considered and a dimensionless time step of 0.015 was chosen to ensure a CFL number of less than unity.

4.3 Vortex Cutting Simulation Results

The ambient vorticity within the vortex is in the negative *y* direction. As the vortex approaches the blade, it induces a spanwise velocity which is associated with generation of vorticity in the positive *y* direction along the blade leading edge. It is the diffusive cross-cancellation of the *y*-oriented vorticity within the vortex with that in the boundary layer along the blade leading edge that controls the vortex cutting process, through which vortex lines within the vortex are cut and reconnect to vortex lines within the blade boundary layer. Results of numerical simulations of the vortex cutting process at different values of the impact parameter, as listed in Table 4.1, are presented in this section.

Table 4.1: Values of the dimensionless parameters for the reported computations. The blade thickness parameter $T/\sigma_0 = 0.8$ and blade Reynolds number $\mathrm{Re}_B = 1000$ for all cases examined.

Case	Re_V	$\frac{2\pi\sigma_o U}{\Gamma}$
1	3,142	0.5
2	667	2.4
3	157	10
4	79	20

4.3.1. Vorticity Dynamics during Vortex Cutting

Throughout this section detailed results are shown for Case 2, and then comparisons of selected results for computations at other values of the impact parameter are given in Section 4.2. A timeline of the basic vortex cutting process is given in Figure

4.4, in which contour plots of ω_y are shown in the *x-y* plane for three times to illustrate the position of the vortex core relative to the blade during different phases of the vortex cutting process. A close-up plot is given in Figure 4.5, showing the ω_y values within a region near the blade leading edge, where regions with high negative values of ω_y are shown in blue and regions with high positive values of ω_y are shown in red.

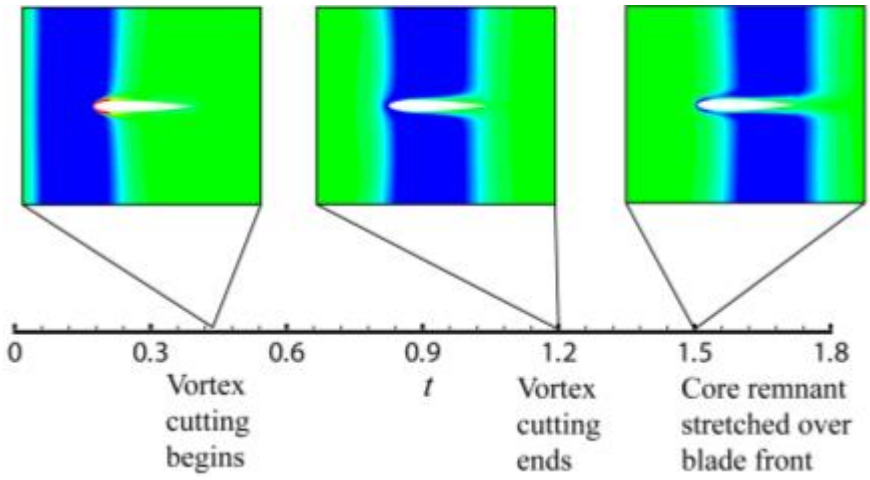

Figure 4.4: Timeline of the vortex cutting process.

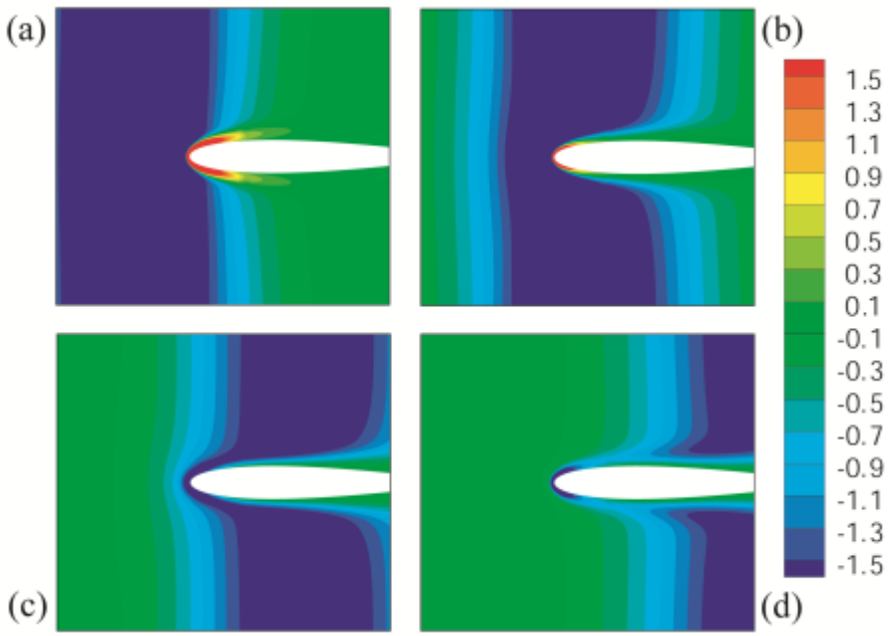

Figure 4.5: Contour plots from Case 2 showing a close-up of ω_y near the blade from a slice along the blade center span in the *x-y* plane for (a) *t* = 0.75, (b) 1.05, (c) 1.35, and (d) 1.65.

At the beginning stage of cutting, the vortex induces a region of positive ω_y within the blade leading edge boundary layer. As the vortex impacts onto the blade, the regions with positive and negative values of ω_y, within the blade boundary layer and the vortex core, respectively, interact by diffusion and partially annihilate each other. This leads to a rapid decrease in both the negative and positive circulation measures, as shown in Figure 4.3 between times of about $t = 0.5$ and 1.0, and causes the vortex lines in the vortex core to break and reconnect to those in the blade boundary layer. However, it is clear that from about the third frame of the series in Figure 4.5 onward in time, the value of ω_y within the blade boundary layer has changed from positive to negative. As demonstrated by Liu and Marshall (2004), this change in sign is associated with the fact that as the blade leading edge passes through the core, the induced spanwise velocity along the leading

edge changes direction. After the change in sign of ω_y within the blade boundary layer occurs, the *y*-component of vorticity within the core is of the same sign as that within the blade boundary layer and diffusive annihilation can no longer occur. A series of plots showing how the value of ω_y along the blade leading edge changes sign is given in Figure 4.6, for a similar time frame as in Figure 4.5 but viewed looking along the *x*-direction, directly toward the blade front region. From this figure, we see that the change in sign of ω_y first occurs at the ends of the blade span and then moves toward the blade center as time progresses.

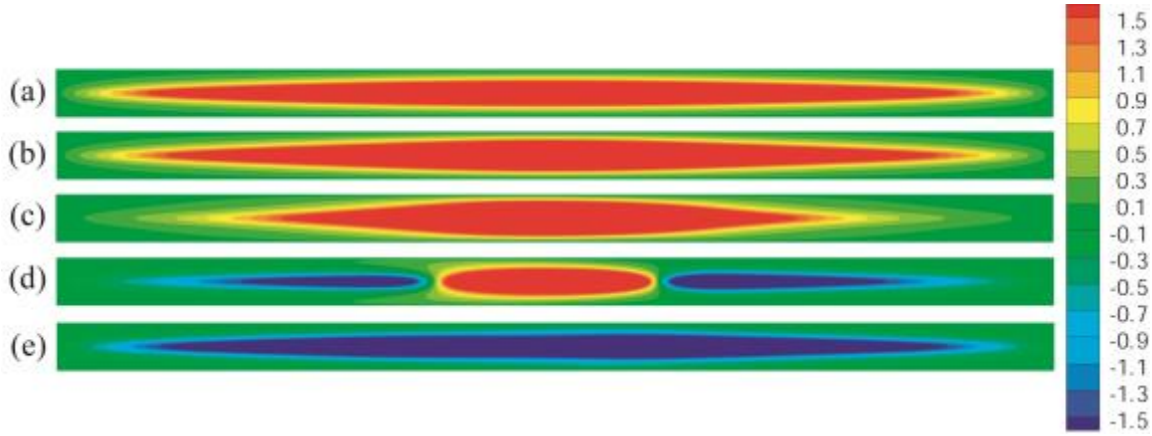

Figure 4.6: Contour plots from Case 2 of ω_y on the front of the blade for (a) *t* = 0.15, (b) 0.45, (c) 0.75, (d) 1.05, and (e) 1.35.

The *x*-component of vorticity also undergoes a sign change as the vortex core passes over the leading edge of the blade. Initially, the induced spanwise velocity from the vortex causes a region of positive ω_x to form on the blade top and a region of negative ω_x on the blade bottom. As the vortex passes over a given point on the blade surface, the induced spanwise velocity at that point changes direction, resulting in a change in the sign of ω_x. Plots illustrating this effect using a time series of contours of

ω_x are shown on the cross-sectional plane $z = 0$ (Figure 4.7) and on projections of the blade top and bottom surfaces looking along the *y*-axis (Figure 4.8). The change in sign of ω_x closely follows the path of the vortex core.

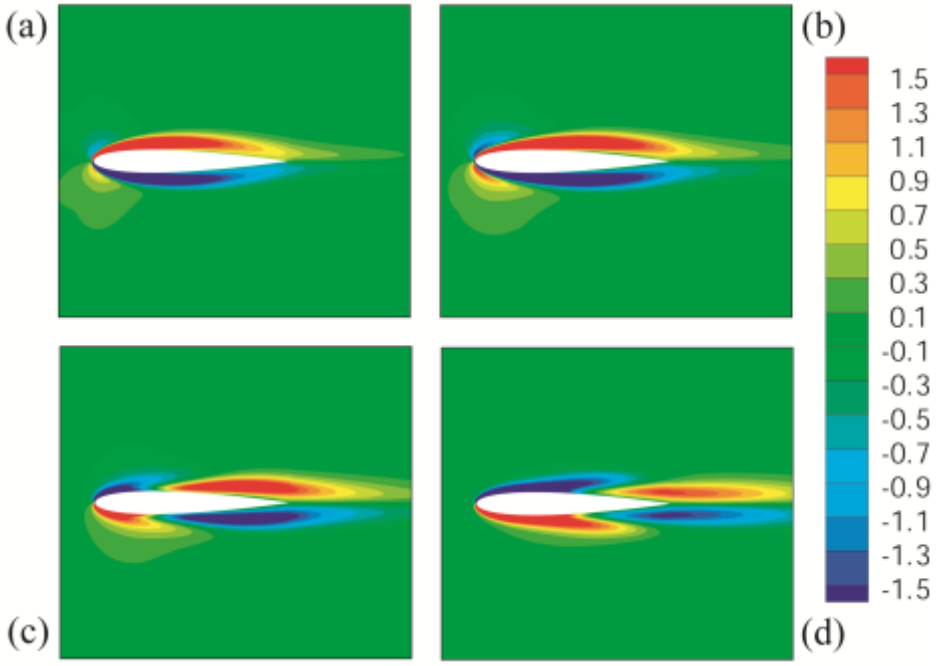

Figure 4.7: Contour plots from Case 2 of ω_x from a slice along the blade center span in the *x*-*y* plane for (a) *t* = 0.75, (b) 1.05, (c) 1.35, and (d) 1.65.

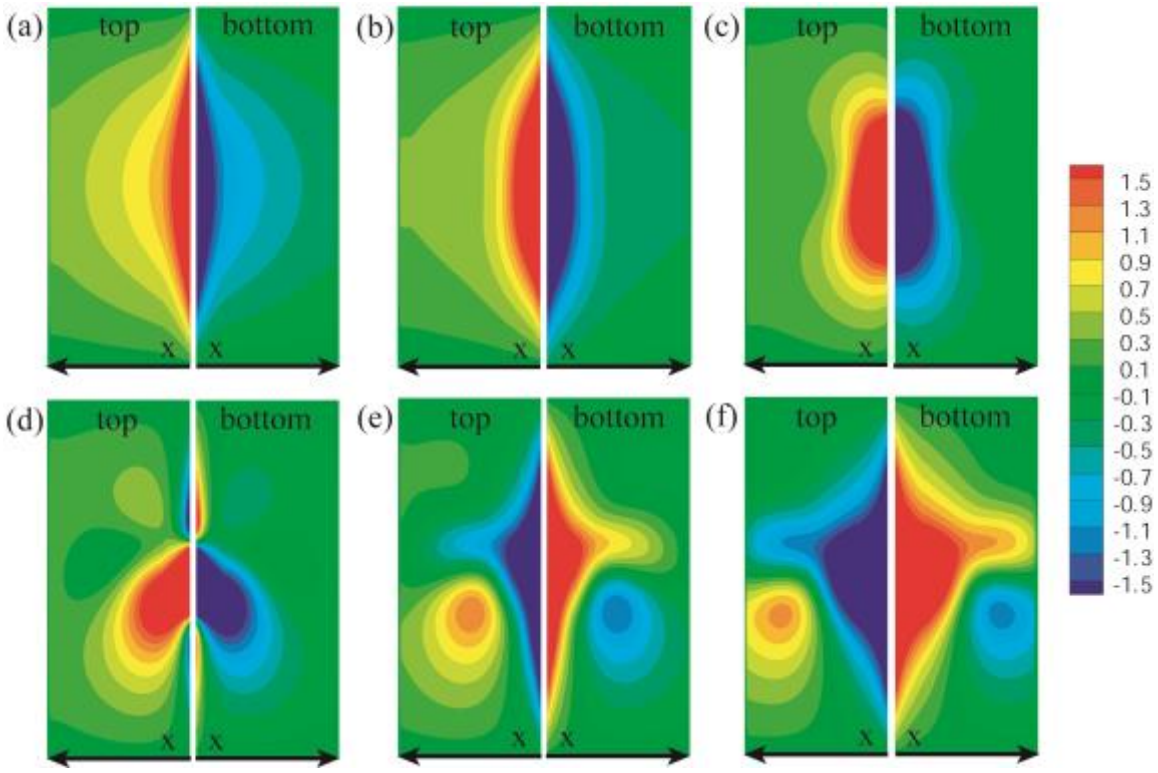

Figure 4.8: Contour plots from Case 2 of ω_x on the blade top (left) and bottom (right) at (a) *t* = 0.15, (b) 0.45, (c) 0.75, (d) 1.05, (e) 1.35, and (f) 1.65.

The essence of vortex reconnection involves cutting of vortex lines originating from one vorticity region and reconnection to vortex lines originating from another vorticity region via diffusion-regulated annihilation of vorticity between the two regions. This vortex line reconnection process for the vortex cutting problem is illustrated in Figure 4.9 for three times as the blade penetrates into the vortex core. In order to illustrate the vortex reconnection process, we color the vortex lines green to indicate vortex lines that originate within the vortex and remain within the vortex, black to indicate vortex lines that originate within the blade boundary layer and remain within the boundary layer, and red to indicate vortex lines that originate within the vortex and cross over to join those within the blade boundary layer (or vice versa).

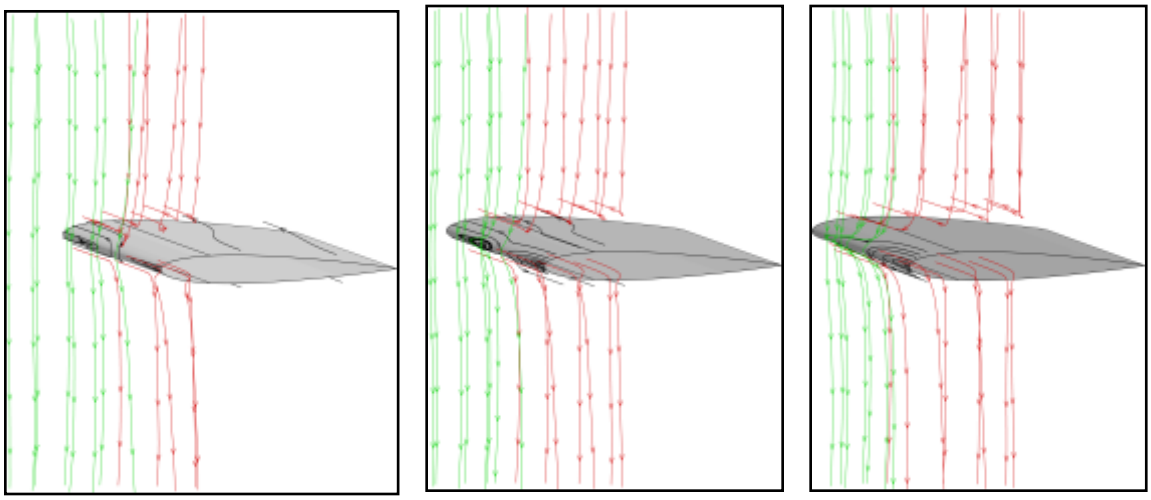

(a) (b) (c)

Figure 4.9: Oblique view of the vortex cutting process. Vortex lines originating in the vortex core can either remain within the vortex core (green) or be cut and reconnect to vortex lines in the boundary layer (red). Similarly, vortex lines originating within the blade boundary layer can either stay in the boundary layer (black) or join to those originating within the core (red). Images are shown at times (a) t = 0.9, (b) 1.05, and (c) 1.2. The green vortex lines near the leading edge become deflected in the spanwise direction as they near the blade.

At the first time (Figure 4.9a), the blade leading edge has penetrated about 30% of the way through the vortex core. At this stage, the sign of ω_y is positive at the blade leading edge and vorticity annihilation between the boundary layer and the vortex allows the vortex lines within the core to cut and reconnect to those within the boundary layer. At the second time (Figure 4.9b), the vortex core center has just passed the position of the blade leading edge and the value of ω_y at the leading edge is in the process of changing sign. Vortex lines from the vortex (in green) are now beginning to deform and to be stretched in the spanwise direction instead of being cut. This process continues in Figure 10c, where the green vortex lines are clearly deforming and stretching in the z-direction (spanwise) rather than being cut. Also, the pattern change of the black vortex lines

illustrates how the vorticity orientation in the boundary layer along the front section of the blade changes as the vortex core passes over the blade leading edge.

The pressure change along the vortex core caused by the presence of the blade is another important aspect of the vortex cutting process. For reconnection of two anti-parallel vortex tubes, Saffman (1990) proposed that the localized increase in vortex core pressure creates a positive feedback loop to drive the vortex reconnection process. We examined how the pressure in the vortex core changed for vortex cutting in order to understand if pressure plays a similar role in the vortex cutting problem. Figure 4.10 illustrates the pressure in the vortex core for a contour plot in the $z = 0$ plane, passing through the center span of the blade.

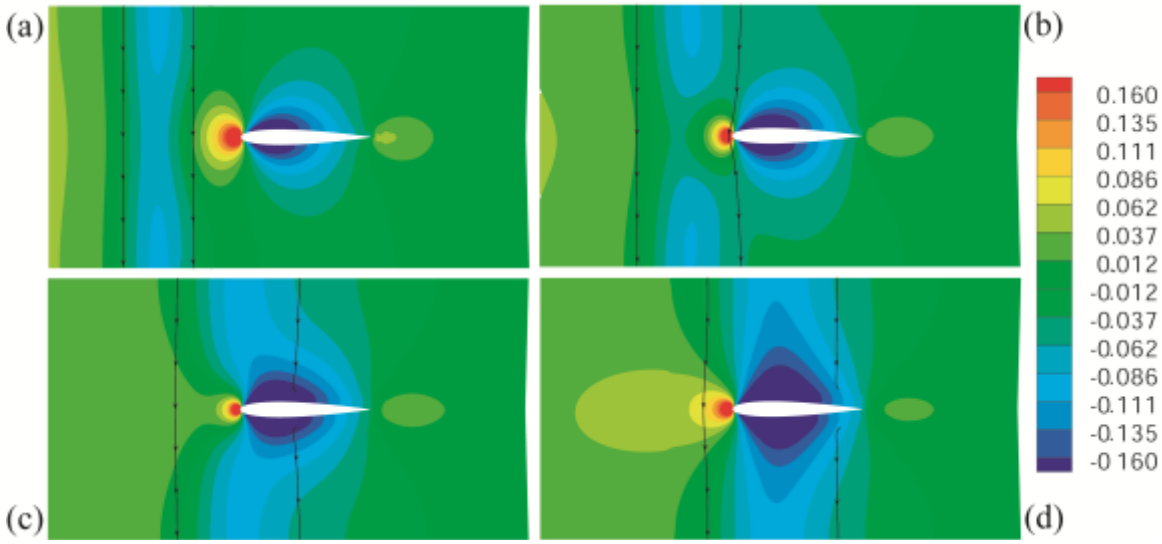

Figure 4.10: Pressure contours in the *x-y* plane passing through the center span of the blade for (a) *t* = 0.3, (b) 0.6, (c) 0.9, and (d) 1.2. The outlines of the vortex are shown by plotting vortex lines on the two sides of the vortex.

Initially there is a large region of low pressure in the vortex core as well as on the top and bottom surfaces of the blade and a region of high pressure around the blade leading edge. As the vortex moves closer to the blade, the pressure in the vortex core increases close to

the impingement region and a pressure gradient forms. This phenomenon is similar to the one Saffman (1990) described, but it occurs for a different reason. In the case of vortex cutting by a blade, the impingement of the vortex upon the ambient high pressure near the blade leading edge no doubt plays a significant role in driving the localized pressure gradient along the vortex core, and any role that core deformation might play in this process is obscured. As the vortex passes over the blade, the low pressure region in the vortex core connects with the low pressure regions on the top and bottom surfaces of the blade, as shown in Figures 4.10c and d.

The key difference between vortex cutting by a blade and more traditional vortex reconnection is the fact that vorticity is generated on the blade surface, which lies within the region dominated by vorticity diffusive interaction. The *x* and *y* components of the surface vortex flux, q_x and q_y, are shown within a projection the front region of the blade (looking along the *x*-axis) in Figures 4.11 and 4.12.

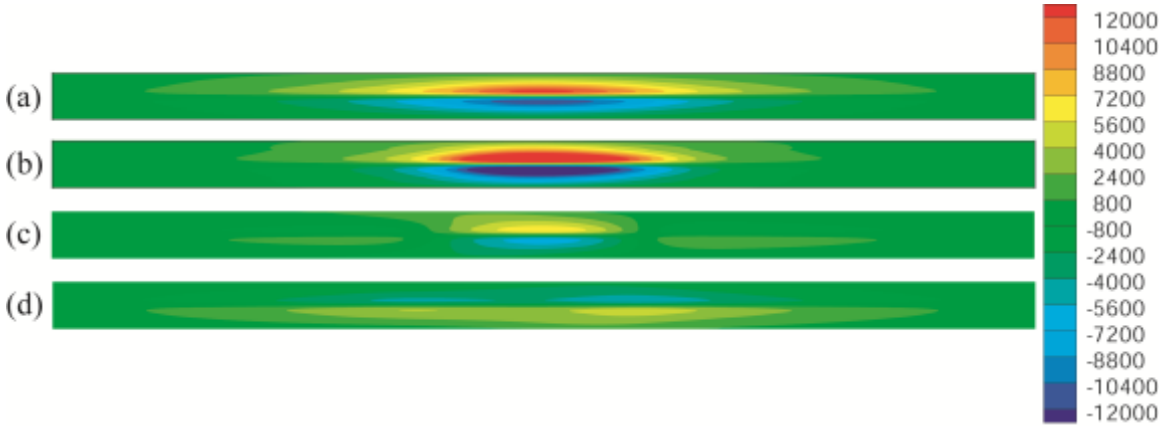

Figure 4.11: Contour plots of the *x* component of the vorticity flux, q_x, on blade leading edge, at times (a) *t* = 0.45, (b) 0.75, (c) 1.05, and (d) 1.35.

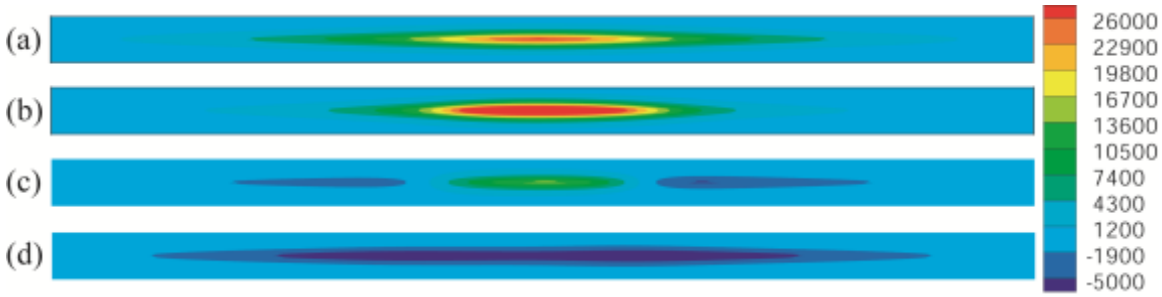

Figure 4.12: Contour plots of the *y* component of the vorticity flux, q_y, on the blade leading edge, at times (a) *t* = 0.45, (b) 0.75, (c) 1.05, and (d) 1.35.

The vorticity flux contour plots exhibit a change in sign around t = 1.05, which corresponds with the change in sign of ω_x and ω_y during vortex passage previously discussed in this section. The contour plots show that the vorticity flux is primarily generated within the leading edge region of the blade, and not on the blade top and bottom surfaces away from the leading edge. This region is exactly where the breaking and rejoining of vortex lines occurs, and further demonstrates the importance of considering the role of surface vorticity flux in a blade-vortex cutting problem.

4.3.2. Effect of Impact Parameter

Time variation of the maximum and minimum values of vorticity and surface vorticity flux are plotted for all four cases examined in Figures 4.13 and 4.14 in order to better understand the effect of impact parameter on the temporal changes in these quantities throughout the vortex cutting process and the manner in which the vortex cutting process changes with respect to the impact parameter. In interpreting these plots, it is helpful to keep in mind the time intervals for major transitions in the cutting process, namely, the onset of penetration of the blade leading edge into the vortex core ($t \cong 0.45$), the passage of the blade leading edge out of the opposite side of the vortex position (

$t \cong 1.2$), and stretching of vortex remnants over the blade leading edge ($t > 1.2$). These three time intervals correspond approximately to the three phases of traditional vortex tube reconnection as described in Section 2.2.

Figure 4.13 shows the time variation of the maximum values of ω_x and ω_z, normalized with respect to the vortex Reynolds number Re_V.

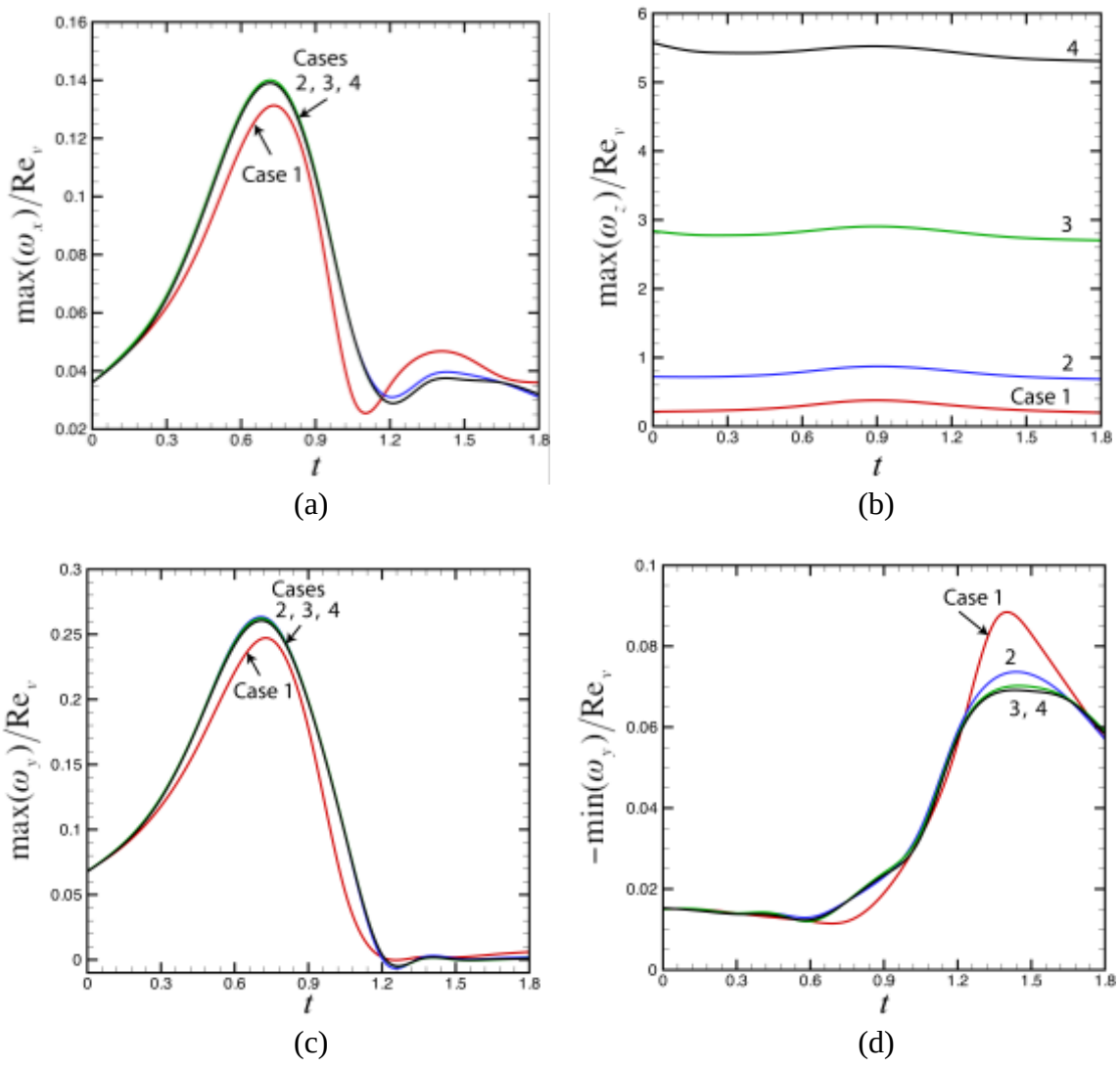

Figure 4.13: Time variation of (a) maximum ω_x, (b) maximum ω_z, (c) maximum ω_y, and (d) minimum ω_y, normalized with respect to the vortex Reynolds number $\mathrm{Re}_V = \Gamma/\nu$. Results are shown for Cases 1 (red), 2 (blue), 3 (green), and 4 (black).

The minimum values of these vorticity components follow nearly identical profiles as the maximum values due to the symmetry on the top and bottom surfaces of the blade, and so are not plotted. The different cases considered differ from each other by the value of the vortex strength, leading to different values of the vortex Reynolds number and vortex-blade impact parameter. However, the plots of maximum and minimum normalized ω_x

values for these different cases appear to nearly collapse onto a single curve, although with a slight deviation for Case 1. The plot in Figure 4.13a exhibits an increase in ω_x with time until around t = 0.75, which corresponds to the time at which the vortex core axis passes over the blade leading edge. Following this time, the value of ω_x gradually decreases until it approaches its initial value as the vortex moves past the tail end of the blade. The maximum value of ω_x occurs in the center of the blade, slightly above the blade centerplane but within the blade boundary layer. From Figure 4.13a, we conclude that the maximum value of ω_x is dominated by the initial cutting of the vortex, and that this value increases approximately linearly with the vortex strength.

The maximum value of ω_z / Re_V, shown in Figure 4.13b, clearly does not collapse onto a single curve for the different cases examined. The results for the different cases appear to be qualitatively similar, but the maximum value of ω_z / Re_V increases/decreases as the vortex Reynolds number increases/decreases. The maximum in ω_z also occurs at a somewhat later time than does the maximum in ω_x, although it seems to occur at the same time for all of the cases examined. In contrast to the maximum of ω_x, the maximum value of ω_z occurs to the left of the center of the blade span and slightly below the blade center plane. This shift is likely due to the induced velocity of the vortex creating a slightly higher free-stream velocity on the left side of the blade and slightly lower velocity on the right side, looking downwind toward the blade leading edge.

The maximum and minimum values of ω_y, normalized by the vortex Reynolds number, are plotted in Figures 4.13c and 4.13d for the four cases listed in Table 4.1, each

with different value of the impact parameter. We again see that the curves nearly coincide for the different cases examined, with the exception of a slight deviation for Case 1. This data collapse indicates that the value of ω_y varies approximately linearly with vortex strength. The maximum positive value of ω_y (which occurs within the boundary layer at the blade leading edge) initially increases as the blade penetrates into the vortex core until a time of about t = 0.75, and after which it decreases to a value of nearly zero as the vortex core passes over the leading edge of the blade and the positive vorticity on the blade front induced by the vortex changes sign. The maximum negative value of ω_y, which initially occurs within the vortex core, exhibits a gradual decay with time during the initial part of the computation, which is due to viscous diffusion of the vortex core. The maximum negative value of ω_y is not significantly affected by the vortex cutting process until the vortex core moves past the blade leading edge and the value of ω_y within the blade boundary layer changes from a positive to a negative sign. From this time until the end of the computation, the point of maximum negative value of ω_y is located at the blade leading edge. The maximum negative value of ω_y gradually increases from the time (t = 0.75) of change in sign of ω_y within the blade boundary layer to a time at which the blade leading edge has entirely penetrated through the vortex core (about $t = 1.5$), after which the maximum negative value of ω_y remains approximately constant for the remainder of the computation. Both the generation of negative ω_y due to induced spanwise velocity from the vortex and the increase in vorticity due to stretching of the remaining portions of the vortex wrapped about the

blade leading edge contribute to producing the maximum negative ω_y value. The fact that the peak value of the maximum negative value of ω_y occurs quite late, when the vortex core is well past the center of the blade, suggests the presence of significant uncut vorticity remnants from the impinging vortex. These uncut vorticity remnants wrap around the blade surface in the form of a thin vortex sheet, for which the value of the negative vorticity component ω_y continuously intensifies by stretching about the blade leading edge while at the same time it is regulated by viscous diffusion, eventually approaching a constant value in a manner analogous to the classical Burgers vortex (Burgers, 1948).

The time variation in positive and negative components of the surface vorticity flux is shown in Figure 4.14.

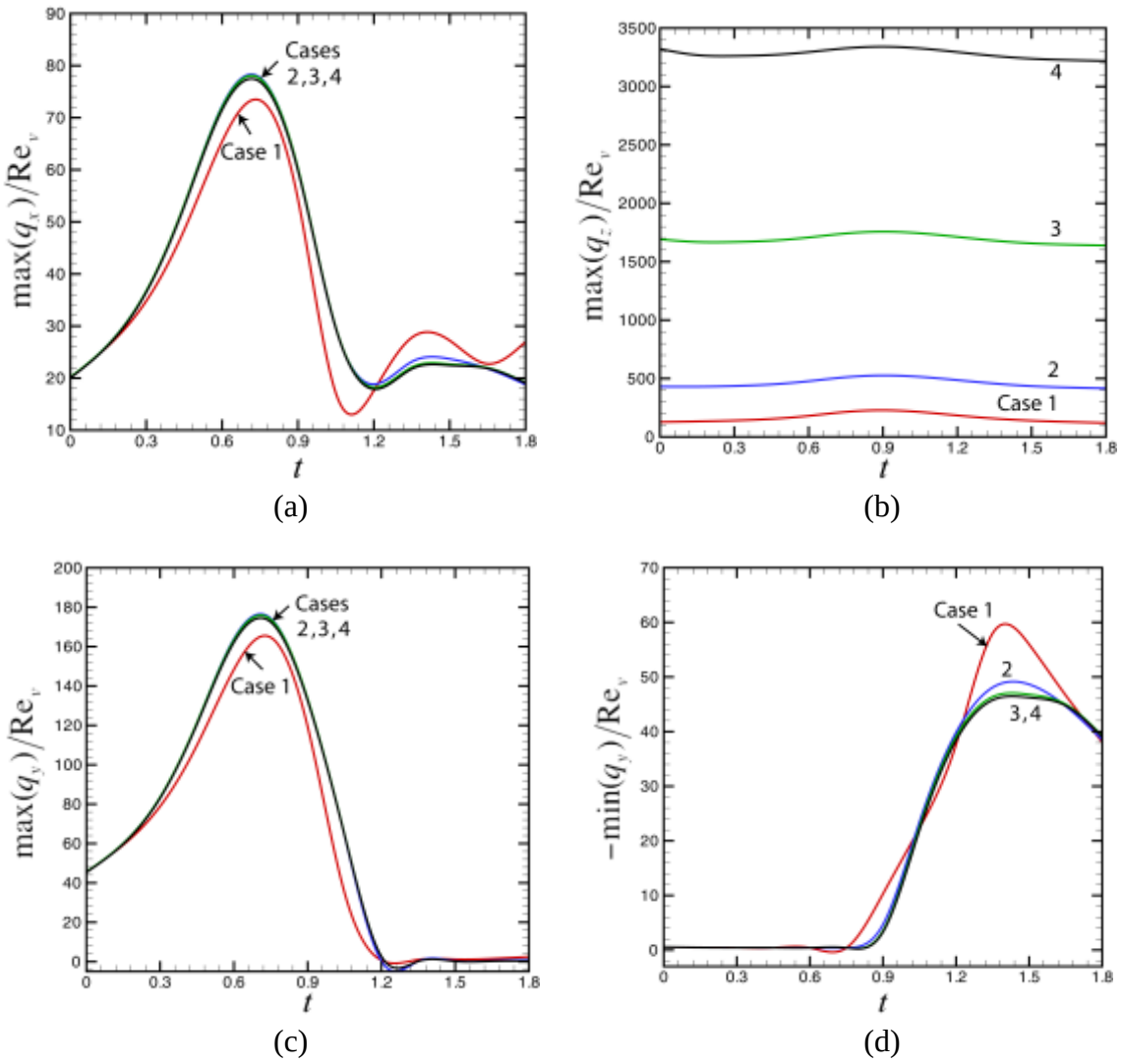

Figure 4.14: Time variation of the maximum values of the surface vorticity flux components (a) q_x, (b) q_z, and (c) q_y, and minimum values (d) q_y, normalized with respect to the vortex Reynolds number. Results are shown for Cases 1 (red), 2 (blue), 3 (green), and 4 (black).

The *x*- and *z*-vorticity fluxes, q_x and q_z, exhibit a functional form very similar to the corresponding maximum values of the vorticity components ω_x and ω_z. As was the case for the vorticity, the maximum positive and negative values of the vorticity flux in these directions follow the same curve, and the maximum values of q_x for the different cases examined collapse nearly onto a single curve while those for q_z do not. It can again be

seen that both an initial increase in the positive vorticity flux component q_y which then drops off to 0 as the cutting process stops, and a late increase in the negative component of vorticity flux as negative *y*-vorticity is generated on the blade leading edge.

This section concludes by revisiting the discussion in Section 2.2 of the different physical processes that occur during vortex reconnection, and comparing these processes to those occurring during vortex cutting. Three distinct phases of vortex reconnection were identified. The first phase is dominated by inviscid interaction of the vortices and has two parts - anti-parallelization and core deformation. The vortex cutting process appears at first view to be most similar to the orthogonally-offset vortex reconnection problem, of the type examined by Boratav et al. (1992) and Zabusky and Melander (1989), since the ambient blade boundary layer vorticity is in the *z*-direction and the ambient vorticity within the vortex is in the *y*-direction. However, unlike in the orthogonal vortex tube reconnection problem, the impinging vortex does not twist around to orient itself anti-parallel to the ambient boundary layer vorticity as it approaches the blade. Instead, the induced velocity from the vortex generates new vorticity in the anti-parallel direction to the incident vortex on the blade leading edge as the vortex approaches. Instead of an inviscid vortex twisting process, in the vortex cutting case the anti-parallel configuration is achieved via viscous vorticity generation on the blade surface. The extent of inviscid core deformation in the vortex cutting process depends greatly on the value of the thickness parameter, T/σ_0. For sufficiently large values of this parameter, significant core deformation can occur as the impinging vortex interacts inviscidly with its image over the blade surface.

The second phase of vortex reconnection entails viscous annihilation of anti-parallel vorticity between the two vorticity regions, leading to vortex line cutting and reconnection between the regions. This process occurs much the same in the vortex tube reconnection and vortex cutting problems, with the difference that in classical vortex tube reconnection all of the vorticity is present at the start of the computation, whereas for vortex cutting vorticity is continually being generated at the blade surface during the reconnection process.

Both the classical vortex tube reconnection and the vortex cutting processes are incomplete, leading to the formation of uncut remnants, or threads, in the third phase of reconnection. Despite this similarity, the reasons that the vortex tube reconnection and the vortex cutting are incomplete are quite different. For vortex tube reconnection, the incomplete reconnection occurs due to the velocity induced by the highly curved bridge regions connecting the two vortex tubes. As these bridges grow in strength, the self-induced velocity gets larger and it is eventually sufficient to move the cores away from one another before all opposite-sign vorticity in the reconnection region has been annihilated. For the vortex cutting process, the incomplete cutting occurs due to the change in sign of the vorticity flux in the anti-parallel (y) direction on the blade leading edge as the leading edge penetrates sufficiently far into the vortex core. Regardless of the different mechanism leading to incomplete reconnection, the end result for both processes is the formation of uncut vorticity threads that linger for long time periods after the primary reconnection or cutting process is complete.

4.4 Model for Vortex Sheet in a Straining Flow near a Surface

A key component of the vortex cutting process involves diffusive vorticity annihilation between the incident vortex and vorticity generated on the blade boundary layer. The incident vorticity initially has the form of a tube, but as it wraps about the blade leading edge it deforms into more of a sheet-like structure (Marshall and Grant, 1996). Finally, the stretching of the impinging vortex imposed by the ambient flow about the blade leading edge plays a critical role in determining the vorticity evolution within the cutting region. In this section a new exact Navier-Stokes solution is described that contains these three elements – anti-parallel vorticity diffusive annihilation, vorticity generation on a surface, and vortex stretching. While the model to be presented incorporates these three key elements, to make the problem analytically tractable, certain other elements of the vortex cutting problem must be dramatically modified. In particular, the model does not deal with vorticity bending around the highly curved blade leading edge, but instead considers vorticity above a flat surface that is stretched by an imposed viscous straining flow (Hiemenz, 1911), as indicated in the schematic diagram in Figure 4.15.

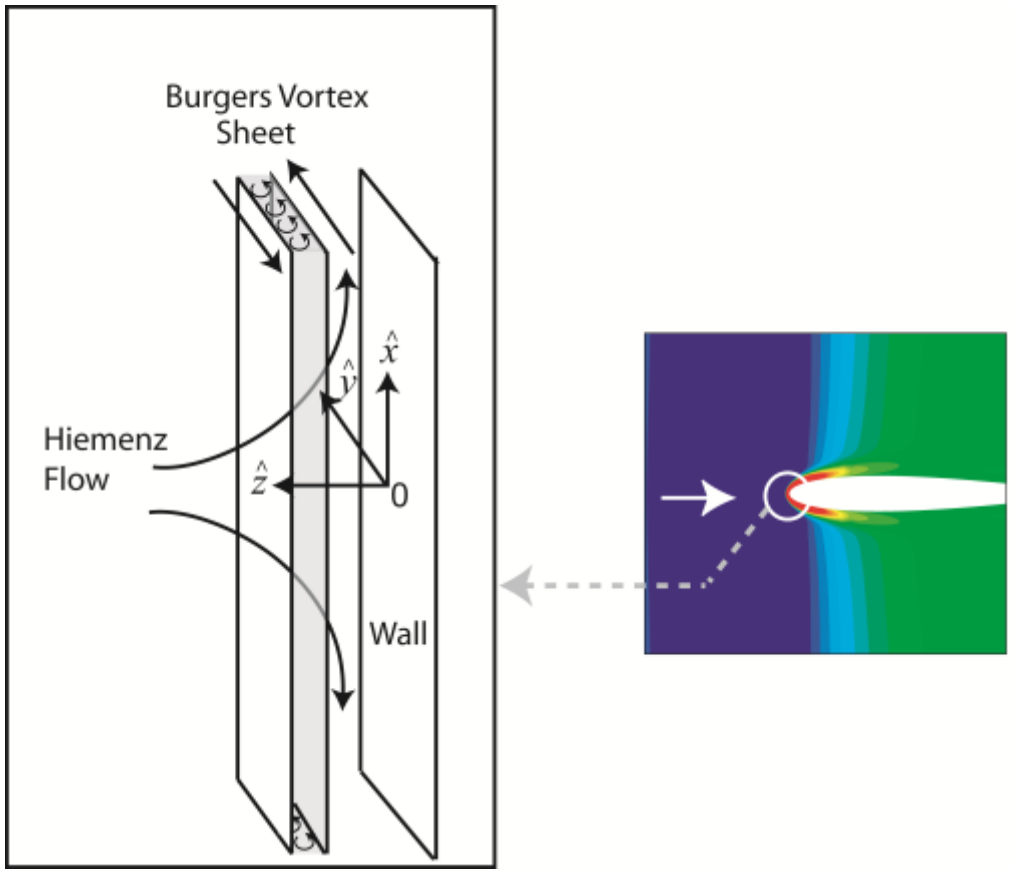

Figure 4.15: (LEFT) Schematic diagram of the model flow field, consisting of a Burgers' vortex sheet (shaded) immersed in a Hiemenz straining flow. (RIGHT) Illustration of vertical vorticity contours during vortex-blade interaction, showing the relationship between the model flow and vorticity dynamics occurring at the blade leading edge during the vortex cutting process.

Secondly, the vortex sheet is assumed to be infinitely wide, whereas the incident vortex in the vortex cutting problem has a finite width. Were it not for the presence of the solid surface, this stretched vortex sheet would be identical to a Burgers sheet, where the vorticity within the sheet is oriented along the direction of the straining flow (Burgers, 1948; Gibbon et al., 1999). Because of these various simplifications incorporated into the model, we do not expect the model solutions to provide an accurate quantitative approximation of the vorticity field in the problem of vortex cutting by a blade.

Nevertheless, the model contains many of the key ingredients of the vortex cutting problem and it may be helpful in suggesting physically-motivated scaling for the vortex cutting problem. As an exact Navier-Stokes solution, the model is also of interest in its own right.

The model deals with a combination of a Hiemenz straining flow and a vortex sheet over a flat surface. The model problem is solved using the Cartesian coordinate system ($\hat{x},\hat{y},\hat{z}$) shown in Figure 4.15, in which $\hat{z}$ points in the upstream direction, $\hat{x}$ is oriented in the direction of the Heimenz straining flow close to the wall, and $\hat{y}$ is in the direction of the flow induced by the vortex sheet. Figure 4.15 illustrates the fact that this model is not intended to be representative of the entire vortex-blade interaction problem, but only of the flow very close to the point of vortex impingement on the blade leading edge. The velocity and pressure fields are assumed to satisfy

$$\mathbf{u} = \hat{u}(\hat{x},\hat{z})\mathbf{e}_{\hat{x}} + \hat{v}(\hat{z},t)\mathbf{e}_{\hat{y}} + \hat{w}(\hat{z})\mathbf{e}_{\hat{z}}, \qquad p = p_1(\hat{x}) + p_2(\hat{z}). \tag{4.3}$$

Under these conditions the continuity and Navier-Stokes equations reduce to

$$\frac{\partial \hat{u}}{\partial \hat{x}} + \frac{\partial \hat{w}}{\partial \hat{z}} = 0, \tag{4.4a}$$

$$\hat{u}\frac{\partial \hat{u}}{\partial \hat{x}} + \hat{w}\frac{\partial \hat{u}}{\partial \hat{z}} = -\frac{1}{\rho}\frac{\partial p_1}{\partial \hat{x}} + \nu\left(\frac{\partial^2 \hat{u}}{\partial \hat{x}^2} + \frac{\partial^2 \hat{u}}{\partial \hat{z}^2}\right), \tag{4.4b}$$

$$\frac{\partial \hat{v}}{\partial t} + \hat{w}\frac{\partial \hat{v}}{\partial \hat{z}} = \nu\,\frac{\partial^2 \hat{v}}{\partial \hat{z}^2}, \tag{4.4c}$$

$$\hat{w}\frac{\partial \hat{w}}{\partial \hat{z}} = -\frac{1}{\rho}\frac{\partial p_2}{\partial \hat{z}} + \nu \frac{\partial^2 \hat{w}}{\partial \hat{z}^2}. \tag{4.4d}$$

We denote the straining rate of the external Hiemenz flow by *s*, the strength of the Burgers vortex sheet by γ, a scaled height variable by $\eta = \hat{z}\sqrt{s/\nu}$, and a scaled time by $\tau = st$. The velocity components can be written as

$$\hat{u} = s\hat{x}F'(\eta), \qquad \hat{v} = \gamma G(\eta, \tau), \qquad \hat{w} = -F(\eta)\sqrt{s\nu}. \tag{4.5}$$

These expressions for velocity satisfy the continuity equation (4.4a) identically, and the momentum equations (4.4b) and (4.4d) reduce to an ordinary differential equation for $F(\eta)$ as

$$F''' + FF'' - (F')^2 + 1 = 0, \tag{4.6}$$

subject to the boundary conditions $F(0) = F'(0) = 0$ and $F'(\infty) = 1$. Substituting (4.5) into (4.4c) yields a partial differential equation for $G(\eta, \tau)$ as

$$\frac{\partial G}{\partial \tau} - F(\eta)\frac{\partial G}{\partial \eta} = \frac{\partial^2 G}{\partial \eta^2}. \tag{4.7}$$

Equation (4.7) is subject to the boundary conditions

$$G(0,\tau)=0, \quad G(\infty,\tau)=\alpha\,, \tag{4.8}$$

where α is a prescribed parameter representing the ratio of the velocity far away from the plate to the vortex sheet strength.

Equation (4.6) is the equivalent to the classic Hiemenz problem, which was solved using a fourth-order Runge-Kutta method, yielding $F''(0)=1.23259$. Equation (4.7) was solved using the Crank-Nicholson method with $\Delta\eta=0.005$ and $\Delta\tau=0.001$. The primary dimensionless parameter is the ratio α of velocity $\hat{v}_\infty$ in the $\hat{y}$-direction far away from the surface to the initial vortex sheet strength γ. Other parameters include the initial position η_0 of the vortex sheet and the initial thickness Δ of the Stokes first problem boundary layer on the wall. A simple example calculation is considered using this model for the problem of a vortex sheet being driven into a flat wall by a Hiemenz straining flow. The initial condition for this example problem has the form of an equilibrium Burgers vortex sheet centered at η_0 and a Stokes first problem boundary layer with dimensionless thickness Δ, given by

$$G(\eta,0)=G_0(\eta)=(1+\alpha)\text{erf}\,(\eta/2\Delta)-\frac{1}{2}-\frac{1}{2}\text{erf}\,[(\eta-\eta_0)/\sqrt{2}], \tag{4.9}$$

where erf(·) is the error function. In this example problem $\eta_0=10$ and $\Delta=1$. Results for this flow are shown in Figure 4.16 for the dimensionless velocity $G=\hat{v}/\gamma$ and dimensionless vorticity $\zeta\equiv\partial G/\partial\eta$ as functions of dimensionless time τ. Based on the

coordinate system shown in Figure 4.15, the velocity is in the $\hat{y}$-direction and the vorticity is in the $\hat{x}$-direction.

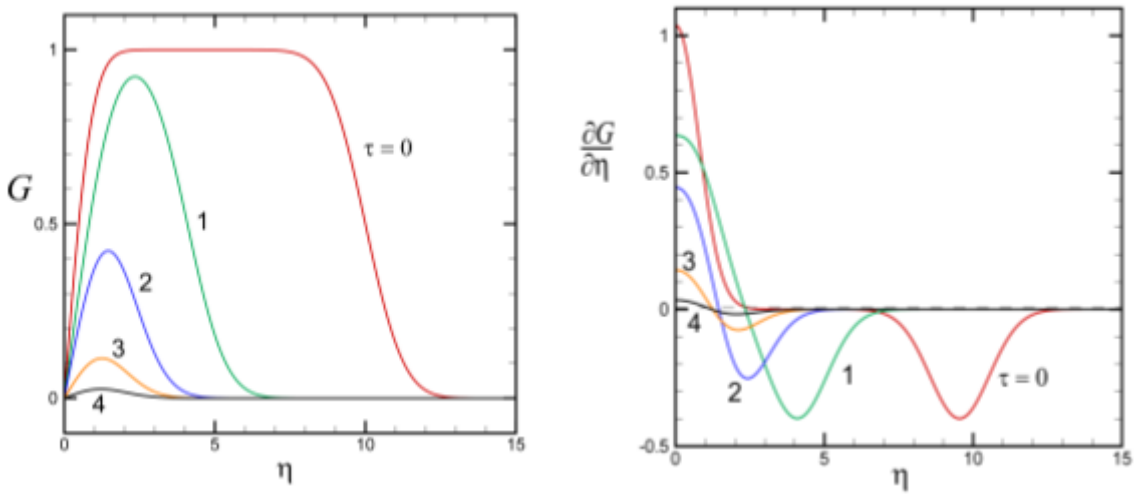

(a) (b)

Figure 4.16: Variation of (a) dimensionless velocity *G* and (b) dimensionless vorticity $\partial G/\partial \eta$ as functions of η for a case with $\alpha = 0$. Plots are shown for $\tau = 0$ (A, red), 1 (B, green), 2 (C, blue), 3 (D, orange), and 4 (E, black).

Dimensionless circulation measures Γ^+ and Γ^- are defined by

$$\Gamma^+ = \int_L \zeta^+ \, d\eta \,, \qquad \Gamma^- = \int_L \zeta^- \, d\eta \,, \tag{4.10}$$

where $\zeta^+ = \begin{cases} \zeta & \text{if } \zeta > 0 \\ 0 & \text{if } \zeta \le 0 \end{cases}$ and $\zeta^- = \begin{cases} 0 & \text{if } \zeta > 0 \\ -\zeta & \text{if } \zeta \le 0 \end{cases}$, and L denotes the range $(0, \eta_{\max})$ of η. Plots of time variation of Γ^+ and Γ^-, given for the example problem in Figure 4.17, provide a quantitative measure of the extent of vorticity diffusion-driven annihilation occurring between the incident vortex sheet and the boundary layer vorticity.

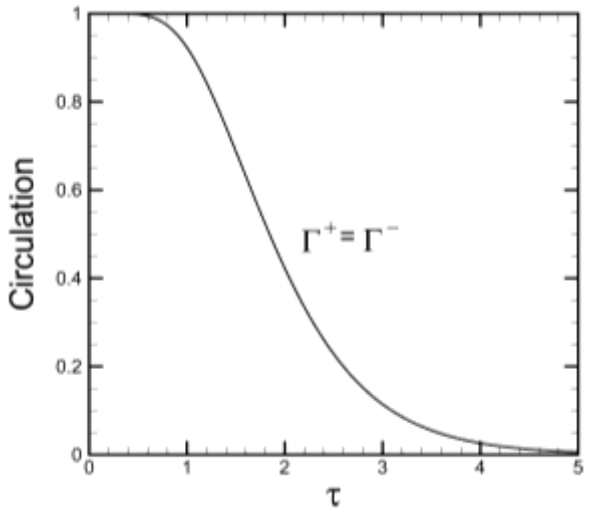

Figure 4.17: Time variation of dimensionless circulation measures Γ^+ and Γ^- as functions of τ for the example problem shown in Figure 4.16. For the case with $\alpha = 0$, $\Gamma^+ = \Gamma^-$.

In the numerical simulation of vortex cutting by a blade discussed in Section 4.3, the assumption that the ambient flow past the blade has the form of a plane straining flow would only be relevant in a region close to the blade leading edge. While we do not expect this simple model to provide an accurate quantitative description of the full numerical simulation, it is nevertheless of interest to compare the model results with those of the full numerical simulation within this near-blade region. In comparing these result, we note the relationships $(\hat{x}, \hat{y}, \hat{z}) = (y, -z, -x)$ and $(\hat{u}, \hat{v}, \hat{w}) = (v, -w, -u)$ between coordinate and velocity components in the model problem and the numerical simulation. The value of the spanwise velocity component *w* was extracted from the numerical simulations along a line corresponding with the -*x* axis from $x = 0$ to $x = -15\sqrt{s/\nu}$, corresponding to the interval $0 \le \eta \le 15$. The straining rate *s* was obtained by extracting the velocity component *v* in the *y*-direction along this same line and fitting a tangent line

near $\eta = 0$, which for Case 2 yields s = 26.7. The negative spanwise velocity $(-w)$ extracted along this line is comparable to the velocity component $\hat{v}$ in the simple theoretical model, and it is plotted as a function of η in Figure 4.18a for different values of the scaled time variable $\tau = st$.

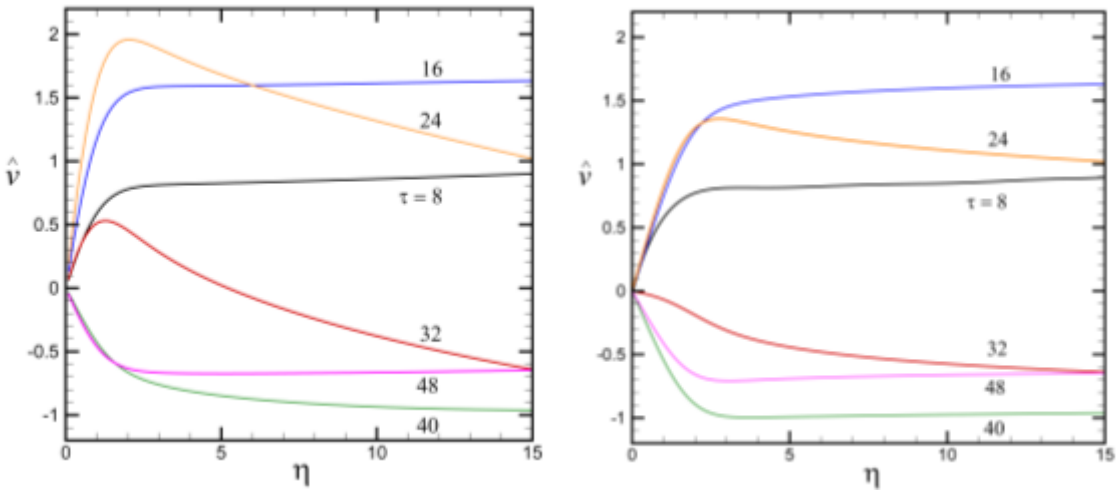

Figure 4.18: Comparison of profiles of dimensionless velocity $\hat{v}$ as a function of η at $\tau = 8$ (black), 16 (blue), 24 (orange), 32 (red), 40 (green), and 48 (purple). Plots are shown for (a) the vortex cutting simulation described in Section 4.3 and (b) the simple model described in Section 4.4.

Comparison results for the theoretical model were obtained using the same initial velocity profile as shown in Figure 4.17a for the vortex cutting simulation, and by varying the boundary condition α in (4.8) as a function of time in accordance with the values of $\hat{v}$ at the position $\eta = 15$ along the extraction line obtained from the vortex cutting simulation. The model calculation was initialized at $\tau = 8$ in order to give the vortex time to approach the blade surface. The results from the model calculations are plotted in Figure 4.18b for the velocity profile. The two sets of results do not exactly match up, but they have sufficiently good qualitative similarities to suggest that the

temporal and spatial scaling suggested by the model are valid also with more general vortex cutting problem. To quantify the vorticity annihilation in the vortex cutting simulations and the simple model, we plot in Figure 4.19 the time variation of the positive and negative circulation measures Γ^+ and Γ^-, which are computed in this case using integration over the interval $0 \le \eta \le 15$, corresponding to the interval -0.09 ≤ x ≤ 0 in the numerical simulations of vortex cutting by a blade.

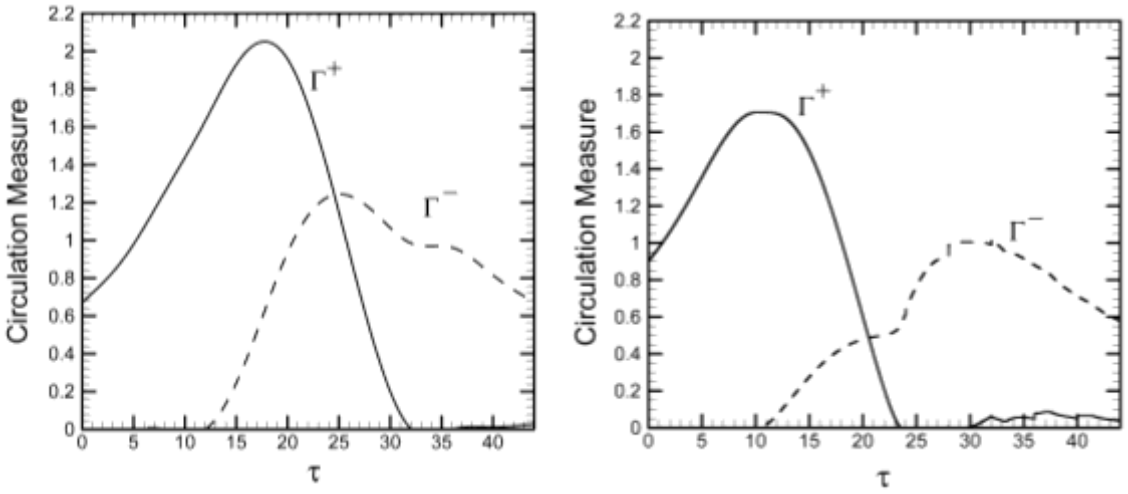

Figure 4.19: Time variation of the dimensionless circulation measures Γ^+ and Γ^- as functions of τ for the vortex cutting problem shown in Figure 4.18. Plots are shown for (a) the vortex cutting simulation described in Section 4.3 and (b) the simple model described in Section 4.4.

We observe higher peaks of both the positive and negative circulation for the vortex cutting simulations compared to the simple model, which is likely an effect of the strong curvature of the vortex around the blade leading edge in the vortex cutting simulations. The qualitative features of the two plots, including the vorticity variation on the time scale τ and the manner in which the stretched vorticity within the flow interacts and is

annihilated by vorticity generated at the surface, appear to be similar between the model and the full simulations.

4.5. Conclusions

Computational results are reported for the cutting of a columnar vortex by a blade without axial flow for different values of the impact parameter, with a particular focus on comparison of the vortex cutting problem to the classic vortex tube reconnection problem. Each of the three phases of vortex tube reconnection were found to have a close analogy in the vortex cutting problem. The first vortex reconnection phase, involving inviscid response to the core resulting in both anti-parallel orientation of the vorticity and core shape deformation, takes the form in the vortex cutting problem of generation of vorticity at the leading edge of the blade due to the spanwise velocity induced by the impinging vortex. While the diffusion of this vorticity into the blade boundary layer is a viscous process, the generation of vorticity at the blade surface is controlled by the inviscid slip velocity along the blade span. The resulting vorticity within the boundary layer wrapping about the blade leading edge is anti-parallel to that within the approaching vortex core.

The second phase of vortex reconnection involves diffusion and annihilation of vorticity within the two anti-parallel vorticity regions. This process occurs in the vortex cutting problem between the vortex core and the boundary layer at the blade leading edge. However, unlike the traditional vortex tube reconnection problem, for vortex cutting the boundary layer vorticity is generated at the blade surface as the vorticity annihilation occurs. A simple exact Navier-Stokes solution illustrating the key processes

involved during this second phase of vortex cutting is described in Section 5, in which we examine the interaction of a vortex sheet above a flat surface in the presence of a straining flow. In this model, the straining flow is in the direction of the vorticity vectors, similar to a Burgers' vortex, and represents the effect of the ambient flow in the stagnation-point region near the blade leading edge. While this model is greatly simplified in order to reduce the problem to a manageable form, and in particular the effect of high curvature at the blade leading edge is ignored, it nevertheless is found to provide a good description of the qualitative features of vortex cutting and to indicate the appropriate temporal and spatial scaling for the problem.

Both the vortex tube reconnection problem and the vortex cutting problem result in incomplete reconnection of the vortex lines across the two vorticity regions; however, the reason that this occurs in the two problems is different. In vortex cutting, the incomplete cutting occurs when the blade leading edge passes sufficiently deeply into the vortex core that the induced spanwise velocity along the leading edge changes sign. After this sign change occurs, the generation of anti-parallel vorticity at the leading edge surface is stopped and the new vorticity generated is parallel to that within the vortex core. When the anti-parallel vorticity in the boundary layer is depleted and replaced by parallel vorticity, the diffusive annihilation of vorticity between the vortex and the boundary layer can no longer occur, effectively stopping the vortex cutting process. What follows corresponds with the third phase of vortex reconnection, in which remnants of the uncut vortex remain for long time, wrapping around the blade boundary layer and stretching under the influence of the ambient flow around the blade.

CHAPTER 5: VORTEX CUTTING WITH NON-ZERO AXIAL FLOW

The third and final study extends the vortex cutting work presented in Chapter 4 to the case of vortices with non-zero axial flow. In particular, the underlying physics of the transient vortex cutting force that results from a vortex with axial flow being cut by a blade will be investigated. Elements of this process that are of specific interest include how the transient cutting force depends on the various dimensionless parameters that govern the flow field, and how the transient force compares to the steady-state vortex cutting force.

5.1. Scaling of the Transient Vortex Cutting Force

First, a scaling analysis is developed to motivate an expression for how the transient vortex cutting force on the blade depends on the various dimensionless parameters governing the flow field. A Cartesian coordinate system is oriented such that the uniform flow is in the *x*-direction, the normal vector of the blade center plane is in the *y*-direction, and the blade span is in the *z*-direction. The orthogonal vortex-blade interaction process is characterized by a number of parameters, including the blade chord *c* and thickness τ, the vortex circulation Γ, core radius σ_0 and maximum ambient axial velocity w_0, the blade speed relative to the vortex core *U*, and the fluid density ρ and kinematic viscosity ν. Using these parameters, the *vortex* and *blade Reynolds numbers* are defined as $\mathrm{Re}_V \equiv \Gamma/\nu$ and $\mathrm{Re}_B \equiv Uc/\nu$. The *thickness parameter* $T = \tau/\sigma_0$ is the ratio of the blade thickness to the vortex core radius while the *impact parameter*

$I \equiv 2\pi\sigma_0 U/\Gamma$ is the ratio of the relative vortex-blade velocity to the maximum swirl velocity within the vortex. The *axial flow parameter* $A \equiv 2\pi\sigma_0 w_0/\Gamma$ is the ratio of the maximum vortex axial velocity to the maximum swirl velocity. Since the propagation speed of axisymmetric waves in the plug-flow vortex model is given by $c_0 = \Gamma/\sqrt{8}\pi\sigma_0$, the axial flow parameter can be interpreted as analogous to a Mach number for the vortex flow.

A schematic diagram showing the coordinate system orientation and the different parameters used to describe vortex cutting is given in Figure 5.1.

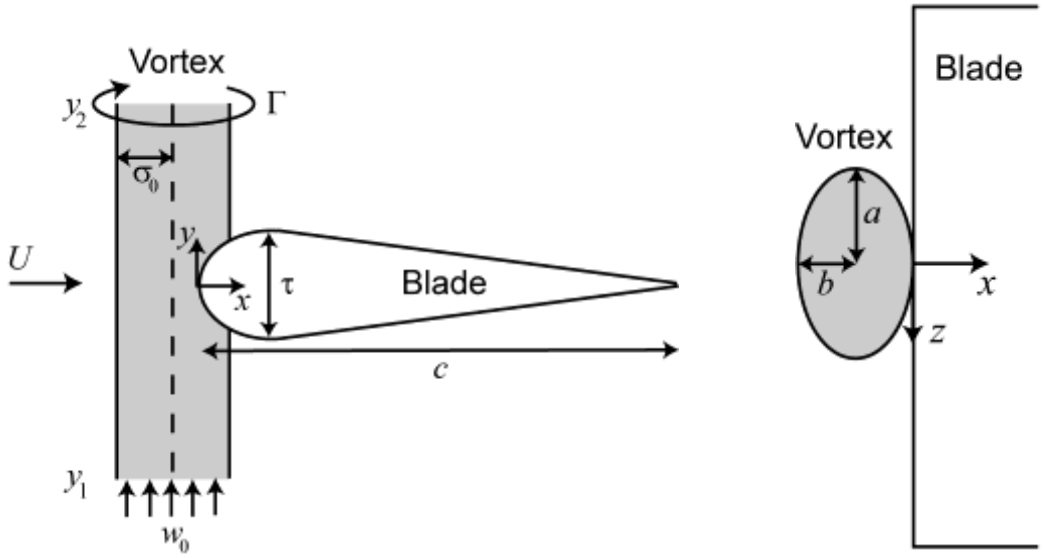

Figure 5.1: Schematic diagram showing the parameters used to describe the vortex cutting problem and the control volume (shaded) used in the scaling analysis, from both (a) the side view and (b) the top view.

The vortex control volume (CV) is shaded grey in Figure 5.1a. Also shown are lower and upper end points y_1 and y_2 along the vortex axis, respectively. Integrating the

momentum equation over this control volume gives the lift force that the fluid exerts on the blade in the positive *y*-direction as

$$L = -\frac{d}{dt}\int_{CV} \rho w \, dv, \tag{5.1}$$

where we assume that the ends of CV on the vortex are sufficiently far from the blade that the axial velocity at each end is approximately equal, or $w(y_2,t) = w(y_1,t)$. The vortex cross section is assumed to have approximately elliptical shape, with major semi-axis $a(\xi,t)$ and minor semi-axis $b(\xi,t)$, where ξ denotes distance along the vortex axis. The effective radius σ and the aspect ratio θ are defined by $\sigma \equiv (ab)^{1/2}$ and $\theta \equiv a/b = (\sigma/b)^2$. Assuming that the axial velocity is uniform across the vortex core (the plug-flow approximation), the lift force is given by

$$L = -\pi\rho \frac{d}{dt}\int_{y_1}^{y_2} abw \, d\xi \,. \tag{5.2}$$

The transient vortex cutting force is caused both by the displacement of the vortex as the blade leading edge penetrates into the vortex core and by the vortex response on either side of the blade. From the full Navier-Stokes simulations discussed in Section 5.4, it was found that the largest change in the vortex appears to be in the vortex radius *b* in the direction of uniform flow while the half-width of the vortex along the blade span, *a,* is relatively constant during the cutting process. The vortex radius *b* decreases from a value

of approximately σ_0 prior to vortex cutting to nearly zero at the conclusion of cutting. The maximum axial velocity $w_{\max}$ increases by about 50% and then decreases again as the blade penetrates into the vortex core. For the purpose of forming a scaling estimate of the lift force, we assume that both *a* and *w* are constant in the integral in (5.2), equal to their initial values σ_0 and w_0, respectively, so that (5.2) becomes

$$L \approx -\pi\rho\sigma_0 w_0 \int_{y_1}^{y_2} \frac{db}{dt}\, d\xi \,. \tag{5.3}$$

It is noted that $db/dt = -U/2$ for all values of ξ corresponding to positions on the blade that have penetrated into the vortex core, which has maximum extent $-\tau/2 < \xi < \tau/2$. However, the value of *b* will also decrease on parts of the vortex on either side of the blade over a distance of scale σ_0. Based upon these approximations, (5.3) yields a scaling estimate for the maximum value of the transient vortex cutting force on the blade, $L_{tr,\max}$, as

$$L_{tr,\max} \cong \frac{\pi}{2}\rho U w_0 \sigma_0 (C_1\tau + C_2\sigma_0) \,. \tag{5.4}$$

where C_1 and C_2 are O(1) constants. If we define a lift coefficient C_L in terms of the ambient vortex axial velocity and core radius as $C_L \equiv L/(\frac{1}{2}\rho w_0^2 \sigma_0^2)$, then the scaling

estimate (5.4) can be written in terms of the axial flow parameter *A*, the impact parameter *I*, and the thickness coefficient *T* as

$$C_{L,tr,\max} \cong \frac{\pi I}{A}(C_1 T + C_2)\,. \tag{5.5}$$

5.2. Steady-State Vortex Cutting Force

In addition to the transient force discussed in Section 5.1, there also exists a steady-state vortex cutting force that is caused by the vortex core radius near the blade surface increasing to a value $\sigma_C > \sigma_0$ on the upstream side of the core and decreasing to a value $\sigma_E < \sigma_0$ on the downstream side of the core following vortex cutting. This difference in core radius leads to a net pressure force on the blade surface. An analytical solution for this pressure force was obtained by Marshall (1994) using the method of characteristics to solve the one-dimensional plug-flow vortex model with instantaneous vortex cutting. For the configuration shown in Figure 5.1a with $w_0 > 0$, the steady-state vortex cutting force L_{ss} can be written in terms of the lift coefficient C_L and the axial flow parameter *A* as

$$C_{L,ss} = \frac{2\pi}{A^2}\ln\left(\frac{\sigma_C}{\sigma_E}\right). \tag{5.6}$$

Therefore, the vortex core radii near the blade on the downstream (expansion) side and the upstream (compression) side, relative to the vortex axial flow, can similarly be written in terms of the axial flow parameter as

$$\frac{\sigma_E}{\sigma_0} = \frac{1}{1+(\sqrt{2}/2)A} \tag{5.7}$$

and

$$A^2\phi^2 = (\phi^2 - 1)\ln(\phi), \tag{5.8}$$

where $\phi \equiv \sigma_C / \sigma_0$ must be solved iteratively from (5.8).

As the axial flow parameter becomes sufficiently large ($A >> 1$), (5.8) admits the asymptotic solution

$$\phi \sim \exp(A^2). \tag{5.9}$$

This solution requires only that $\phi^2 >> 1$, and so has an error of only 1.8% at $A = 2$. Substituting (5.9) and (5.7) into (5.6) gives an asymptotic solution for the steady-state vortex cutting force for $A >> 1$ as

$$C_{L,ss} \sim 2\pi + \frac{2\pi}{A^2}\ln\left(1 + \frac{\sqrt{2}}{2}A\right). \tag{5.10}$$

For small axial flow parameters ($A << 1$), (5.8) admits an asymptotic solution of the power series form

$$\phi \sim 1 + \frac{1}{\sqrt{2}} A + \frac{1}{2} A^2 + O(A^3) . \tag{5.11}$$

Using (5.11) and (5.7) in (5.6) and retaining two terms in the small parameter A yields an asymptotic solution for the steady-state vortex cutting lift coefficient for $A << 1$ as

$$C_L \sim \frac{2\sqrt{2}\,\pi}{A} + DA, \tag{5.12}$$

where $D = 5\sqrt{2}\,\pi/16 \cong 1.3884$ is an O(1) constant.

5.3. Heuristic Model of Vortex Response to Cutting

In this section a one-dimensional heuristic model of the vortex response during cutting and the development of the blade lift force is developed using an approach motivated by the plug-flow vortex model of Lundgren and Ashurst (1989) and the vortex tube reconnection model of Saffman (1990). The primary purpose of this one-dimensional model is to explore the relative role of the different forces acting on the vortex during cutting and the qualitative response of the vortex axial velocity and core radius and of the blade lift to these forces.

Accurate solution of (5.2) for the blade lift force during vortex cutting requires knowledge of how the vortex axial velocity and core radius change along the vortex as a function of both time and position. As a blade penetrates into a vortex core, the vortex axial flow comes into contact with the blade surface resulting in a shear force that

opposes the axial transport of fluid in the vortex. At the same time, an external pressure gradient is generated along the vortex core as the vortex comes into contact with the high pressure region near the blade leading edge. Finally, as a result of further blade penetration, the vortex core becomes pinched such that the semi-minor axis $b(\xi,t)$ reduces in time within the blade penetration region. Together these different effects cause changes in both the vortex core effective radius $\sigma(\xi,t)$ and the axial velocity $w(\xi,t)$. The simplified one-dimensional model of Lundgren and Ashurst (1989), which assumes the presence of a uniform axial velocity distribution (i.e., a 'plug flow') within the core, is one approach to understanding the time and spatial variation of the core radius and axial velocity. Application of a similar model to the vortex tube reconnection problem was given by Saffman (1990), in which the axial variation of vortex circulation caused by the vortex reconnection was shown to give rise to an internal pressure gradient within the vortex core. Saffman's model was found to be in reasonable qualitative agreement with data from full Navier-Stokes solutions of vortex tube reconnection (Shelley et al., 1993).

The equations of continuity and conservation of momentum for the plug-flow vortex model are given by

$$\frac{\partial}{\partial t}(\sigma^2)+\frac{\partial}{\partial \xi}(\sigma^2 w)=0, \tag{5.13}$$

$$\frac{\sigma^2}{2}\left(\frac{\partial w}{\partial t}+w\frac{\partial w}{\partial \xi}\right)=-\frac{1}{\rho}\int_0^{\sigma}\frac{\partial p}{\partial \xi}r dr-\frac{a}{\rho}\tau_w. \tag{5.14}$$

where the pressure integral in (5.14) is across the vortex core, $\sigma \equiv (ab)^{1/2}$ is the equivalent core radius, and the last term in (5.14) is added to account for the frictional force between the vortex axial flow and the blade leading edge. Following Saffman (1990), the pressure at a radius *r* from the vortex axis can be expressed as a function of aspect ratio θ as

$$\frac{p(r) - p_\infty}{\rho} = -\frac{\Gamma^2 g(\theta)}{4\pi^2 \sigma^4}(2\sigma^2 - r^2), \tag{5.15}$$

where $g(\theta) = \theta/(1+\theta^2)$ for $\theta > 1$. Substituting (5.15) into (5.14) and performing the integration over *r* gives

$$\frac{\partial w}{\partial t} + w\frac{\partial w}{\partial \xi} = -\frac{\Gamma^2 g(\theta)}{2\pi^2 \sigma^3}\frac{\partial \sigma}{\partial \xi} + \frac{3}{8\pi^2 \sigma^2}\frac{\partial}{\partial \xi}[\Gamma^2 g(\theta)] - \frac{1}{\rho}\frac{\partial p_\infty}{\partial \xi} - \frac{2}{\rho b}\tau_w . \tag{5.16}$$

Eq. (5.16) reduces to the standard plug-flow model when $b = \sigma$ and Γ is constant, with the addition of the external pressure gradient and shear force terms.

For simplicity, it is assumed that the vortex axis does not bend due to the inviscid interaction with the blade, so that we can set $\xi = y$. The external pressure gradient $\partial p_\infty / \partial y$, the shear stress τ_w, and the variation in vortex circulation $\Gamma(y,t)$ can all be approximated using the results of full Navier-Stokes solutions for uniform flow past a blade (NACA0012 airfoil), which are given by Saunders and Marshall (2015) for

no axial flow and in Section 5.4 of the current paper with axial flow. For the external pressure variation, results from Saunders and Marshall (2015) yield

$$p_\infty \cong 0.16\,\rho U^2 \exp[-(y/\tau)^2], \tag{5.17}$$

so that the external pressure gradient force per unit mass F_P acting on the vortex is

$$F_P = -\frac{\partial(p_\infty/\rho)}{\partial y} \cong 0.32U^2(y/\tau^2)\exp[-(y/\tau)^2]. \tag{5.18}$$

The effect of this external pressure gradient is to produce an axial flow moving away from the vortex cutting region, thus thinning the vortex core near the location of vortex cutting and increasing the vortex core radius on both sides of the blade.

The blade shear stress τ_w plays a critical role in reducing the axial velocity within the vortex core in the vortex cutting region. The shear stress is approximated by

$$\tau_w \cong \mu w f(t)/\delta, \tag{5.19}$$

where δ is a characteristic boundary layer thickness and $f(t)$ is the spanwise length of the region on the blade surface over which the shear stress acts. The function $f(t)$ can be regarded to behave as a type of ramp function for the shear stress, which varies from 0 when the vortex core axial flow first makes contact with the blade leading edge to approximately unity once the blade has penetrated half-way through the vortex core. For

convenience, the current study assigned $f(t)$ to be a simple hyperbolic tangent function, given by $f(t) = \tanh(2t/t_{cut})$. Here, $t = 0$ corresponds to the time at which the blade leading edge first contacts the vortex and $t_{cut} = 2\sigma_0 / U$ is the nominal cutting time. The length scale δ is assumed to be proportional to the 99% stagnation-point boundary layer thickness δ_{sp} at the blade leading edge, given by

$$\delta_{sp} = 2.40(\nu / s)^{1/2} \cong (\nu\tau / U)^{1/2}. \tag{5.20}$$

using the estimate $s \cong 5.3U/\tau$ for strain rate *s* at the blade leading edge (Saunders and Marshall, 2015). The shear stress from (5.19) becomes $\tau_w \cong C_{shear}\mu w f(t)/\delta_{sp}$, where C_{shear} is a constant of proportionality, so that using (5.20) the shear force per unit mass acting on the vortex (i.e., the last term in (5.16)) can be written as

$$F_S = -\frac{2\tau_w}{\rho b} \cong -2C_{shear}\frac{w}{b}\left(\frac{\mu U}{\rho\tau}\right)^{1/2} f(t). \tag{5.21}$$

The shear stress on the blade surface was measured for a range of different parameters values in the full Navier-Stokes simulations described in Section 5.4. In each case, (5.21) was used to estimate the coefficient C_{shear} from the computational data. The values obtained varied between 4–10. While this is a fairly wide range of variation, no doubt a consequence of the fact that the above equation for wall shear stress is just a rough estimate, the computed lift force on the blade was fortunately found not to be particularly

sensitive to this coefficient (as seen from comparison of predictions with both C_{shear} = 4 and 10).

The 'circulation gradient force' F_C is given by the second term on the right-hand side of (5.16), or

$$F_C = \frac{3}{8\pi^2\sigma^2}\frac{\partial}{\partial y}[\Gamma^2 g(\theta)]. \tag{5.22}$$

This force is induced by the internal pressure gradient associated with the axial gradient in vortex circulation that arises as a consequence of vortex reconnection, and it featured prominently in the vortex tube reconnection model of Saffman (1990). The aspect ratio can be computed in terms of the minor axis length *b* and the effective radius σ using $\theta = (\sigma / b)^2$, where a smoothly-varying approximation for *b* is assumed in the form

$$b(y,t) \cong 1 - (Ut/2)\exp[-(2y/\tau)^2]. \tag{5.23}$$

The vortex circulation is approximated using data from the full Navier-Stokes simulation (Saunders and Marshall, 2015) as

$$\Gamma(y,t) \cong \Gamma_0[1 - \tanh(t/t_{cut})]\exp[-(2y/\tau)^2] \ . \tag{5.24}$$

Equations (5.13) and (5.16) were solved using the McCormack finite-difference algorithm. The time step and spatial step size were chosen as $w_0 dt/\sigma_0 = 0.001$ and $dx/\sigma_0 = 0.02$ respectively while the shear coefficient C_{shear} was chosen to be 4 and 10. Representative solutions for the effective core radius and axial velocity at four different times during the vortex cutting process are plotted in Figure 5.2 for a case with dimensionless parameter values $I = 1$, $A = 2$, $T = 1$, $\mathrm{Re}_A = 500$ and $C_{shear} = 10$. In addition, a set of plots for this computation showing the dimensionless shear force $F_S/\sigma_0 w_0^2$, the dimensionless external pressure gradient force $F_P/\sigma_0 w_0^2$, and the dimensionless 'circulation gradient' force $F_C/\sigma_0 w_0^2$ is given for the same four times in Figure 5.3. Further computations were performed with different combinations of these forces turned off in order to understand the role that each force plays in the overall solution.

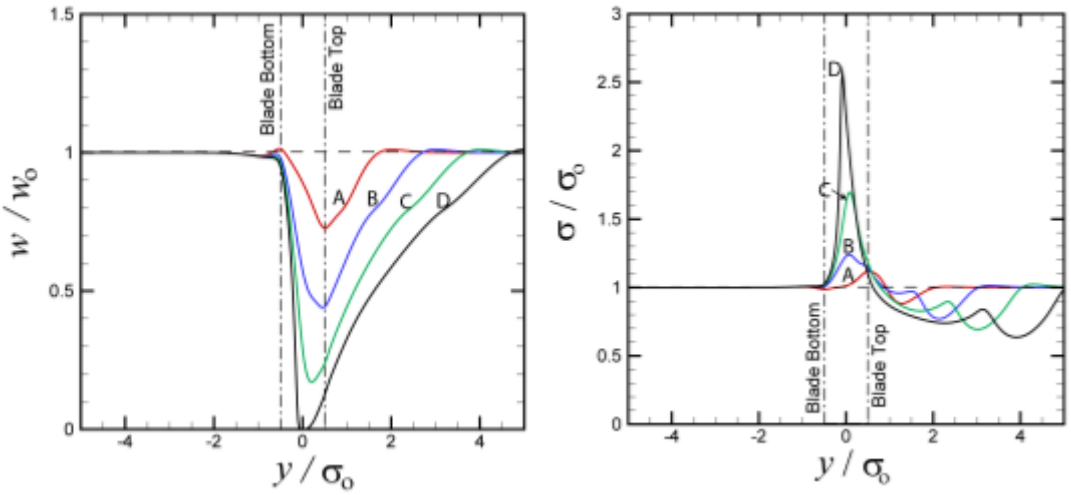

Figure 5.2: Computational results for (a) vortex axial velocity and (b) effective core radius from the plug-flow model for a case with dimensionless parameter values $I = 1$, $A = 2$, $T = 1$ and $\mathrm{Re}_A = 500$. The plots are drawn for times $w_0 t/\sigma_0 = 0$ (dashed), 1 (A, red), 2 (B, blue), 3 (C, green) and 4 (D, black), where the last time coincides with the vortex cutting time.

The vortex flow field in Figure 5.2 is divided into an upstream 'compression region' ($y < 0$) and a downstream 'expansion region' ($y > 0$) in which the core is axially compressed or expanded by the axial flow, respectively, and ‘upstream’ and ‘downstream’ are with respect to the core axial velocity. The vortex axial velocity is decreased near the blade and within a region lying between the blade surface and the vortex expansion far downstream of the blade due to the strong shear force between the blade leading edge and the vortex axial flow. The shear force similarly results in an increase in vortex effective core radius σ immediately upstream of the blade leading edge and a corresponding decrease in σ downstream of the blade. The increase (decrease) in effective vortex core radius on the upstream (downstream) side of the vortex from the cutting blade is consistent with the experimental observations and inviscid computations of Marshall and Krishnamoorthy (1997) and the full Navier-Stokes simulations of Liu and Marshall (2004). From Figure 5.3, we observe that both the external pressure gradient force and the circulation gradient force have much smaller magnitudes than the shear force, so the vortex core response to the blade is governed primarily by the shear force.

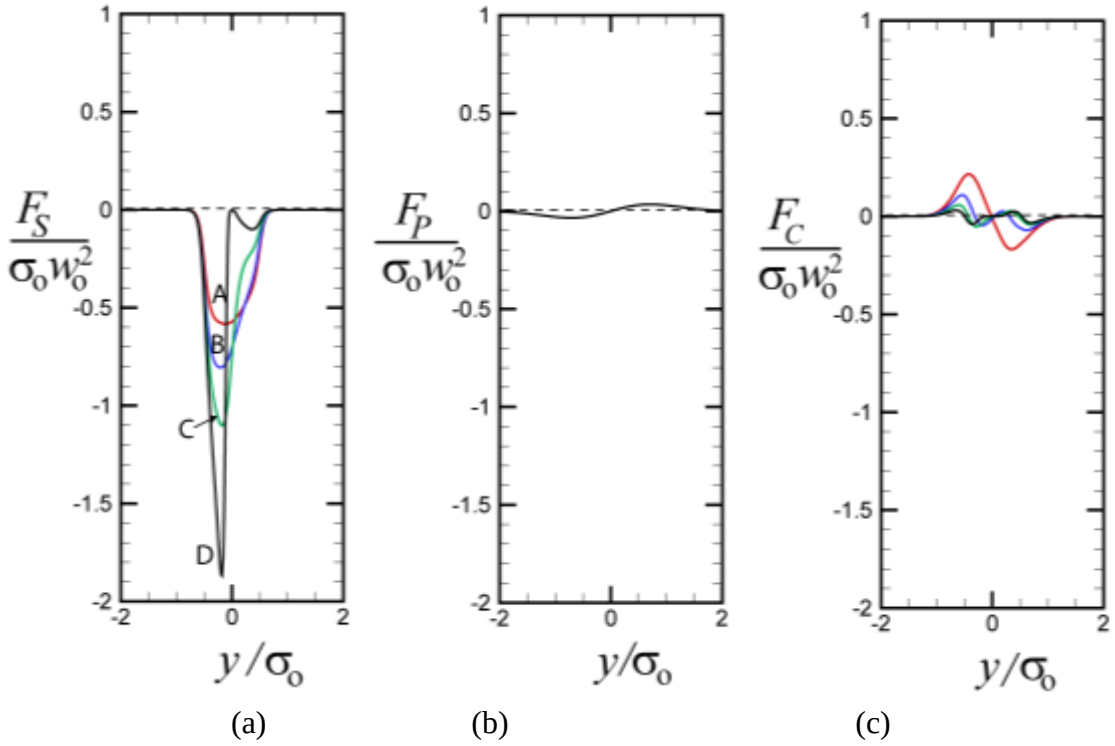

Figure 5.3: Plots showing variation along the vortex core of (a) the shear force F_S, (b) the pressure gradient force F_P, and (c) the vortex circulation gradient force F_C, per unit mass, at times $w_0 t/\sigma_0 = 0$ (dashed), 1 (A, red), 2 (B, blue), 3 (C, green) and 4 (D, black), for the same case as shown in Figure 5.2. The pressure gradient force does not change in time.

The blade lift coefficient C_L is obtained by computing the lift force by numerical evaluation of the integral in (5.2) using the trapezoidal rule with the computed values of core radius and axial velocity from solution of (5.13) and (5.16). The lift coefficient exhibits a peak value $C_{L,\max}$ shortly before the end of the vortex cutting process and then decreases at later times. A series of computations was conducted to determine how $C_{L,\max}$ varies with the values of the dimensionless parameters *A*, *I* and *T* for both $C_{shear} = 4$ and 10, the results of which are plotted in Figure 5.4.

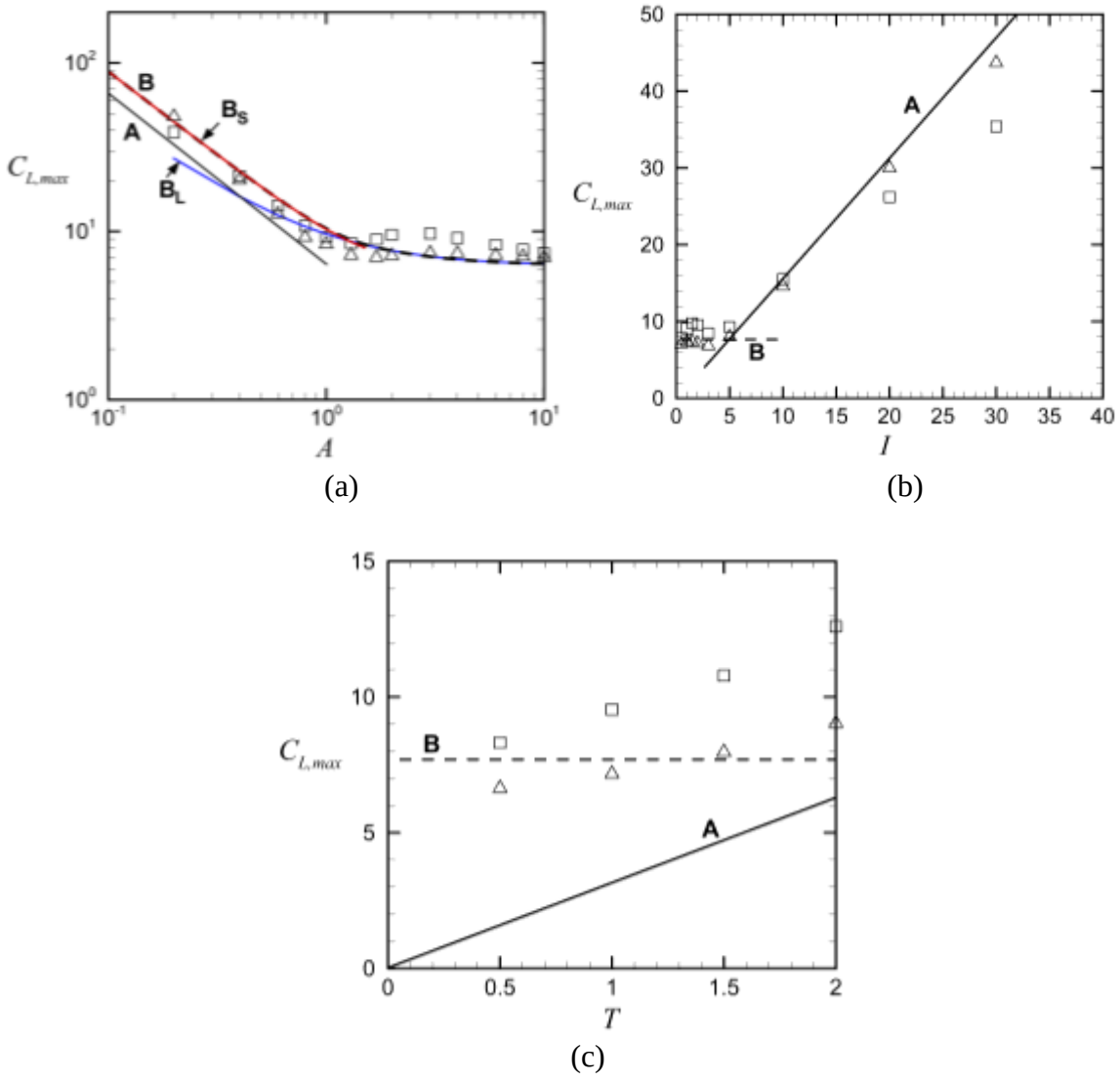

Figure 5.4: Variation of lift coefficient predicted from the plug-flow vortex model with (a) axial flow parameter (with $I = 2$ and $T = 1$), (b) impact parameter (with $A = 2$ and $T = 1$), and (c) thickness parameter (with $A = 2$ and $I = 2$). The plug-flow model results are for $C_{shear} = 4$ (squares) and 10 (deltas). Line A (solid black) represents the scaling estimate (5.5) for the transient vortex cutting force with $C_1 = 1$ and $C_2 = 0$ and line B (dashed) is the steady-state vortex cutting force prediction obtained by solving Eqs. (5.6)-(5.8). The asymptotic solutions for the steady-state vortex cutting force are indicated in (a) by line B_L (blue) for large axial flow parameters and by line B_S (red) for small axial flow parameters.

The vortex model solutions are compared to the scaling estimate (5.5) for the maximum transient vortex cutting force, which is indicated in these figures by line **A**. In comparing to the scaling solution for the transient lift force, we select the coefficients C_1 and C_2 in

(5.5) as $C_1 = 1$ and $C_2 = 0$ in Figure 5.4, which appears to give the best fit to the data. The steady-state vortex cutting force was obtained by iterative solution of (5.8) for $\phi = \sigma_C / \sigma_0$ using the false position method and plugging the result into (5.6), with the result indicated by line **B** in Figure 5.4. In Figure 5.4a, the value of $C_{L,\max}$ is plotted versus the axial flow parameter *A* using a log-log plot, where *A* varies over the interval (0.1,10). In this plot, we also show the solutions obtained from the asymptotic expansions (5.10) and (5.12) for the steady-state vortex cutting force at large and small values of *A*, indicated in Figure 5.4a by lines $\mathbf{B_L}$ and $\mathbf{B_S}$, respectively. The computational solutions from the plug-flow model are in good agreement with the steady-state vortex cutting force solution for all values of *A*, as well as in reasonably good agreement with the transient vortex cutting force solution (5.5) for $A<1$. We also note that the two asymptotic solutions (5.10) and (5.12) for the steady-state vortex cutting force are close to the full solution for $A<1.2$ and for $A\geq 1.2$, respectively. In the Figure 5.4b, showing variation of $C_{L,\max}$ with the impact parameter *I*, the transient vortex cutting force prediction (5.5) agrees well with the computational solution for $I>5$, and the steady-state vortex cutting solution agrees with the computational data in the range $I<5$, for which the transient force prediction is less than the steady-state force prediction. Figure 5.4c shows the variation of $C_{L,\max}$ with the thickness parameter *T*. For low values of *T* the plug-flow model predictions for $C_{L,\max}$ are not very sensitive to the value of *T*, and are given with reasonable accuracy by the steady-state solution. For large values of *T* (e.g., $T>4$) the plug-flow model predictions agree well with the transient lift force model (5.5); however, results with *T* larger than about 2 are not physically meaningful, since for

such cases the vortex bends significantly prior to impingement on the vortex (Marshall and Yalamanchili, 1994), and they are therefore not shown in Figure 5.4.

5.4. Full Navier-Stokes Simulations

The previous sections discuss some of the physics that gives rise to the transient and steady-state vortex cutting forces on the blade in terms of both analytical solutions and a one-dimensional heuristic model based on the plug-flow approximation. This section seeks to examine the validity of these model predictions using full Navier-Stokes simulations of a blade with zero angle of attack cutting through the core of a vortex with non-zero axial flow.

5.4.1. Numerical Method

The Navier-Stokes equations were solved in primitive-variable form using a finite-volume method (Lai, 2000) on a block-structured mesh with hexahedral elements and eight implicitly-coupled blocks. The grid was designed to provide smooth grid cell variation and high spatial accuracy in the region surrounding the blade leading edge, where the vortex cutting occurs (Figure 5.5a). The computational algorithm employed is described in more detail in Section 4.2.

The computations were initialized with a columnar vortex with strength Γ convected by a uniform flow with speed U toward a fixed blade. The variation of swirl velocity and axial velocity with radius within the initial columnar vortex were specified as Gaussian functions. The initial position of the vortex axis was located approximately four vortex core radii upstream of the blade leading edge in order to allow the blade boundary layer time to grow in a natural way as the vortex approaches. When initialized

as a Gaussian vortex, the vortex swirl (u_θ) and axial (w) velocity fields were observed to remain Gaussian by the time the vortex reached the blade leading edge, with form

$$u_\theta = \frac{\Gamma}{2\pi r}\left[1-\exp\left(-r^2/\sigma_0^2\right)\right], \qquad w = w_0 \exp\left(-r^2/\sigma_0^2\right). \tag{5.25}$$

The vortex maximum axial velocity and core radius at a time just before onset of cutting of the vortex by the blade were measured, and are denoted by w_0 and σ_0, respectively.

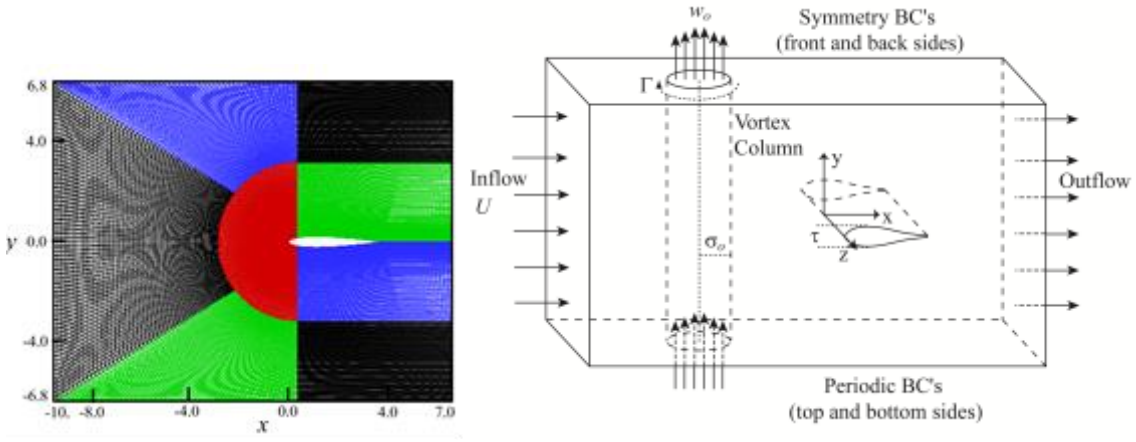

(a) (b)

Figure 5.5: (a) Cross-sectional view of the computational grid in the plane $z = 0$ and (b) schematic diagram showing boundary conditions, as used for the full Navier-Stokes simulations. The inlet and outlet planes are at $x = -10$ and $x = 7$, respectively, and the blade span length is equal to 10.

Standard inflow and outflow boundary conditions were used for the boundary planes in the *x*-direction, and periodic and symmetry boundary conditions were used in the *y*- and *z*-directions, respectively, as shown in Figure 5.5b. The blade was a NACA symmetric airfoil with chord length *c*, thickness τ, and with the leading edge lying on the line $x = 0$. The computational domain spanned the region $-10 \le x/\sigma_o \le 7$, $-6.8 \le y/\sigma_o \le 6.8$, and $-5 \le z/\sigma_o \le 5$, where the blade center plane is given by the

intersection of the blade with the y = 0 plane. The vortex axis was initialized on the central plane ($z_0 = 0$) at a location $x_0 / \sigma_o = -4.4$ upstream of the blade leading edge, and the inlet plane was located upstream of the blade leading edge at $x_{inlet} / \sigma_o = -10$.

The values of the various dimensionless parameters used for the Navier-Stokes computations are listed in Table 5.1. The vortex Reynolds number is set at $\mathrm{Re}_V = 1500$ for all cases examined. The impact parameter I varies from 1.4 to 44.5, the axial flow parameter A varies from 0.06 to 11, and the thickness parameter T varies from 0.13 to 1.05. The impact parameter is maintained at a sufficiently large value that no boundary layer separation is observed prior to impact of the blade onto the vortex. The blade Reynolds number Re_B varies inversely to the impact parameter, ranging from 2000 to 15,000 for the different cases examined. A dimensionless time step of $\Delta t = 0.06$ was chosen to ensure a CFL number of less than unity for all computations.

Table 5.1: Values of the dimensionless parameters for the reported computations.

Case	$T = \tau / \sigma_0$	Re_B	$I = \frac{2\pi\sigma_o U}{\Gamma}$	$A = \frac{2\pi\sigma_o w_0}{\Gamma}$	Symbol (figure 5.15)
1	0.48	15,000	11.6	0.06	+
2	0.48	15,000	11.6	0.3	Δ
3	0.48	15,000	11.6	0.6	*
4	0.48	15,000	11.6	3.0	□
5	0.48	15,000	11.6	6.0	♦
6	0.48	15,000	11.6	11.0	●
7	0.48	2,000	1.4	0.6	NA
8	0.48	7,500	5.7	0.6	▲
9	0.48	38,500	27.0	0.6	x
10	0.48	57,500	44.5	0.6	■
11	0.13	15,000	11.6	0.6	#
12	0.26	15,000	11.6	0.6	○
13	1.05	15,000	11.6	0.6	◊
14	2.10	15,000	11.6	0.6	∇

All length variables are non-dimensionalized using the ambient vortex core radius σ_0, velocity variables are non-dimensionalized by the freestream velocity U, time is non-dimensionalized by σ_0 / U, and vorticity is non-dimensionalized by the inverse time

scale U/σ_0. Pressure and shear stress are non-dimensionalized by ρU^2, where ρ is the fluid density.

Grid independence of the simulation results was examined by repeating the run for Case 5 with four different meshes, where the total number of grid points varied by a factor of 4.4 between the coarsest and finest meshes. The meshes are labeled as mesh A-D, with the number of grid points varying from 860,886 to 3,750,288 points. Grid independence was evaluated by calculating the maximum lift coefficient on the blade during vortex cutting, where all computations and grids had the same parameter values, domain size and block mesh structure. The results are shown in Table 5.2, including the number of grid points and the maximum value of the lift coefficient for each mesh. The maximum lift coefficient had a difference of 1.4% between the two finest meshes, and all subsequent computations were performed with the finest mesh D.

Table 5.2: Results of grid independence study, comparing results for meshes (A-D).

Mesh	Number of Grid Points	$C_{L,\max}$	% difference with previous grid
A	860,866	12.6	
B	1,459,808	12.3	2.4
C	2.446.848	13.6	9.5
D	3,750,288	13.8	1.4

The effect of domain size was also considered to ensure the accuracy of the numerical simulations. The most important parameter was the distance between the initial position of the vortex core and the inlet plane. If this distance was set too small, the induced velocity from the vortex caused weak positive *y*-vorticity to be generated on the inlet plane, which propagates towards the blade behind the vortex. When this vorticity

reaches the blade leading edge it diffusively cancels with the uncut portion of the vortex core that was stretched around the blade leading edge. Several domains were examined, and the mesh in Figure 5.5a was chosen in order to ensure that the strength of this inlet vorticity was small and that it did not reach the blade until very late in the computation.

5.4.2. Vortex Cutting with Axial Flow

The vortex cutting process occurs due to the diffusive cross-cancellation of vorticity within the vortex core to that on the blade leading edge. To illustrate this process, the positive and negative circulation measures, defined by

$$\Gamma^{+} = \int_{L} \omega_y^{+}\, dx\,, \qquad \Gamma^{-} = \int_{L} \omega_y^{-}\, dx\,, \tag{5.26}$$

where $\omega_y^{+} = \begin{cases} \omega_y & \text{if } \omega_y > 0 \\ 0 & \text{if } \omega_y \le 0 \end{cases}$ and $\omega_y^{-} = \begin{cases} 0 & \text{if } \omega_y > 0 \\ -\omega_y & \text{if } \omega_y \le 0 \end{cases}$ were calculated along a line L on the blade symmetry plane as shown in Figure 5.6a. We recall that the *y*-coordinate direction coincides with the direction along the axis of the ambient vortex. The vortex initialized in this study possessed negative *y*-vorticity within the vortex core. As the vortex core approached the blade, the induced velocity created a boundary layer of positive *y*-vorticity along the blade leading edge, the growth of which corresponds to the increase in positive circulation in Figure 5.6b.

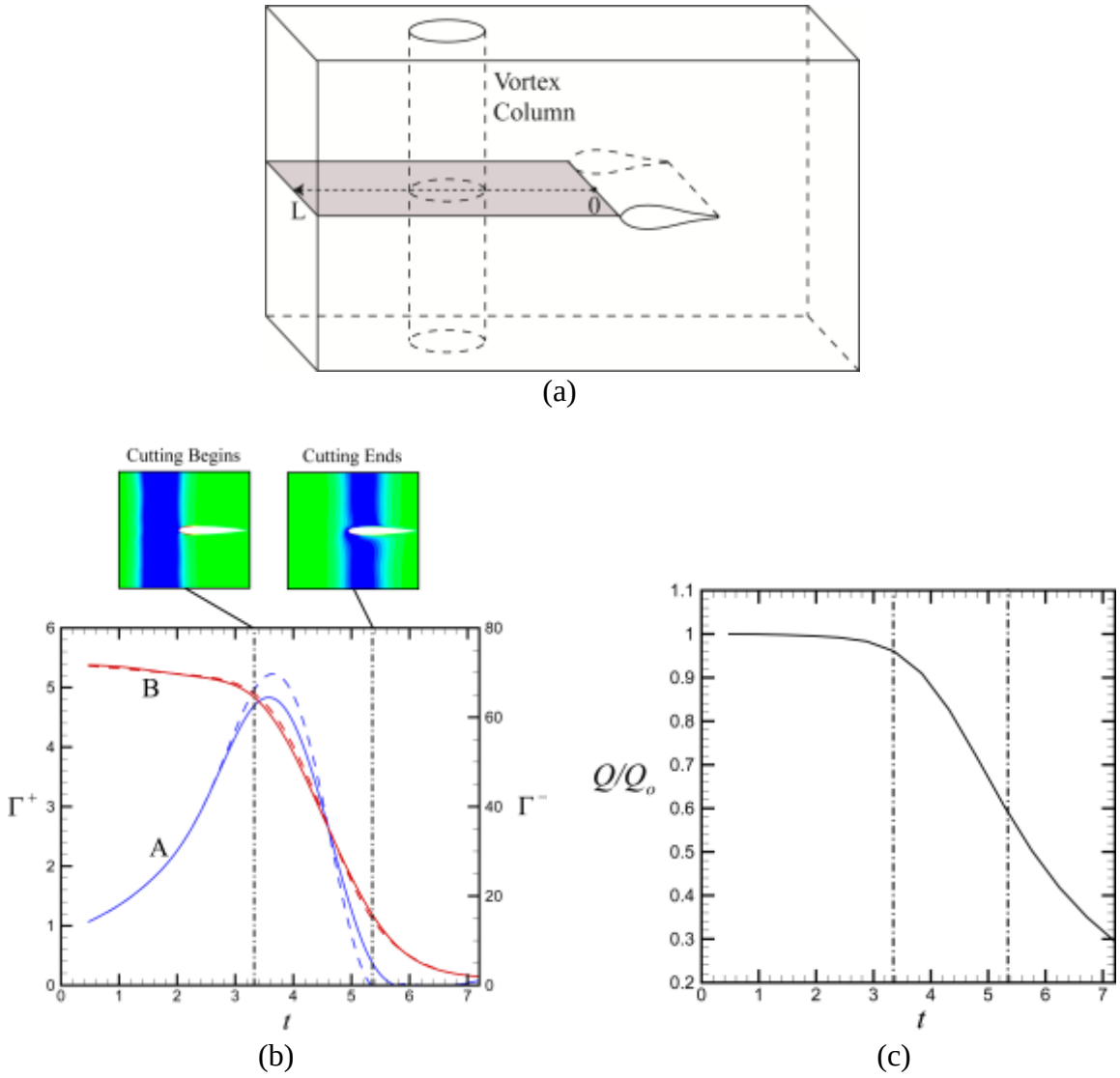

Figure 5.6: (a) The line, L, and plane (shaded region) over which the circulation, Γ, and flow rate, *Q*, were calculated in (b) and (c), respectively. (b) Positive and negative circulation measures, Γ^+ (A, blue curve) and Γ^- (B, red curve), versus dimensionless time for Case 5 (solid lines) and for the Case 5 with no axial flow (dashed lines). The circulation was calculated along a line extending out from the blade front in the –*x* direction as shown in (a). (c) Flow rate, *Q*, in the *y*-direction along the blade symmetry plane ($y = 0$), non-dimensionalized by the initial value. Vertical dashed-dotted lines correspond to the nominal starting and ending times for vortex cutting (*t* =3.36 and 5.36, respectively), as shown in the insert to (b).

As the blade began to penetrate into the vortex core ($t = 3.4$), the induced positive *y*-vorticity in the blade boundary layer diffusively cancelled with the negative *y*-vorticity in

the vortex core. This vorticity diffusion caused the vortex lines within the core to be cut and to reconnect to the vortex lines within the blade boundary layer, decreasing both the positive and negative circulation measures. Once the vortex centerline passes over the blade leading edge, this induced vorticity in the leading edge boundary layer changes sign, which in turn stops the vortex cutting process as the positive circulation measure approaches zero (Figure 5.6b). As time advances further, the uncut portion of the vortex stretches over the blade leading edge to form a vortex sheet, but it cannot be cut due to a lack of positive *y*-vorticity in the boundary layer. As the vortex advects sufficiently far downstream, the induced velocity from the stretched, uncut vortex sheet increases in strength relative to that from the main vortex and positive *y*-vorticity will again form in the blade leading edge boundary layer, indicating a second, slower stage of vortex cutting.

A comparison of the time variation of Γ^+ and Γ^- is also given in Figure 5.6b between a computation with ambient axial vortex flow (Case 5) and the same run but with no ambient axial vortex flow. The results for Γ^- (corresponding to the vorticity within the vortex structure) for the computations with and without ambient axial flow are nearly identical. The positive circulation measure Γ^+ (corresponding to the vorticity in the blade boundary layer) is slightly higher for the computation without ambient axial flow near the start of the blade penetration into the core and slightly lower the end of the vortex cutting process compared to the case with axial flow, but the differences are small. Overall, we conclude that axial core flow does not have a large influence on the vortex cutting process.

The volumetric flow rate in the axial direction through the plane extending out from the center of the blade is plotted in Figure 5.6c as a function of time. The flow rate depends on both the magnitude of axial velocity within the core and the core radius of the vortex. The flow rate remains relatively constant until the cutting process begins. Once vortex cutting starts, the axial flow rate decreases sharply. It then continues to decrease more gradually as the core remnant is stretched along the blade leading edge. A time series of contour plots of both the axial velocity and *y*-component of vorticity in the *x*-*z* plane are given in Figure 5.7. After the cutting process ends following the change of sign of the leading edge boundary layer vorticity, the remaining core deforms as it is stretched along the span of the blade (Figure 5.7c).

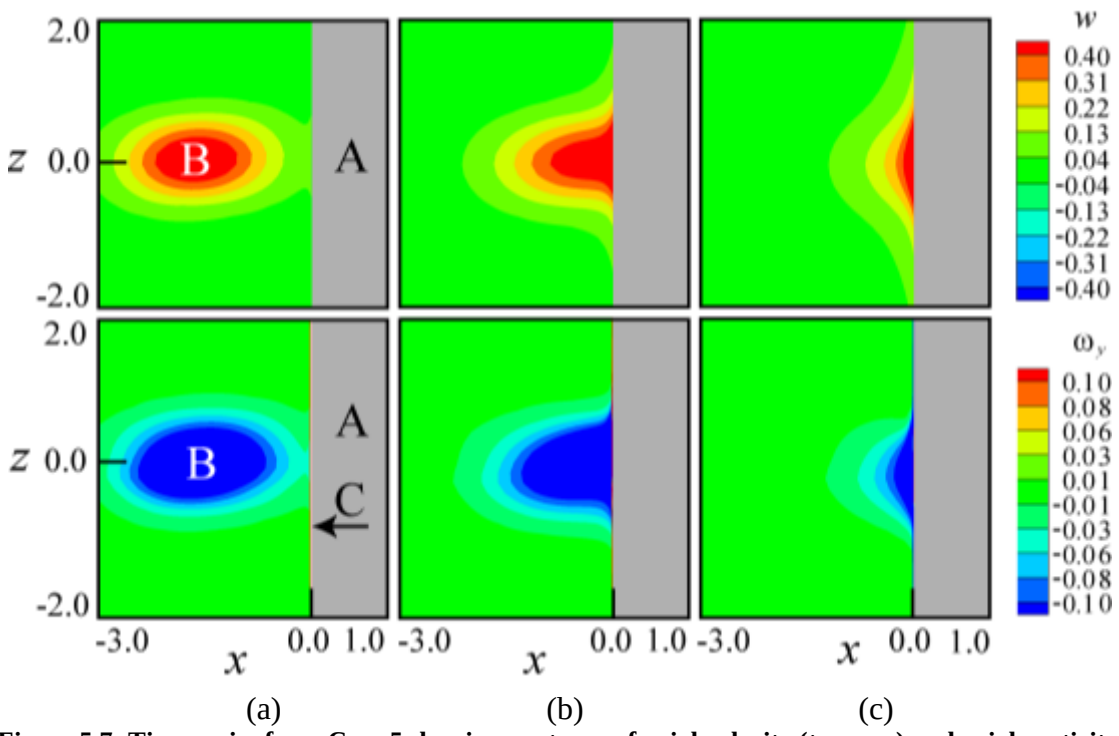

Figure 5.7: Time series from Case 5 showing contours of axial velocity (top row) and axial vorticity (bottom row) in the blade symmetry plane ($y = 0$) at times (a) t = 2.88 , (b) 4.08, and (c) 5.28. The blade surface is labeled as A, vortex core as B, and blade boundary layer as C.

While the change in sign of induced *y*-vorticity nominally corresponds to when the center of the vortex core passes over the blade leading edge, both the axial flow and the blade thickness parameter, *T*, were found to affect this change in sign. Figure 5.8 shows a time series of contour plots in the *x*-*y* plane for Cases 5 and 13. In Case 5, the blade thickness parameter is set to T = 0.48 and the vorticity along the blade leading edge begins to change sign as the core center passes over the blade leading edge. However, the presence of upward axial flow causes this change in sign to occur first on the top surface of the blade (Figure 5.8c).

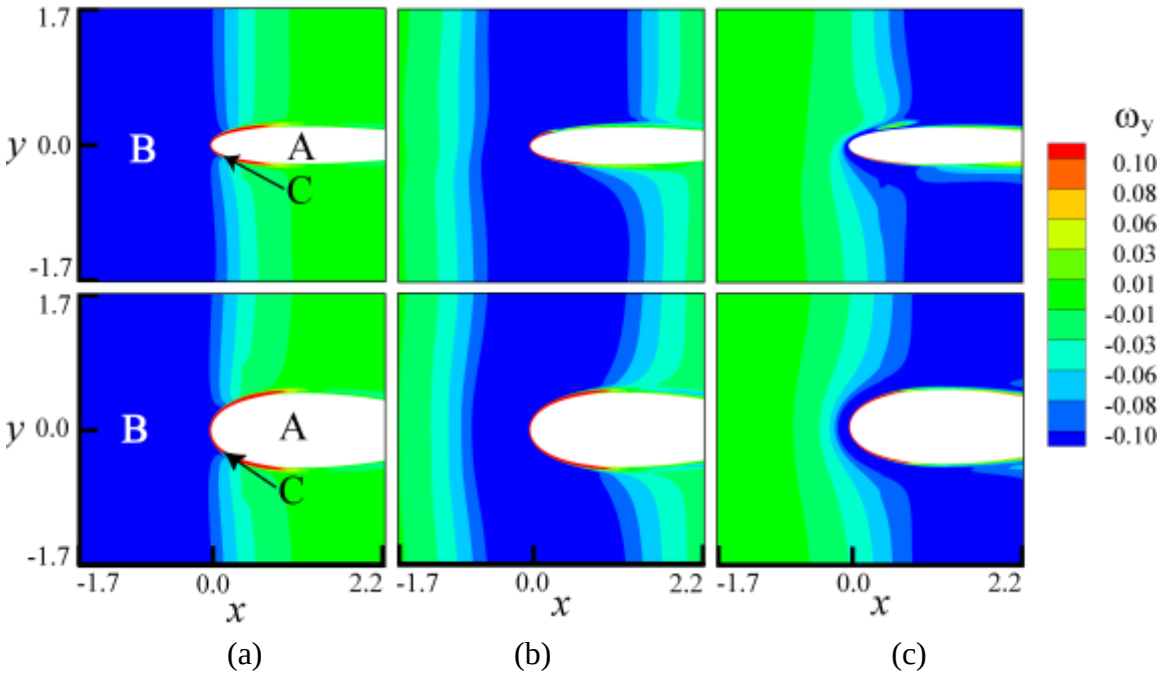

(a) (b) (c)

Figure 5.8: Contours of the vorticity component ω_y in a plane $z = 0$ along blade leading edge for cases with thickness parameter values T = 0.48 (Case 5, top row) and T = 1.05 (Case 13, bottom row) at times (a) t = 3.6, (b) 4.8, and (c) 6. The blade cross-section is labeled as A, vortex core as B, and blade boundary layer as C.

In the bottom row of Figure 5.8, the blade thickness is increased such that T = 1.05. In this case, as the vortex core passes over the blade leading edge, the induced y-vorticity does not change sign but instead remains positive within a region directly underneath the stretched vortex sheet (Figure 5.8c). Vortex lines for the case with T = 1.05 (Case 13) are shown in Figure 5.9 from two different perspectives.

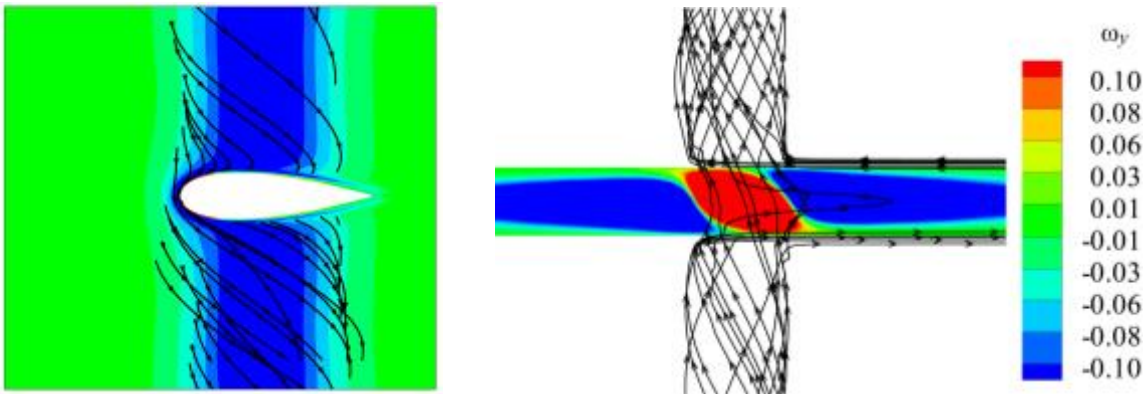

(a) (b)

Figure 5.9: Contour plots from Case 13 of ω_y (a) in the *x*-*y* plane and (b) on the blade surface projected onto the *y*-*z* plane, viewed from a perspective looking in the *x*-coordinate direction, at *t* = 6. Vortex lines in both the vortex core and blade boundary layer are plotted in black.

The axial velocity within the vortex core causes the vortex lines to swirl around the core as they travel upwards. Figure 5.9b shows a contour plot of *y*-vorticity on the blade surface projected onto the *y*-*z* surface, viewed from a perspective looking in the *x*-coordinate direction. The change in sign of *y*-vorticity occurs along the ends of the blade span after the vortex center passes by the blade leading edge, but in the blade center the change in sign is opposed by the velocity induced by the stretched (uncut) portion of the vortex that wraps around the blade leading edge. Also shown are the vortex lines that have been cut from the vortex core and have re-connected with the vortex lines from within the blade boundary layer.

5.4.3. Lift Force on the Blade

As a blade penetrates into the core of a vortex with axial flow, a transient lift force forms which peaks and then diminishes during the cutting period. As discussed in Section 5.2, a steady-state lift force can also occur due to the difference in vortex core radius across the blade surface after cutting of the vortex is complete. In this section, the effect of the different dimensionless parameters on the lift force is examined using full

Navier-Stokes simulations for the different cases considered in the study. A plot showing the typical variation of the lift coefficient C_L with time is given in Figure 5.10. The lift force on the blade increases as the blade penetrates into the vortex core, peaks when the blade leading edge is roughly two-thirds of the way through the cutting process, and then decreases with further time as the uncut portion of the vortex core is stretched over the blade leading edge. The three stages of vortex cutting identified by Saunders and Marshall (2015) are indicated using vertical lines in Figure 5.10.

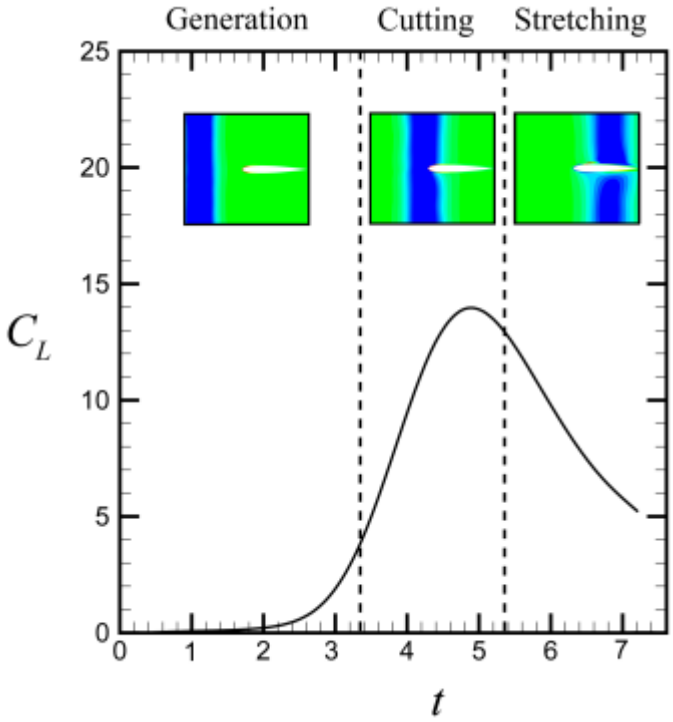

Figure 5.10: Time variation of the lift coefficient for Case 5. The three phases of vortex cutting are identified on the plot using vertical dashed lines.

The primary cause of the large transient lift force is the unequal pressure distribution on the top and bottom blade surfaces. A time series showing pressure contours in the *x*-*y* plane is given in Figure 5.11, where the leading and trailing edge of the vortex core are marked with dashed lines. Prior to penetration of the blade leading

edge into the vortex core (Figure 5.11a), the pressure distribution is approximately symmetric over the blade centerline surface $y = 0$.

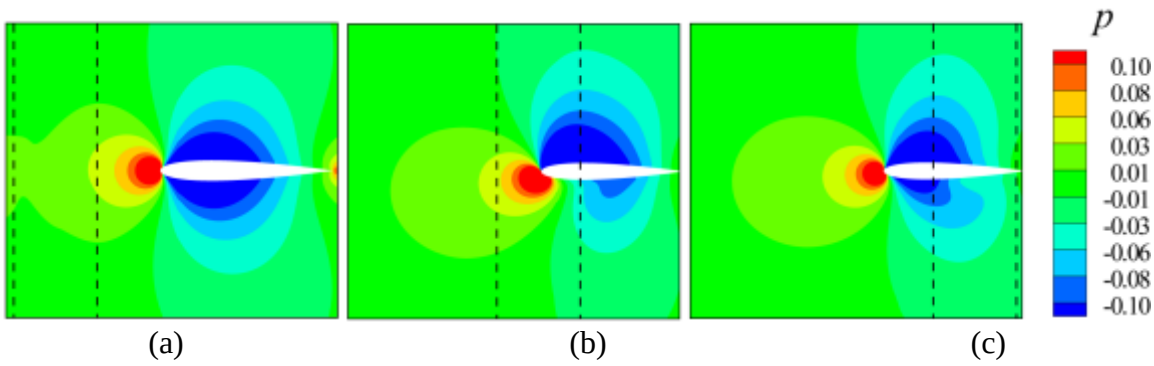

Figure 5.11: Time series of pressure contours in the *x*-*y* plane for Case 5 at (a) *t* = 1.8, (b) 4.2, and (c) 6.6. Edges of the vortex core are indicated with dashed lines.

As the blade penetrates into the vortex core (Figure 5.11b), the upward axial flow increases the pressure on the lower surface of the blade and decreases the pressure on the upper surface, leading to development of an asymmetric pressure profile. As cutting ends and the uncut core is stretched over the blade leading edge (Figure 5.11c), the pressure again approaches a nearly symmetric condition and the net force on the blade decreases.

The effect of the vortex axial flow on the shear and pressure distributions on the blade surface is shown in Figures 5.12-5.13. Figure 5.12a-b shows the change in shear stress on the blade surface between the time at which the peak cutting force occurs and that acting on a blade immersed in a uniform free stream flow with no vortex.

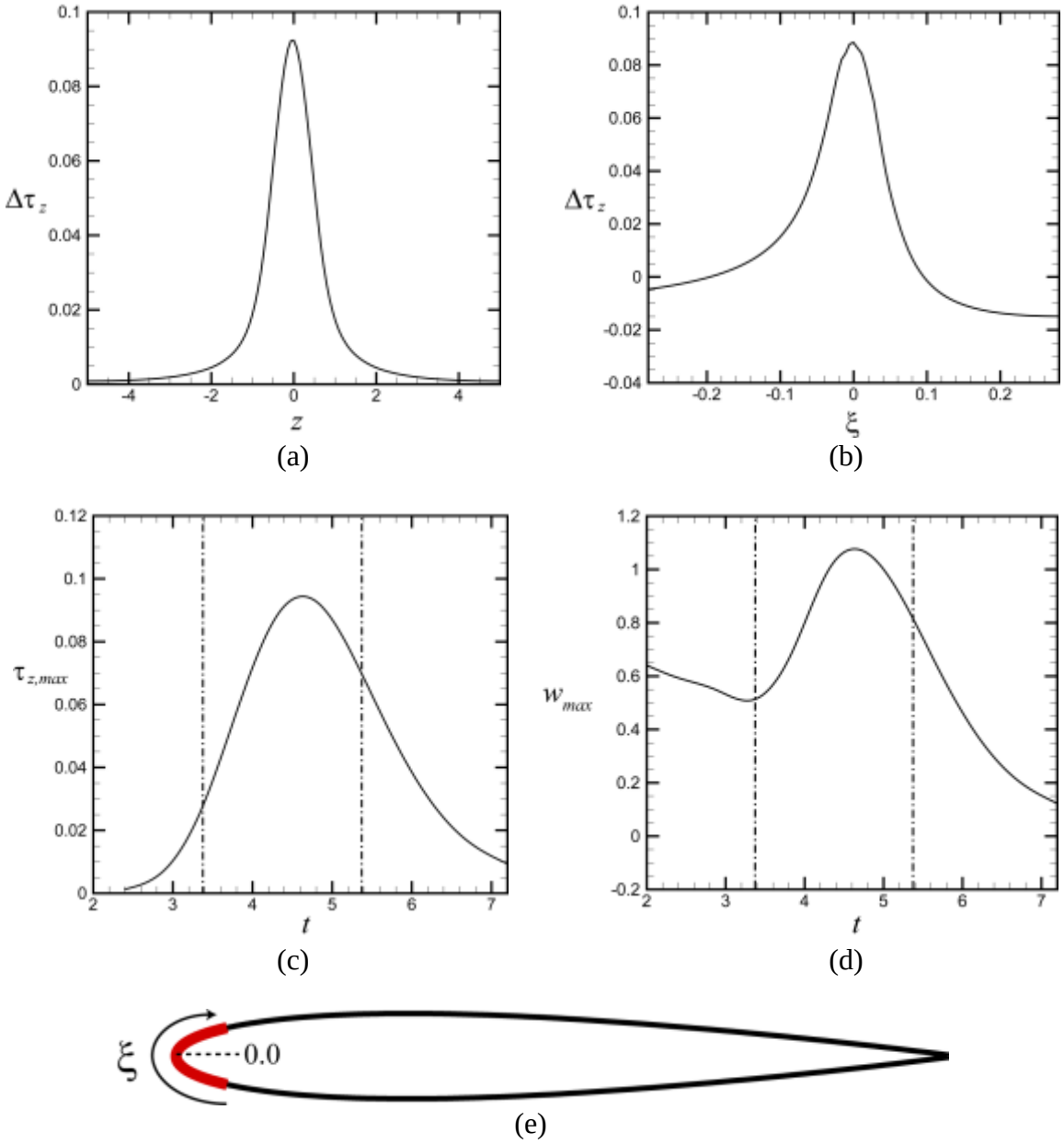

Figure 5.12: Difference in the spanwise shear stress $\Delta\tau_z$ between computations with and without the vortex present (a) along the blade leading edge as a function of spanwise length *z* and (b) along the blade surface as a function of arc length ξ in the $z = 0$ plane (see insert (e)) at time *t* = 4.8. Also shown are the maximum values of (c) spanwise shear stress τ_z along the blade leading edge and (d) axial velocity *w* within the vortex core on the plane $y = 0$ as functions of the dimensionless time. In (c) and (d), the nominal vortex cutting starting and ending times are indicated by vertical dashed-dotted lines. The simulations are for Case 5.

In Figure 5.12a, the change in shear stress is plotted as a function of the span-wise distance z along the blade leading edge ($x = y = 0$). The largest shear stress occurs in the center of the span, where the vortex core impacts the blade. Figure 5.12b shows the change in shear stress as a function of arc length ξ along a curve wrapped around the blade leading edge within the $z = 0$ plane. A sketching illustrating this curve is given in Figure 5.12e, where $\xi = 0$ corresponds to the blade leading edge. The largest change in shear stress occurs at the leading edge of the blade. The asymmetrical change in shear stress along the top and bottom surfaces of the blade front is due to the axial flow within the vortex core, where the axial flow combines with the free stream velocity to increase the shear stress on the blade upper surface and to decrease the shear stress on the blade lower surface. In Figure 5.12c, the maximum spanwise shear stress on the blade leading edge is plotted versus dimensionless time. The peak in spanwise shear stress occurs roughly two-thirds of the way through the vortex cutting process, corresponding to the peak in lift coefficient in Figure 5.10. In Figure 5.12d, the maximum axial velocity in the blade center plane $y = 0$ is plotted versus dimensionless time. Again, the peak occurs at roughly two-thirds of the way through the vortex cutting process. As the cutting process begins, the maximum value of axial velocity increases due to the deformation of the vortex core as it is cut by the blade. After cutting, the maximum value of axial velocity in the blade center plane decreases as the vortex compression and expansion waves propagate away from the blade, leaving regions of the vortex with low axial flow near the blade.

Figure 5.13 shows how the pressure distribution on the blade surface is changed by penetration of the blade into a vortex with axial flow.

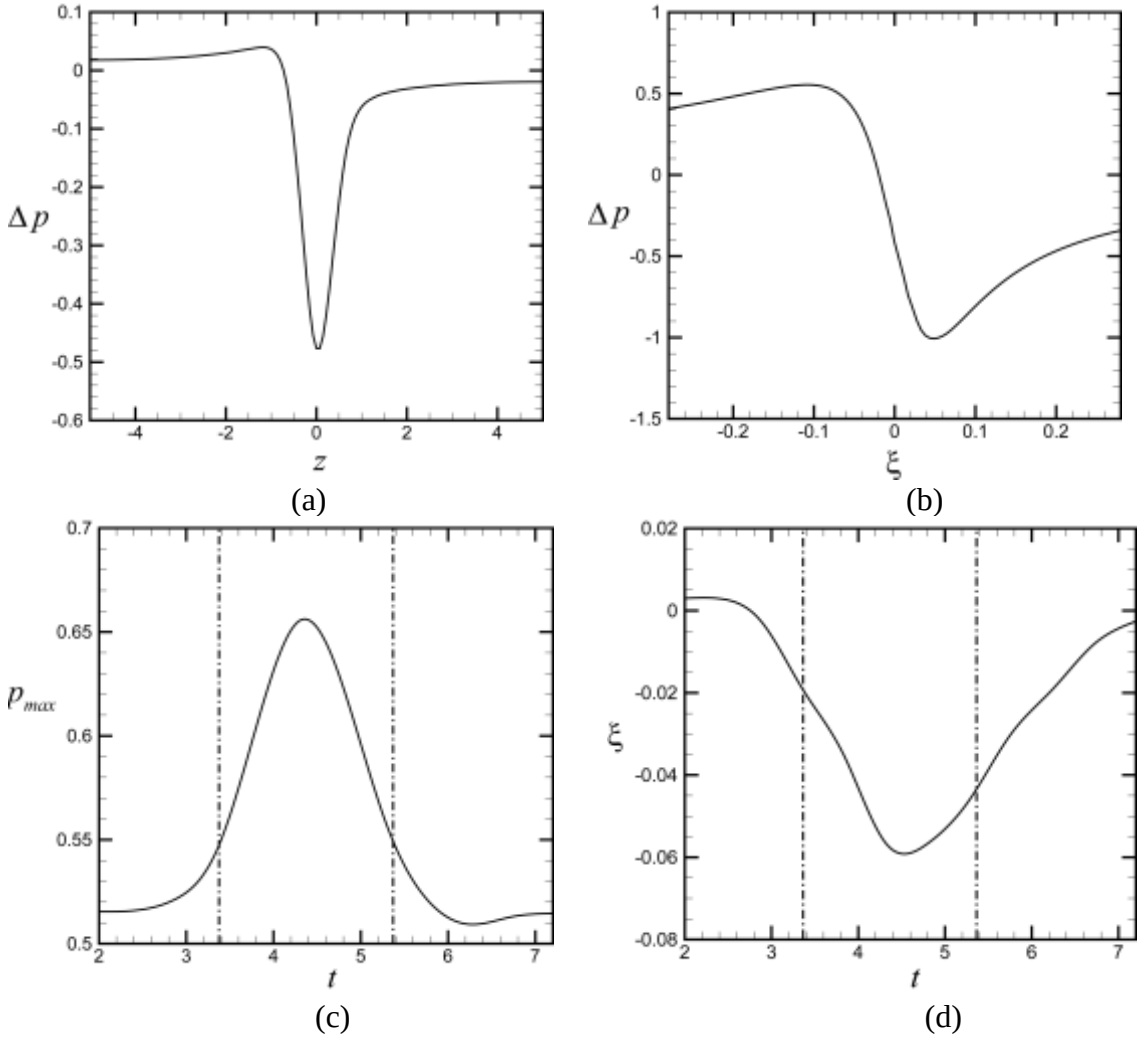

Figure 5.13: Difference in surface pressure Δp between computations with and without the vortex present (a) along the blade leading edge as a function of spanwise length *z* and (b) along the blade surface as a function of arc length ξ in the $z = 0$ plane at time *t* = 4.8. Also shown are the maximum values of (c) pressure within the plane $z = 0$ and (d) value of ξ corresponding to the maximum surface pressure position as functions of dimensionless time. In (c) and (d), the nominal vortex cutting starting and ending times are indicated by vertical dashed-dotted lines. The simulations are for Case 5.

Figure 5.13a-b shows the change in pressure on the blade surface between the time at which the peak cutting force occurs and that acting on a blade immersed in a uniform free stream flow with no vortex. The change in pressure is plotted versus the spanwise distance z in Figure 5.13a, showing a sharp decrease in pressure in the center region where the vortex impinges on the blade leading edge. The pressure change is asymmetric, however, with a slightly increased pressure on the left of the vortex ($z < 0$) and a slightly decreased pressure on the right of the vortex ($z > 0$). This asymmetry is a result of the direction of the vortex swirl relative to the ambient uniform flow. The pressure change is plotted in Figure 5.13b as a function of arc length ξ on the curve wrapping about the blade front shown in Figure 5.12e. The pressure increases on the bottom surface of the blade and decreases on the top surface, both of which occur due to interaction of the blade with the vortex axial flow. The maximum pressure on the blade over the $z = 0$ plane center span is plotted versus dimensionless time in Figure 5.13c, and the value of arc length ξ at the location of maximum pressure is plotted in Figure 5.13d. The pressure maximum occurs halfway through the cutting process, when the center of the vortex core is located at the blade leading edge. As seen in Figure 5.13d, the pressure maximum is initially located at the blade leading edge, but as the blade penetrates into the vortex core the location of maximum pressure shifts downward (such that $\xi < 0$). Halfway through the cutting process the location of the pressure maximum begins to return toward the blade leading edge (Figure 5.13d).

The maximum lift coefficient for the different cases examined in Table 5.1 was calculated and the results were compared with those predicted by the plug-flow model (Section 5.3) and the scaling analysis for the transient force (Section 5.1). In conducting

this comparison, we note that the vortex structure is different in the two problems. The models used for the plug-flow computations were based on an assumption of uniform vorticity across the core, or a Rankine vortex. On the other hand, the dissipative character of the full Navier-Stokes calculations makes a Gaussian vortex a much better choice for this study. Because of these differences in vortex structure, as well as because of the numerous approximations incorporated into the plug-flow model, we expect only qualitative agreement in the lift coefficient trends obtained by the two approaches.

The predictions for the maximum lift coefficient from the Navier-Stokes simulations listed in Table 5.1 are plotted as a function of the three dimensionless parameters *A*, *I* and *T* in Figure 5.14a-c. The data from Cases 1-6 are shown on a log-log plot in Figure 5.14a as a function of the axial flow parameter *A*, with *I* and *T* held constant. Over the interval in A evaluated ($0.06 \le A \le 11$), the maximum lift coefficient predictions all fall on a straight line with slope -1, indicating inverse dependence of $C_{L,\max}$ on *A* over this range of values. The leveling out of the lift force observed for the steady-state force in Figure 5.4a for $A > 1$ is not evident in Figure 5.14a, which suggests that the maximum lift for these simulations is dominated by the transient lift force.

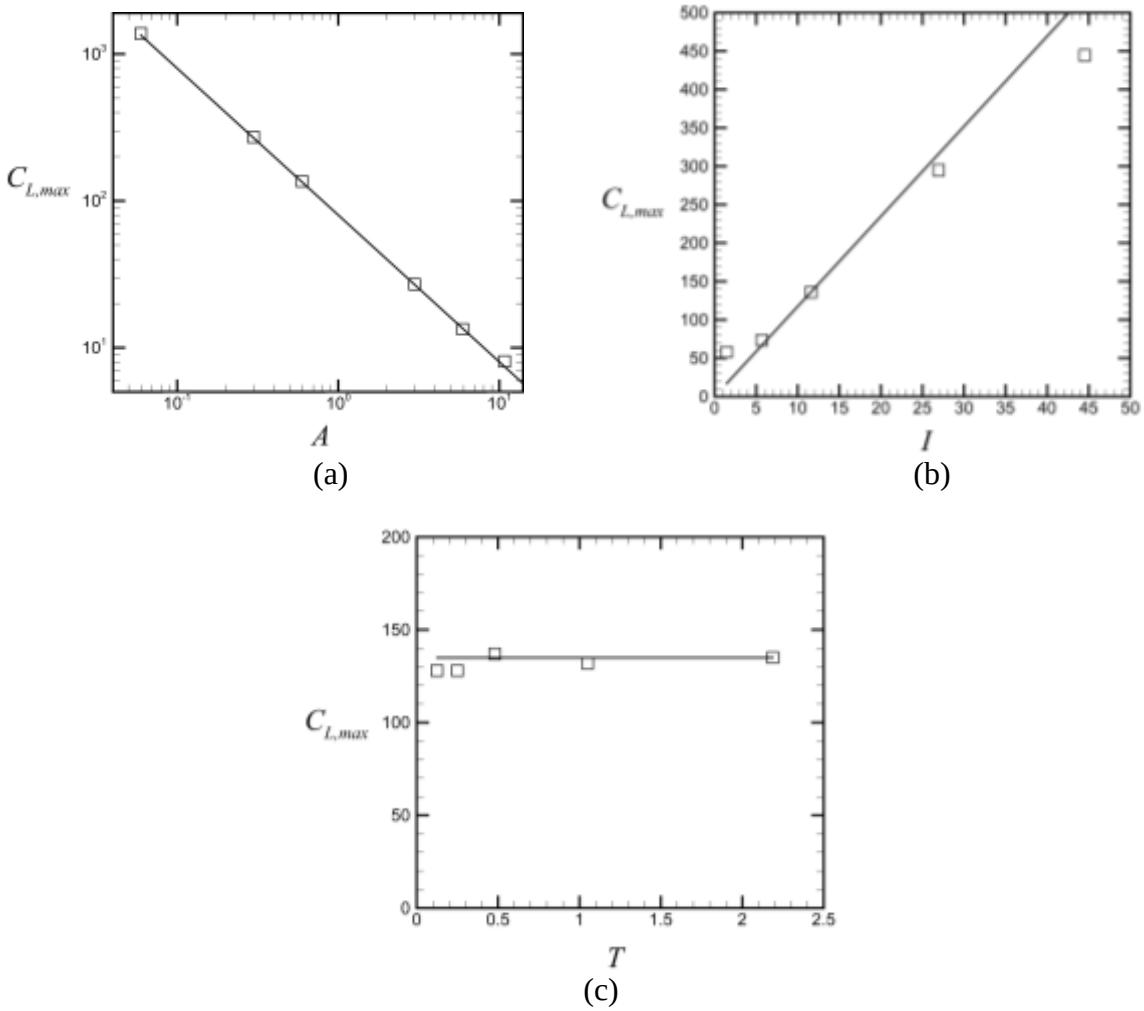

Figure 5.14: Variation of the maximum value of the lift coefficient with (a) axial flow parameter (I = 11.6, T = 0.48), (b) impact parameter (A = 0.6, T = 0.48), and (c) thickness parameter (A = 0.6, I = 11.6). Symbols are results of full Navier-Stokes computations and lines coincide with the prediction of the scaling result Eq. (5.27).

The influence of impact parameter on the lift coefficient was evaluated by plotting $C_{L,\max}$ as a function of I in Figure 5.14b for Cases 3 and 7-10, with A and T held fixed. The predicted lift coefficient values are observed to vary approximately linearly with a slope close to unity as I varies over the interval $1.4 \le I \le 45$, as indicated by the solid line in Figure 5.14b. The increase in $C_{L,\max}$ value above this line for the case with low impact parameter (I = 1.4) and the decrease in $C_{L,\max}$ value below this line for the

case with high impact parameter (I = 44.5) are consistent with similar trends for the plug-flow model evident in Figure 5.4b. The flattening out of the lift force prediction for $I = 1.4$ is similar to the effect of the steady-state lift force as observed in Figure 5.4b, whereas the transient lift force seems to dominate for the other cases plotted in Figure 5.14b. We also note that cases with small values of the impact parameter can exhibit shedding of vorticity from the blade boundary layer prior to impact of the vortex onto the blade surface (Krishnamoorthy and Marshall, 1998), which imposes a lower limit of approximately unity on the value of I, below which the vortex-blade interaction problem is fundamentally altered.

The influence of thickness parameter on the lift coefficient was examined by plotting $C_{L,\max}$ as a function of T in Figure 5.14c for Cases 3 and 11-13, with A and I held fixed. The maximum value of lift coefficient is found to be approximately independent of the thickness parameter in the range $T \le 2$ examined in the full Navier-Stokes simulations. By comparison, the plug-flow predictions in Figure 5.4c are also nearly constant as blade thickness is varied, although they exhibit a slight increase with thickness parameter T which is not evident in the full Navier-Stokes simulation results.

Most of the data trends observed for the full Navier-Stokes simulation results reported in this paper indicate that the transient lift force is the dominant force controlling the maximum value of lift. The scaling analysis for the transient lift force in Section 5.1 yields the estimate (5.5) for the maximum value of the lift coefficient. In keeping with the observation that the lift coefficient is nearly independent of the thickness parameter within the range of values examined in the full Navier-Stokes simulations, we find that a good fit to the computed lift coefficient data is obtained by setting $\pi(C_1 T + C_2)$ in (5.5)

equal to a constant value, which is obtained as approximately 7.0 by a fit to the data in Figure 5.14, thus giving an expression for the maximum lift coefficient over the range of parameters considered in the computations as

$$C_{L,tr,\max} \cong 7.0\, I / A \tag{5.27}$$

The prediction from (5.27) is indicated by the solid lines in Figures 5.14a-c. The good fit between the scaling estimate (5.27) and our data for maximum lift coefficient suggests that a collapse of the lift coefficient predictions for the full Navier-Stokes simulations can be obtained by plotting the ratio AC_L / I versus dimensionless time, which is shown in Figure 5.15. The symbols in this Figure include all runs except for Case 7, which has a very low impact parameter ($I = 1.4$) and for which case the maximum lift coefficient in Figure 5.14b is significantly above that given by (5.27). The data for $C_{L,max}$ originally spanned over more than two orders of magnitude, and while Figure 5.15 still shows a slight spread in the data, the deviation reduces from a root-mean-square (RMS) value of 347 for $C_{L,max}$ to a RMS value of 0.114 for the scaled variable $AC_{L,\max} / I$. This significant reduction in RMS value and the agreement in Figure 5.14 between the scaling analysis and results from the Navier-Stokes simulations indicates that the scaling estimate provides a reasonable estimate for the maximum lift coefficient.

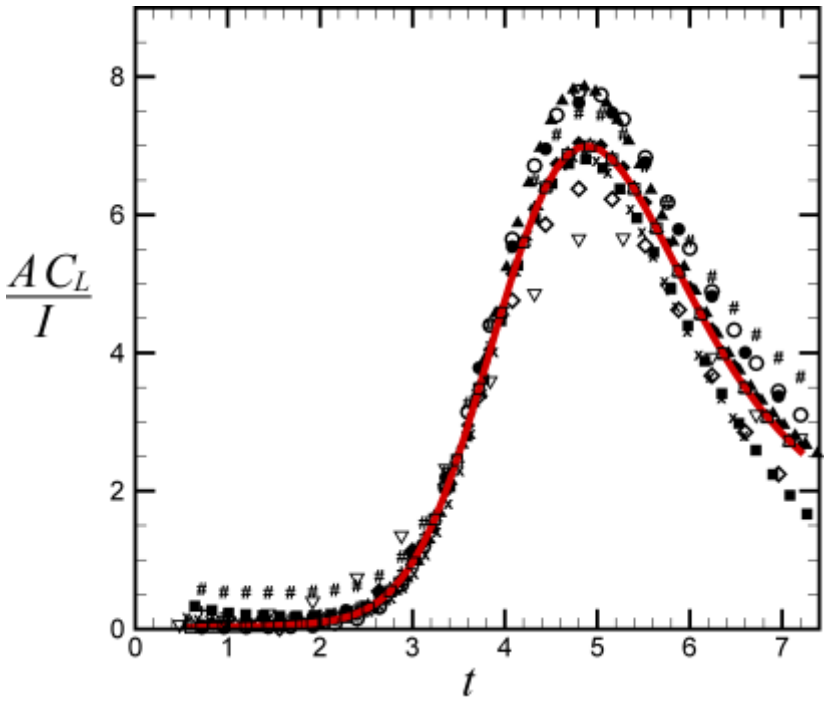

Figure 5.15: Plot showing collapse of the lift coefficient as a function of dimensionless time, with symbols indicating data from the various cases indicated in Table 5.1. The red curve has a maximum value of 7.0, which coincides with the scaling estimate Eq. (5.27).

5.6. Conclusions

The current chapter investigated the physics of this transient force and its relationship with the previously proposed steady-state force. This investigation was conducted using a scaling analysis of the transient penetration force, a review of the previously proposed steady-state force, a heuristic model for the vortex response to cutting based on the plug-flow approximation for the axial flow in the vortex core (similar to Saffman's 1990 model for vortex reconnection), and full Navier-Stokes simulations of the vortex-blade interaction, each of which lead to interesting insights. The scaling analysis of the transient vortex cutting force in Section 5.1 explained the empirical observation of Liu and Marshall (2004) for why the blade lift varies as the

product of w_0 and *U*, and is independent of Γ. When nondimensionalized in terms of a lift coefficient C_L, the scaling analysis indicates that the maximum value of C_L for the transient force will vary proportionally to the ratio I/A. In contrast, the steady-state vortex cutting force is just a function of the axial flow parameter *A*. Furthermore, the implicit expression for the steady-state force was shown to admit two asymptotic solutions (for high and low values of axial flow parameter *A*), which when patched together give a good explicit expression for the force over the entire range of *A*. The effect of blade penetration on the vortex in the plug-flow model (Lungren and Ashurst, 1989) was introduced by addition of a viscous shear force on the blade, which triggered the expected response of the core radius and vortex axial flow to cutting. While the plug-flow model is very simple, it was shown to yield solutions for the blade lift coefficient that match the predictions of the transient scaling theory and the steady-state force theory in different regimes.

The full Navier-Stokes simulations in Section 5.4 were used to investigate the variation of both the blade surface pressure and the shear stress during vortex cutting, focusing on how the presence of a non-zero vortex axial flow effects the cutting process. The lift coefficient predictions obtained from the full simulations were found to agree with the scaling suggested by the transient force scaling analysis, resulting in a data collapse which yields an approximate expression for the maximum value of the blade lift coefficient during penetration into a vortex core within a region of parameter space indicated by $0.06 < A < 11$, $2 \le I \le 45$ and $0 < T < 2$. The vortex-cutting process is not limited to this range of parameters and the data collapse may hold for other parameters outside this range. However, one should be aware that in certain limits of parameter space

the physical processes involved in the vortex-blade interaction change, which will likely restrict the range of applicability of this expression. An example of this is for low values of impact parameter ($I < 2$). For these values, the flow is modified by shedding of vorticity from the blade leading edge prior to vortex impact and the shed vorticity wraps around the vortex core which modifies the vortex prior to impact onto the blade. Also, for high values of thickness parameter ($T > 2$), the vortex can exhibit significant bending due to the inviscid interaction with the blade prior to impact. Vortex bending delays the impact time, stretches the vortex, and can enhance generation and shedding of boundary layer vorticity from the blade surface. For cases with sufficiently high values of the axial flow parameter, the vortex can become unstable due to the axial flow (Khorrami, 1991; Lessen et al., 1974; Mayer and Powell, 1992), causing both generation of bending waves and small-scale motion surrounding the vortex core.

CHAPTER 6: FINAL CONCLUSIONS AND RECOMMENDATIONS

In this dissertation both advantages and disadvantages of wake interactions were examined. One advantageous effect of wake interactions, the minimization of the variability in farm power output, was investigated with the use of a farm-level controller. Specifically, a nonlinear MPC scheme was introduced to examine the importance of wake interactions on the controller for both power maximization and variability minimization. In practice, a farm-level MPC approach for wind farm control would also have to take into account additional aspects such as wind forecast error, varying wind directions, wake meandering, and constraints on computational time. However, exploring the behavior and limits of an 'ideal' farm-level controller does have broader applications which can be applied to wind farm control. It was found that whether by the use of smoothing individual power curves, or using the constructive and destructive interference between the individual power curves, a controller can significantly reduce farm power variability without significantly reducing electrical energy output when accounting for variability within the objective function of the controller. Furthermore, the findings that the controller performance improves as the time horizon increases, and that this occurs as discrete transitions rather than a continuous improvement, can be applied to the design of farm-level controllers.

In the future, wind farm control studies will need to further address both extending the results past the simple, 3-turbine system considered in Chapter 3 and the limitations of current engineering wake models. Simulations incorporating two-dimensional grids of wind turbines and allowing for both time and space varying velocity

inputs will improve the results from optimization-based control schemes. In addition, the applicability of the reported results will broaden as the accuracy of wake models improves. This is an active field of research with researchers working to improve such aspects as time delay modeling, transfer functions for how the input velocity changes across a turbine, and the velocity deficit in turbulent wakes (Knudsen et al., 2012; Gebraad et al., 2015; Gebraad et al., 2014) A recent study using a higher-order wake model has even called into question previous findings that axial induction-based methods of cooperative control provide a net increase in the net wind farm power over individual turbine control methods (Annoni et al., 2016). The improvement of engineering wake models, particularly for dynamic wake conditions, while maintaining sufficient simplicity that these models can be incorporated into optimization-based control schemes, will continue to be an important area for wind turbine wake studies.

The second and third studies described in this dissertation focused on investigating the interaction between turbine blades and coherent vortex structures found within the wakes of upstream turbines. Specifically, the basic phenomenon of vortex cutting by a blade and the vortex cutting force that results when a vortex with non-zero axial flow is cut by a blade were investigated. While an understanding of the various physical processes involved in blade penetration into a vortex core has slowly developed over the past two decades, prediction of the vortex-blade interaction force has remained a challenge. This is true even if only considering a particular type of vortex-blade interaction, such as orthogonal interaction in the presence of an ambient vortex axial flow, which is a primary cause of large unsteady structural loading in these flow fields. It was noted by Marshall (1994) that the cutting of a vortex with axial flow results in a

difference in core radius over the vortex core, which results in a difference in the net pressure force over the blade surface. A simple analytical model for the vortex response to "instantaneous" cutting was proposed by Marshall (1994) that in later work was shown to compare well to numerical predictions and experiments. This vortex response model also yields a prediction for the vortex cutting force caused by the core radius difference across the blade following completion of the vortex cutting, which in this dissertation is referred to as the steady-state vortex cutting force. In a later paper, Liu and Marshall (2004) found that the lift force on the blade appeared not to be dominated by this steady-state force, but instead was controlled by a transient force that peaks during the initial penetration of the blade leading edge into the vortex core and then decreases as the vortex is further cut. They validated the computed cutting force with experimental data and observed empirically that it seemed to be proportional to the product of the vortex axial velocity w_0 and the freestream velocity U, and was independent of the vortex circulation.

The current study clarifies the underlying physics of the transient vortex cutting force using a combination of scaling theory, an approximate plug-flow model of the vortex core flow, and full Navier-Stokes simulations. All of these approaches lead to development of a validated data collapse for the lift force on a blade during vortex cutting, along with a simple expression for the maximum lift force. This data collapse can help aid in the creation of more accurate models for unsteady wind turbine blade loadings based on information about the wake vortex structures and future work should examine if this data collapse still holds for cases involving blades with non-zero angles of attack. In addition, knowledge regarding the relevant parameters and timescales of the cutting process can help validate and guide CFD simulation designs of wind farm wake

interactions. The results from these studies are also applicable to a wide range of other problems in which vortices interact with lifting surfaces. In applications ranging from hydraulic pumps, to helicopter aerodynamics, to submarine dynamics the vortex cutting process can lead to undesirable structural vibrations or acoustic emissions which will be best minimized through continued advancement in understanding and modeling the vortex-cutting process.

There are broader implications of this work beyond the need for improved wake and turbine fatigue models. Currently, commercial wind turbines are individually equipped with traditional PID controllers to maximize the power output of each turbine. This type of setup does not allow for coordinated control of multiple turbines and any restrictions on total farm power output will be decided for each turbine separately. This work has demonstrated how farm-level control systems can be used to improve the quality of farm power supplied to the electric grid and the contribution of wake vortices to unsteady loadings on turbine blades. These findings suggest that wind farm capabilities could be greatly improved with the incorporation of farm-level control systems into utility-scale wind farms. Farm-level control systems can allow wind farms to participate in new markets such as the ancillary services market, or to generate power in areas where the electric grid is more susceptible to instabilities caused by large variations in power generation. Furthermore, the damage to individual turbines could be more accurately quantified and reduced, decreasing the likelihood of unscheduled maintenance and repairs to turbines. While the timescale of wind speed fluctuations considered in this study allowed for the demonstration of power smoothing through coordinated control of wind turbines, fluctuations in wind speed on the order of hours to days also need to be

considered. The power variability caused by these longer timescales cannot be reduced via cooperative control of turbines but would need to be addressed with the incorporation of energy storage devices or demand response programs.

BIBLIOGRAPHY

Ahmadi, A.R. 1986 An experimental investigation of blade-vortex interaction at normal incidence. *AIAA Journal of Aircraft* **23**(1), 47-55.

Annoni J., Gebraad P.M.O., Scholbrock, A.K., Fleming, P.A., Van Wingerden, JW. 2016 Analysis of axial-induction-based wind plant control using an engineering and a high-order wind plant model. *Wind Energy* **19**, 1135-1150. DOI: 10.1002/we.1891

Barthelmie R.J., Folkerts L., Larsen G.C., Rados K., Pryor S.C., Frandsen S.C., Lange B., Schepers G. 2005 Comparison of wake model simulations with offshore wind turbine wake profiles measured by sonar. *J Atmospheric Ocean Technol* **23**, 881-901. DOI: 10.1175/JTECH1886.1

Binder, A. 1985 Turbulence production due to secondary vortex cutting in a turbine rotor. *Journal of Engineering for Gas Turbines and Power* **107**, 1039-1046.

Bjerge C., Kristoffersen J.R. 2007 How to run an offshore wind farm like a conventional power plant. *Modern Power Systems* **27**, 31-33.

Boratav, O.N., Pelz, R.B. & Zabusky, N.J. 1992 Reconnection in orthogonally interacting vortex tubes: Direct numerical simulations and quantifications. *Physics of Fluids A* **4**(3), 581-605.

Bossanyi E. 2003 Wind turbine control for load reduction. *Wind Energy* **6**(3), 229-244. DOI: 10.1002/we.95

Bottasso C.L., Croce A., Savini B. 2007 Performance comparison of control schemes for variable-speed wind turbines. *Journal of Physics: Conference Series* **75,** 012079. DOI: 10.1088/1742-6596/75/1/012079

Boukhezzar B., Lupu L., Siguerdidjane H., Hand M. 2007 Multivariable control strategy for variable speed, variable pitch wind turbines. *Renew Energy* **32**(8), 1273 - 1287. DOI: 10.1016/j.renene.2006.06.010

Burgers, J.M. 1948 A mathematical model illustrating the theory of turbulence. *Adv. Appl. Mech.* **1**, 171–199.

Burkart R., Margellos K., Lygeros J. 2011 Nonlinear control of wind turbines: an approach based on switched linear systems and feedback linearization. *Decision and control and European control conference (CDC-ECC),* 2011 50th IEEE conference on IEEE, 5485 – 5490. DOI: 10.1109/CDC.2011.6160709

Burton T., Sharpe D., Jenkins N., Bosanyi E. 2008 *Wind Energy Handbook (2nd edn)*. John Wiley and Sons: Chichester, West Sussex, UK.

Cary, C.M. 1987 An experimental investigation of the chopping of helicopter main rotor tip vortices by the tail rotor. NASA CR-177457.

Churchfield, M.J., Lee, S., Michalakes, J. & Moriarty, P.J. 2012 A numerical study of the effects of atmospheric and wake turbulence on wind turbine dynamics. *Journal of Turbulence* **13**, January.

Clemow P., Green T.C., Hernandez-Aramburo C.A. 2010 Wind farm output smoothing through co-ordinated control and short-term wind speed prediction. *IEEE PES General Meeting*, 1-8. DOI: 10.1109/PES.2010.5590112

Coton, F.N., Marshall, J.S., McD. Galbraith, R.A. & Green, R.B. 2004 Helicopter tail rotor orthogonal blade-vortex interaction. *Progress in Aerospace Sciences* **40**(7), 453-486.

De Rijcke S., Driesen J., Meyers J. 2015 Power smoothing in large wind farms using optimal control of rotating kinetic energy reserves. *Wind Energy* **18**(10), 1777-1791. DOI: 10.1002/we.1790

Doolan, C., Coton, F. & Galbraith, R. 1999 Three-dimensional vortex interactions with a stationary blade. *Aeronautical Journal* **103**(1030), 578-587.

Doolan, C.J., Coton, F.N. & Galbraith, R.A. 2001 Surface pressure measurements of the orthogonal vortex interaction. *AIAA Journal* **38**(1), 88-95.

Earle, M.D. 1996 Nondirectional and Directional Wave Data Analysis Procedures. *NDBC Technical Document 96001*.

Early, J., Green, R. & Coton, F. 2002 Flow visualization of the orthogonal blade-vortex interaction using particle image velocimetry. *Aeronautical Journal* **106**(1057), 137-145.

Ebrahimi, F.M., Khayatiyan, A., Farjah, E. 2016 A novel optimizing power control strategy for centralized wind farm control system. *Renewable Energy* **86**, 399-408. DOI: 10.1016/j.renene.2015.07.101

Felli, M. & Falchi, M. 2011 Propeller tip and hub vortex dynamics in the interaction with a rudder. *Experiments in Fluids* **51**, 1385-1402.

Felli, M., Camussi, R. & Guj, G. 2009 Experimental analysis of the flow field around a propeller-rudder configuration. *Experiments in Fluids* **46**, 147-164.

Filippone, A. & Afgan, I. 2008 Orthogonal blade-vortex interaction on a helicopter tail rotor. *AIAA Journal* **46**(6), 1476-1489.

Gebraad P.M.O., Van Wingerden, J.W. 2015 Maximum power-point tracking control for wind farms. *Wind Energy* **18**, 429-447. DOI: 10.1002/we.1706

Gebraad, P.M.O., Fleming, P.A. 2014 A control-oriented dynamic model for wakes in wind plants. *Journal of Physics: Conference Series*, IOP Publishing **524**(1). DOI: 10.1088/1742-6596/524/1/012186

Gebraad, P.M.O., Fleming, P.A., Van Wingerden, J.W. 2015 Wind turbine wake estimation and control using FLORIDyn, a control-oriented dynamic wind plant model. *American Control Conference*, 1702-1708. DOI: 10.1109/ACC.2015.7170978

Gibbon, J.D., Fokas, A.S. & Doering, C.R. 1999 Dynamically stretched vortices as solutions of the 3D Navier–Stokes equations. *Physica D* **132**, 497–510.

Gonzalez-Longatt, F., Wall, P., Terzija, V. 2012 Wake effect in wind farm performance: Steady-state and dynamic behavior. *Renewable Energy* **39**, 329-338. DOI: 10.1016/j.renene.2011.08.053

Green, R., Doolan, C. & Cannon, R. 2000 Measurements of the orthogonal blade-vortex interaction using a particle image velocimetry technique. *Experiments in Fluids* **29**, 369-379.

Green, R.B., Coton, F.N. & Early, J.M. 2006 On the three-dimensional nature of the orthogonal blade-vortex interaction. *Experiments in Fluids* **41**, 749-761.

Guo Y., Hosseini S.H., Tang C.Y., Jiang J.N., Ramakumar R.G. 2013 An approximate wind turbine control system model for wind farm power control. *IEEE Transactions on Sustainable Energy* **4**, 262-274. DOI: 10.1109/TSTE.2012.2217992

Hansen, A., Sorensen, P., Iov, F., Blaabjerg, F. Centralized power control of wind farm with doubly fed induction generators. *Renewable Energy* **31**(7), 935-951. DOI: 10.1016/j.renene.2005.05.011

Hiemenz, K. 1911 Die Grenzschicht an einem in den gleichförmigen Flüssigkeitsstrom eingetauchten geraden Kreiszylinder. *Dingler's Polytech. J.* **326**, 321.

Holkar, K.S., Waghmare, L. M. 2010 An Overview of Model Predictive Control. International Journal of Control and Automation **3**(4), 47-63.

Howe, M.S. 1989 On unsteady surface forces, and sound produced by the normal chopping of a rectilinear vortex. *Journal of Fluid Mechanics* **206**, 131–153.

Issa, R. 1985 Solution of the implicit discretized fluid flow equations by operator splitting. *Journal of Computational Physics* **62**, 40-65.

Jensen, N.O. 1983 A note on wind generator interaction. *Riso National Laboratory,* Report M-2411.

Johnson K.E., Fritsch G. 2012 Assessment of extremum seeking control for wind farm energy production. *Wind Engineering* **36**, 701 - 716. DOI: 10.1260/0309-524X.36.6.701

Johnson K.E., Thomas N. 2009 Wind farm control: addressing the aerodynamic interaction among wind turbines. *Proceedings of the European Wind Energy Conference,* Marseille, France. DOI: 10.1109/ACC.2009.5160152

Johnston, R.T. & Sullivan, J.P. 1992 Unsteady wing surface pressures in the wake of a propeller. AIAA Paper 92-0277.

Jonkman, J.M., Butterfield, S., Musial, W., Scott, G. 2009 Definition of a 5-MW reference wind turbine for offshore system development. *National Renewable Energy Laboratory,* Golden, CO.

Khorrami, M.R. 1991 On the viscous modes of instability of a trailing line vortex. *Journal of Fluid Mechanics* **225**, 197-212.

Kida, S. & Takaoka, M. 1994 Vortex reconnection. *Annual Review of Fluid Mechanics* **26**, 169-189.

Kida, S., Takaoka, M. & Hussain, F. 1991 Formation of head-tail structure in a two-dimensional uniform straining flow. *Physics of Fluids A* **3**(11), 2688-2697.

Knudsen, T., Bak, T. 2012 Data driven modeling of the dynamic wake between two wind turbines. *IFAC Symposium on System Identification,* 1677-1682. DOI: 10.3182/20120711-3-BE-2027.00128

Knudsen, T., Bak, T., Svenstrup, M. 2015 Survey of wind farm control-power and fatigue optimization. *Wind Energy* **18**, 1333-1351. DOI: 10.1002/we.1760

Koerber, A., King, R. 2013 Combined feedback-feedforward control of wind turbines using state-constrained model predictive control. *IEEE Transactions on Control Systems Technology* **21**(4), 1117-1128.DOI: 10.1109/TCST.2013.2260749

Korber, A., King, A. 2009 Model predictive control for wind turbines. *Proc. 47th AIAA Aerospace Sciences Meeting*, Orlando, Florida.

Korber, A., King, R. 2011 Nonlinear model predictive control for wind turbines. *Proc. EWEC*.

Krishnamoorthy, S. & Marshall, J.S. 1994 An experimental investigation of 'vortex shocks'. *Physics of Fluids* **6**(11), 3737-3741.

Krishnamoorthy, S. & Marshall, J.S. 1998 Three-dimensional blade-vortex interaction in the strong-vortex regime. *Physics of Fluids* **10**(11), 2828-2845.

Kristalny, M., Madjidian, D., Knudsen, T. 2013 On using wind speed preview to reduce wind turbine tower oscillations. *Control Syst Technol IEEE Trans* **21**(4), 1191- 1198. DOI: 10.1109/TCST.2013.2261070

Kumar, A., Stol, K. 2009 Scheduled model predictive control of a wind turbine. *47th AIAA Aerospace Sciences Meeting*, Orlando, Florida. DOI: 10.2514/6.2009-481

Lai, Y.G. 2000 Unstructured grid arbitrarily shaped element method for fluid flow simulation. *AIAA Journal* **38**(12), 2246-2252.

Laks, J., Pao, L.Y., Simley, E., Wright, A., Kelley, N., Jonkman, B. 2011 Model predictive control using preview measurements from LIDAR. *Proc. 49th AIAA aerospace sciences meeting*, Orlando, FL. DOI: 10.2514/6.2011-813

Lee, J., Burggraf, O. & Conlisk, A. 1998 On the impulsive blocking of a vortex jet. *Journal of Fluid Mechanics* **369**, 301-331.

Leishman, J. G., *Principles of Helicopter Aerodynamics*, Cambridge University Press, Cambridge, U.K., p. 351 (2006).

Lessen, M., Singh, P.J. & Paillet, F. 1974 The instability of a trailing line vortex. Part 1. Inviscid theory. *Journal of Fluid Mechanics* **63**, 753-763.

Leverton, J.W., Pollard, J. S. & Wills, C. R. 1977 Main rotor wake/tail rotor interaction. *Vertica* **1**, 213-221.

Lindeberg, E. 2009 Optimal control of floating offshore wind turbines, *Master's Thesis*, Norwegian University of Science and Technology.

Liu, X. & Marshall, J.S. 2004 Blade penetration into a vortex core with and without axial core flow. *Journal of Fluid Mechanics* **519**, 81-103.

Lundgren, T.S., & Ashurst, W.T. 1989 Area-varying waves on curved vortex tubes with application to vortex breakdown. *Journal of Fluid Mechanics* **200**, 283–307.

Madjidian, D., Martensson, K., Rantzer, A. 2011 A distributed power coordination scheme for fatigue load reduction in wind farms. *American Control Conference*.

Malik, N.A., Vassilicos, J.C. 1996 Eulerian and Lagrangian scaling properties of randomly advected vortex tubes. *J. Fluid Mech* **326**, 417-436.

Marden, J.R., Ruben, S.D., Pao, L.Y. 2013 A model-free approach to wind farm control using game theoretic methods. *IEEE Trans. Control Systems Technology* **21**(4), 1207-1214. DOI: 10.1109/TCST.2013.2257780

Marshall, J.S. & Yalamanchili, R. 1994 Vortex cutting by a blade. Part II. Computations of vortex response. *AIAA Journal* **32**(7), 1428-1436.

Marshall, J.S. & Grant, J.R., 1996 Penetration of a blade into a vortex core: vorticity response and unsteady blade forces. *Journal of Fluid Mechanics* **306**, 83-109.

Marshall, J.S. & Krishnamoorthy, S. 1997 On the instantaneous cutting of a columnar vortex with non-zero axial flow. *Journal of Fluid Mechanics* 351, 41-74.

Marshall, J.S. 1991 A general theory of curved vortices with circular cross-section and variable core area. *Journal of Fluid Mechanics* **229**, 311-338.

Marshall, J.S. 1994 Vortex cutting by a blade. Part I. General theory and a simple solution. *AIAA Journal* **32**(6), 1145-1150.

Marshall, J.S., *Inviscid Incompressible Flow*, John Wiley & Sons, New York (2001).

Mauledoux, M., Shkodyrev, V. 2009 Distributed multi-objective optimal control for wind farms. *PHYSCON*, Catania, Italy.

Mayer, E.W. & Powell, K.G. 1992 Viscous and inviscid instabilities of a trailing vortex. *Journal of Fluid Mechanics* **245**, 91-114.

Melander, M.V. & Hussain, F. 1989 Cross-linking of two antiparallel vortex tubes. *Physics of Fluids A* **1**(4), 633-635.

Nagahara, T., Sato, T. & Okamura, T. 2001 Effect of the submerged vortex cavitation occurred in pump suction intake on hydraulic forces of mixed flow pump impeller. CAV 2001: 4th International Symposium on Cavitation, Pasadena, California.

Nakamura, M., Nanayakkara, N., Yoshida, H., Hatazaki, H. 1995 Modelling and Prediction of Effective Wind Speed for Wind Turbine Operations. *International Conference on Automation*.

Ozdemir, A.A., Seiler, P., Balas, G.J. 2013 Design tradeoffs of wind turbine preview control. *Control Syst Technol IEEE Trans* **21**(4), 1079 - 1089. DOI: 10.1109/TCST.2013.2261069

Paterson, R.W. & Amiet, R.K. 1979 Noise of a model helicopter rotor due to ingestion of turbulence. NASA Tech. Rept. NASA CR-2313.

Rocha, R., Martins-Filho, L., Bortolus, M. 2005 Optimal multivariable control for wind energy conversion system: a comparison between H2 and H controllers. *Proceedings of the 44th IEEE conference on decision and control, and the European control conference*, 7906 - 7911.

Rodriguez-Amenedo, J., Arnaltes, S., Rodriguez, M. 2008 Operation and coordinated control of fixed and variable speed wind farms. *Renewable Energy* **33**(3), 406-414. DOI: 10.1016/j.renene.2007.03.003

Saffman, P.G. 1990 A model of vortex reconnection. *Journal of Fluid Mechanics* **212**, 395-402.

Saunders, D.C. & Marshall, J.S. 2015 Vorticity reconnection during vortex cutting by a blade. *Journal of Fluid Mechanics* **782**, 37-62.

Schlipf, D., Schlipf, D.J., Kuhn, M. 2013 Nonlinear model predictive control of wind turbines using LIDAR. *Wind Energy* **16**, 1107 - 1129. DOI: 10.1002/we.1533

Shafii, S., Obermaier, H., Linn, R., Koo, E., Hlawitschka, M., Garth, C., Hamann, B., & Joy, K.I. 2013 Visualization and analysis of vortex-turbine intersections in wind farms. *IEEE Transactions on Visualization and Computer Graphics* **19**(9)**,** 1579-1591.

Shelley, M.J., Meiron, D.I. & Orszag, S.A. 1993 Dynamical aspects of vortex reconnection of perturbed anti-parallel vortex tubes. *Journal of Fluid Mechanics* 246, 613-652.

Sheridan, P.F. & Smith, R.P. 1980 Interactional aerodynamics – a new challenge to helicopter technology. *Journal of the American Helicopter Society* **25**(1), 3-21.

Siggia, E.D. 1985 Collapse and amplification of a vortex filament. *Physics of Fluids* **28**, 794-805.

Soleimanzadeh, M., Wisniewski, R., Johnson, K. 2013 A distributed optimization framework for wind farms. *Journal of Wind Engineering and Industrial Aerodynamics* **123**, 88-98. DOI: 10.1016/j.jweia.2013.08.011

Soltani, M., Wisniewski, R., Brath, P., Boyd, S. 2011 Load reduction of wind turbines using receding horizon control. *IEEE international conference on Control applications (CCA)*, 852 - 857. DOI: 10.1109/CCA.2011.6044407

Sorensen, P., Hansen, A.D., Rosas, P.A.C. 2002 Wind models for simulations of power fluctuations from wind farms. *J Wind Eng Ind Aerodyn* **90**(12), 1381 - 1402. DOI: 10.1016/S0167-6105(02)00260-X

Spencer, M.D., Stol, K.A., Unsowrth, C.P., Cater, J.E., Norris, S.E. 2013 Model predictive control of a wind turbine using short-term wind field predictions. *Wind Energy* **16**, 417 - 434. DOI: 10.1002/we.1501

Spruce, C.J. 1993 Simulation and control of windfarms. *Ph.D. Thesis*, University of Oxford Department of Engineering Science Lady Margaret Hall.

Spudic, V., Baotic, M., Jelavic, M., Peric, N. 2010 Hierarchical wind farm control for power /load optimization. *Torque 2010 The Science of Making Torque from Wind*, EWEA, Heraklion, Crete, Greece.

Spudic, V., Baotic, M., Peric, N. 2011 Wind farm load reduction via parametric programming based controller design. *International Federation of Automatic Control (IFAC)*, Milano, Italy, 1704-1709. DOI: 10.3182/20110828-6-IT-1002.02956

Spudic, V., Conte, C., Baotic, M., Morari, M. 2015 Cooperative distributed model predictive control for wind farms. *Optim. Control Appl. Meth.* **36**, 333 - 352. DOI: 10.1002/oca.2136

Steinbuch, M., de Boer, W., Bosgra, O., Peters, S., Ploeg, J. 1988 Optimal Control of Wind Power Plants. *Journal of Wind Engineering and Industrial Aerodynamics* **27**(1-3), 237-246.

Wang, T., Doolan, C.J., Coton, F.N. & Galbraith, R.A.M. 2002 Experimental study of the three-dimensionality of orthogonal blade-vortex interaction. *AIAA Journal* **40**(10), 2037-2046.

Weigand, A. 1993 The response of a vortex ring to a transient spatial cut, Ph.D. Thesis, University of California, San Diego.

Yildirim, E. & Hillier, R. 2013 Numerical modeling of the impulsive orthogonal cutting of a trailing vortex. *Shock Waves* **23**, 369-379.

Zabusky, N.J. & Melander, M.V. 1989 Three-dimensional vortex tube reconnection: morphology for orthogonally-offset tubes. *Physica D* **37**, 555-562.